Coherent and Dissipative Transport in Metallic Atomic-Size Contacts

A Thesis
Presented to
The Academic Faculty

by

Zhenting Dai

In Partial Fulfillment
of the Requirements for the Degree
Doctor of Philosophy

School of Physics
Georgia Institute of Technology
December 2006

Coherent and Dissipative Transport in Metallic Atomic-Size Contacts

Approved by:

Professor Alexei Marchenkov, Advisor
School of Physics
Georgia Institute of Technology

Professor Philip First,
School of Physics
Georgia Institute of Technology

Professor Walter A. De Heer,
School of Physics
Georgia Institute of Technology

Professor James L. Gole
School of Physics
Georgia Institute of Technology

Professor Andrei Fedorov
School of Mechanical Engineering
Georgia Institute of Technology

Date Approved: 11/14/2006

To my parents.

ACKNOWLEDGEMENTS

First and foremost, I would like to thank my advisor, Prof. Alexei Marchenkov. He gave a lot of support not only in the academic research, but also in other parts of my life. Without his help, I would not be have been able to accomplish my Ph.D.

I express my special gratitude to our collaborators Dr. Chun Zhang, Dr. Robert N. Barnett, and Prof. Uzi Landman from the School of Physics, who performed ab-initio structure and conductance calculations related to our experiments on breaking and formation of niobium contacts and nanowires. These simulations were performed at the Center for Computational Materials Science at Georgia Tech and the National Energy Research Scientific Computing Center (NERSC).

I am indebted to Prof. Vitaly Shumeiko and Dr. Åke Ingerman, both from Chalmers University, Sweden, for their simulation code of superconducting point contacts transport curves used in the analysis of the experiments .

I am grateful to Prof. William King in the School of Mechanical Engineering for being my co-advisor during the duration of my 2004 Nanoscale Science and Technology (NaST) fellowship as well as for his advice during the early stages of the samples development process.

I want to thank Dr. Jie Diao, who recently graduated from the School of Chemical Engineering. He helped me a lot in making me familiar with the equipment in the MiRC cleanroom and coached me in the area of microfabrication. I also want to thank Dr. Armando Anaya and Prof. Dragomir Davidovic who taught me how to use e-beam lithography tools.

I have had a lot of fun working in the same lab with Brandon Donehoo, John "Brooks" Howard, Sanjay Bidasaria, and Dan Benjamin. I especially appreciate all the LabView data acquisition programs written by Brandon. Thanks to Yan Yi, Jianfei Shao, Zhimin Song, Xuebin Li, Tianbo Li, and Yaguang Wei for all different kinds of advise, support, and

assistance.

This research was supported in part by Georgia Tech through the Nanoscience/Nanoengineering Research Program (NNRP) and the NSF CAREER Grant No. DMR - 0349110.

TABLE OF CONTENTS

LIST OF FIGURES

SUMMARY

In this thesis I discuss development and fabrication of thin-film niobium (Nb) mechanically controlled break junctions (MCBJs) and resistively shunted niobium mechanically-controlled break junctions (RS-MCBJs) (see Ch. 2). Using these devices, high-stability atomic-size contacts (ASC) were routinely produced and investigated both in the normal and superconducting states.

In the smallest Nb ASC, completely reversible mechanical manipulation of the electronic states was demonstrated and related to specific atomic configurations (Ch. 3). This ubiquitous "elastic" regime includes switching between two states with distinct electronic properties (high-conductance or HG and low-conductance or LG states), which occurs via random telegraph noise (RTN). First-principles density functional (DFT) structural optimizations and conductance calculations using the non-equilibrium Green's functions (NEGF) method reproduce and explain the measurements (these ab-initio numerical simulation techniques are briefly overviewed in appendix A). In particular, the observed conductance bistability was associated with formation of a niobium dimer between the opposing electrodes, with the dimer shuttling between a symmetric high-conductance and an asymmetric low-conductance configurations in the gap. This system is very promising in regard to the emerging research areas dealing with coherence in nanoscale devices and the interplay between electronic, mechanical, and thermal degrees of freedom in atomic-size contacts and wires. The evidence of the interaction between the electronic current and the mechanical properties of the dimer configuration is reported in Ch. 5; suggestions are also given for future experiments involving the interaction between the Josephson radiation intrinsic to the superconducting weak link formed by the dimer system and its mechanical modes.

For the first time, resistively shunted MCBJ, using tantalum shunts, were produced and incorporated into a special-purpose composite microfabricated superconducting device,

whose state can be controlled by the temperature as well as mechanical manipulation (see Ch. 4). Embedding resistive shunts close to a junction affects the electronic transport properties of Nb ASC. In particular, the subgap structure in the current-voltage characteristics (the spectrum of multiple Andreev reflections, MAR) shifts to lower voltages. We are not aware of a theory which addresses our experimental situation directly; however, similar changes in the MAR spectrum were predicted to be caused by various pair-breaking effects which affect the coherence of the electronic transport through superconducting quantum point contacts (QPCs). Nevertheless, we found that the the formalism, based on superconductivity, which is used to characterize transport properties of atomic-size contacts without resistive shunts remains applicable for sufficiently high shunt resistances. Complementary experiments (see Ch. 5 and Ch. 1) revealed the temperature-independence of the electronic structure of atomic-size contacts, which allows one to perform quantum phase-biased transport experiments in the resulting RF SQUID configuration with the fully characterized Nb atomic contact serving as a weak link.

Finally, in Ch. 5, the behavior of niobium atomic-size contact in magnetic fields, at elevated temperatures, and high bias voltages is described. Directions for further research based on the observed experimental properties are suggested. In particular, point contact spectroscopy (PCS) experiments in both the normal and the superconducting states are suggested to establish the correlation between the observed phenomena with the atomic structure of contacts and nanowires as well as their electronic state.

CHAPTER I

INTRODUCTION

One of the driving forces behind studying of the structural, electronic, and thermal properties of micro- and nano- structures and devices is the continuing miniaturization of electronic elements in conjunction with increasing demands on performance, energy consumption, and reliability. On the scale where the physical size of electronic elements and/or their interconnects approaches one of the characteristic lengths in the materials, there are observable changes in the transport of the electric charge, which affect the overall performance of the circuits. Three fundamental length scales are: elastic scattering (phase coherence) length, l_e, inelastic scattering length, l_i, and the Fermi wavelength, λ_F (typically, $\lambda_F \ll l_e \ll l_i$). These lengths must be compared to the characteristic size W of the device in order to choose the appropriate electronic transport model. Practical microelectronic elements have yet to reach dimensions comparable to the Fermi wavelength of charge carriers. However, there is substantial research activity at this length scale in both fundamental science and for potentially creating fundamentally different electronic devices and circuits. This field (sometimes referred to as "molecular electronics") involves studying and potential utilization of *quantum* effects which emerge at this scale. One of these effects is the omnipresent quantization of the electronic conductance.

This chapter starts with description of the exact conductance quantization in two-dimensional electron gas (2DEG) quantum point contacts (QPC), where the ballistic case is realized, i.e. scattering is negligible: $\lambda_F \sim W \ll l_e, l_i$ (Figs. 1 and 2). The foundational Landauer-Imry scattering approach [51, 52, 39], which includes elastic scattering ($\lambda_F \sim W \leq l_e \ll l_i$) is introduced in Sec. 1.2. In this model, the electronic transport through a QPC is described in terms of a few independent *conductance channels*, each of them characterized by a phenomenological transmission coefficient, τ_j ($0 < \tau_j \leq 1$). The key prediction stipulates that the total electronic conductance is $G = G_0 \sum_{j=1}^{N} \tau_j$, where

G_0 is the *conductance quantum* ($G_0 \equiv 2e^2/h \approx 1/12906\ \Omega^{-1}$) and N is the number of conductance channels a particular QPC accommodates. The complete set of transmission coefficients, $\{\tau_j\} \equiv \{\tau_1, ..., \tau_N\}$ (conductance channel composition, CCC or C^3) is also the kernel of the theoretical description of other electronic properties of QPCs, such as shot noise, thermopower, etc. Numerous experiments have confirmed the universality of the model for a variety of electronic (see review by Agraït *et al.* [1]), thermal [81], and even photonic [61] systems.

The Landauer-Imry approach is of great importance in theoretical description of transport through individual molecules, nanowires, etc. High-quality semiconductor structures are intermediate between the atomic and the macroscopic scale, and are referred to as *mesoscopic* systems. Their characteristic property is the low density of charge carriers, which implies that carries behave as almost free particles, insensitive to the underlying structure of the host semiconductor material. The situation is very different for atomic-size contacts and molecular electronic devices, where a detailed modeling of the atomic structure of both the constriction ("device") area (which, e.g., may contain a single molecule or atom) and the electrodes is crucial for the correct description of the electronic properties of the device. Such a microscopic description is provided by the Density Functional Theory (DFT) [37, 44], which supplies the foundation for the accurate quantum mechanical numerical modeling of atomic structures. In appendix A, I briefly overview DFT and show how the Non Equilibrium Green's Functions (NEGF) technique [19] is used to solve the DFT equations and determine the electron current. The combination of DFT structural optimization and NEGF electron transport calculations is the most advanced technique for numerical modeling of electronic transport in nanoscale systems. In Ch. 3, I demonstrate the application of these methods to simulations of transport in the smallest niobium contacts. One of the key criteria for the comparison of the DFT/NEGF theory with the experiments is matching of the conductance channel composition, which is readily available from the numerical simulations.

In Sec. 1.3, I review the two experimental methods used in producing metallic atomic-size contacts and wires and for performing electronic transport experiments on them. These

methods also furnish a versatile test-bench for various single-molecule electronic devices. The first one is based on a modified scanning tunneling microscopy (STM) principle. The second one is the mechanically controlled break junction (MCBJ) technique; it is the latter method which was used in all the experiments described in this thesis. Some experiments which illustrate the capabilities of these techniques are described in Sec 1.3.3.

In Sec. 1.4, I describe the relevant theory and the only reliable experimental method of establishing the conductance channel composition of a QPC. This method involves measuring current-voltage (IV) characteristics of atomic-size conductors made of superconducting metals [80, 78, 58], which are subsequently fitted with a series of numerically-generated model curves [3, 13, 17], each of them representing a single conductance channel with the transmission coefficient τ_j. Finally, in Sec. 1.4.3, I describe our implementation of this technique to niobium atomic-size contacts (also see Ref. [18]) and in Sec. 1.4.4 I discuss temperature-independence of the conductance channel composition.

1.1 Conductance Quantization in Quantum Point Contacts

Powerful demonstration of conductance quantization has been made possible by the development of techniques capable of producing semiconducting structures made from layers whose thickness can be as small as a nanometer. Further advances have been made using techniques that allow these effectively two-dimensional systems (two-dimensional electron gas, 2DEG) to be formed into quantum wires (QWRs), one-dimensional (1D) systems, in which electron motion is essentially restricted to one direction, and quantum dots (QDs), zero-dimensional (0D) systems, with their discrete electron energy level spectrum, which exhibit atom-like electron configurations (artificial atoms) [86]. Furthermore, coupled QDs can behave like artificial molecules [77].

For 2DEG devices larger than both the mean free path and the phase coherence length, electron transport is well described by classical, diffusive models. Current commercial semiconductor devices are usually in this limit. For smaller electronic devices, however, quantum mechanics plays an increasingly dominant role. This regime, often referred to as mesoscopic physics, (between microscopic and macroscopic), has been an area of active

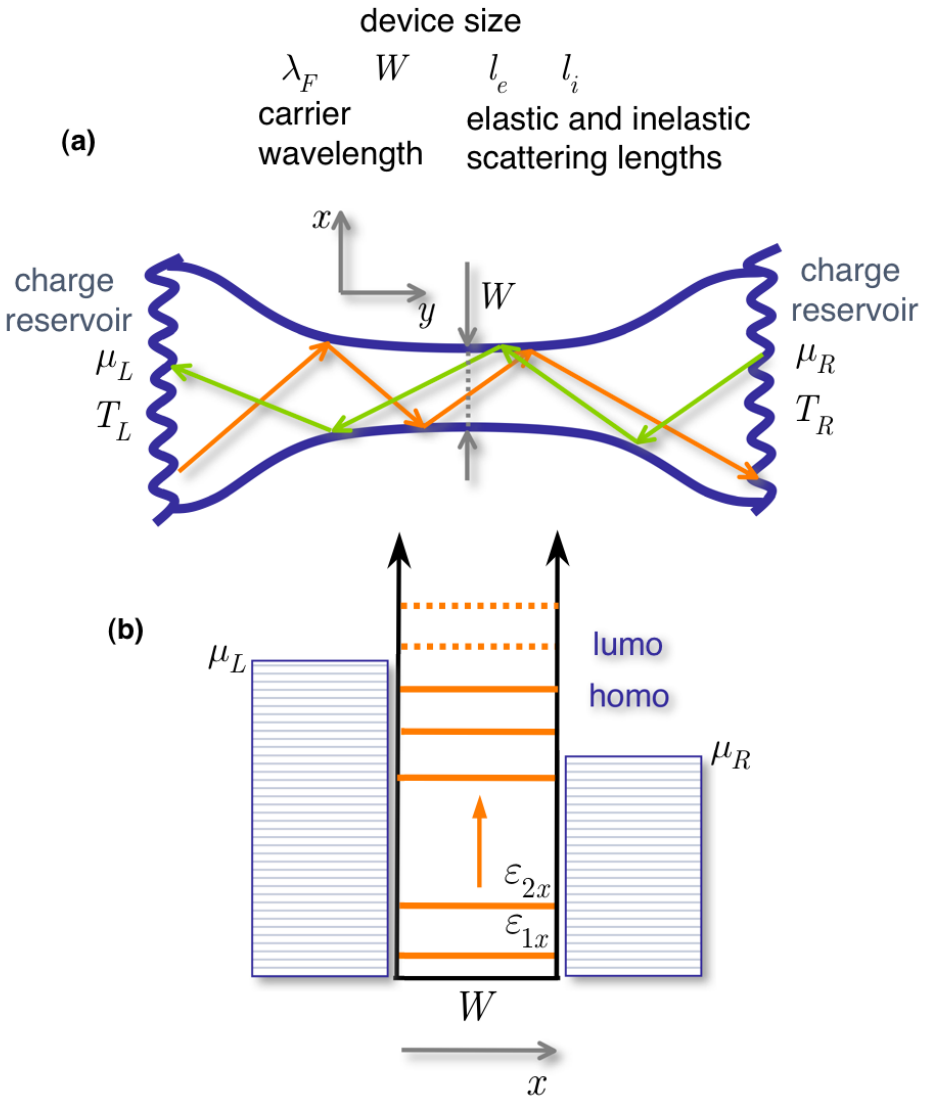

Figure 1: Toy model of the transport through a mesoscopic or a molecular conductor. (a) In the ballistic regime, there is no scattering inside the conductor; consequently, the total conductance is the net difference between the charge fluxes supplied by the charge reservoirs, which depend on the chemical potentials $\mu_{L,R}$. (b) If the width of the conductor W is comparable with the Fermi wavelength λ_F, the amount of current in such a conductor does not depend on the number of electrons. It is the amount of states around the Fermi energy that determines how much current flows. "homo" and "lumo" stand for highest occupied molecular orbital and lowest unoccupied molecular orbital, respectively. In molecular electronics, they correspond to the first molecular energy level just below (homo) and just above (lumo) the Fermi energy, respectively. Coupling to electrodes, temperature, and other factors broaden the molecular levels, thus transforming a quantized energy spectrum to a continuous "density of states" depiction.

research for the past two decades: a wide variety of novel, interesting physical phenomena have been discovered and investigated. These include the Quantum Hall Effect, Quantum Chaos, Tunable Point Contacts (with resulting Conductance Quantization), and Quantum Dots (which illustrate Coulomb Blockade) [26, 39].

2DEG quantum wires are formed by confining the motion of the electrons in the direction orthogonal to the current flow direction. A commonly used technique is that of the split gate (see Fig. 2), which allows the QWR width to be varied [89, 106]. The conductance quantization was first observed in a 2DEG device [96, 98]. A typical 2DEG quantum point contact (QPC) device is shown in Fig. 2(a). As the width of the contacts increases, the conductance increases stepwise, with each step height exactly equal to the conductance quantum $2e^2/h$. This textbook example (van Wees *et al.* [96] were cited 1533 times as of November, 2006) illustrates that due to spatial confinement of the motion in a constriction, the energy spectrum of charge carriers acquires a quantized component. Changes in the confinement potential, such as the one induced by the split gates, alters the spectrum of the quantized component, including expulsion of energy levels as the width of the channel decreases. In the conductance curves, this translates into the drop in the conductance by $2e^2/h$, which is equal to the conductance of a single ballistic conductance channel. For more detailed treatment of this adiabatic transport model see Refs. [39, 26, 19].

1.2 Transport in Quantum Point Contacts: Scattering Approach

In atomic-size conductors, formed by either the STM or MCBJ techniques described below, conductance steps were also observed as the conductors are elongated or compressed as shown in Fig. 6(a) and the inset in Fig. 7. However, the conductance quantization should be distinguished from rearrangements of the atomic structure of the contact, which, according to the classical Ohm's law will alter the conductance as:

$$G = \delta \frac{S}{L}, \tag{1}$$

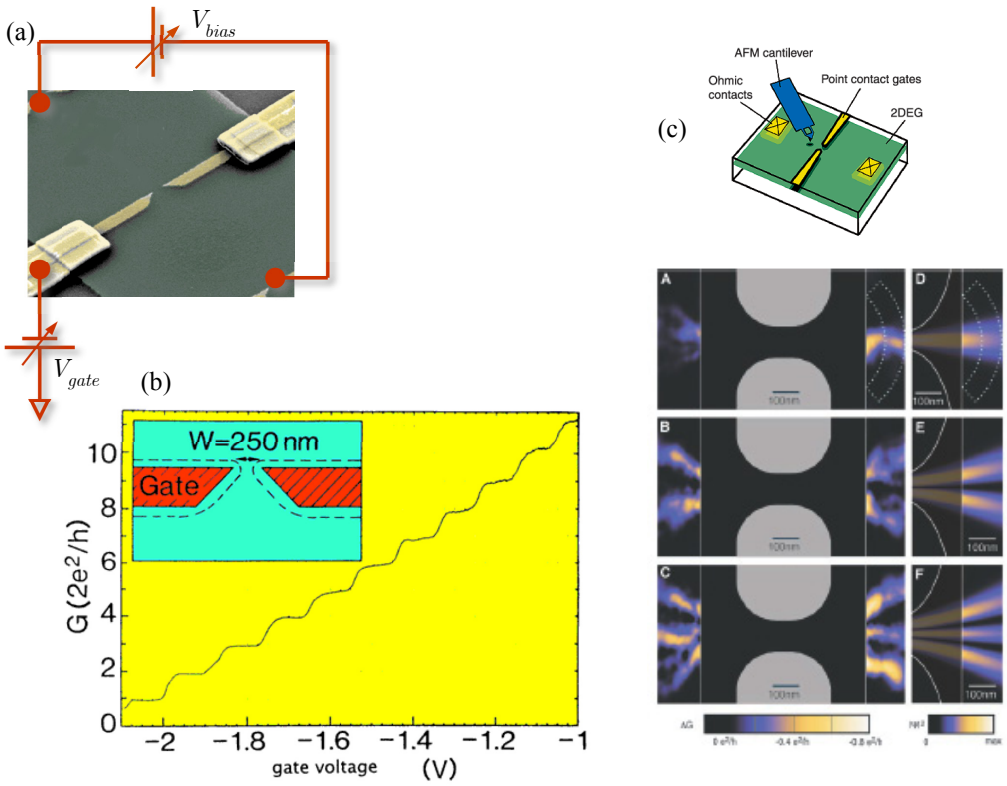

Figure 2: (a) Layout and measurement schematic of a 2DEG device. The bias voltage on the splitting gate (gold color) will repel charge carriers underneath and in the immediate vicinity, therefore, controlling the width of the narrow constriction. (b) Quantization of the conductance of a quantum point contact. Upon increasing the width of the opening (by varying the voltage on the gate electrode shown in the inset), the conductance increases stepwise. The step height of $2e^2/h$ depends only on fundamental constants of nature. (From van Wees *et al.* [96]; similar results were published by D. A. Wharam *et al.* [98]). (c) Illustration of application of AFM to studies of the transport through a 2DEG point contact (From Topinka *et al.* [91]). By simultaneously scanning the negatively charged AFM tip over the surface and measuring the conductance of the sample, one can image the current flow in the 2DEG (top panel). The bottom panel shows the electron flow from the first three modes of a QPC. Moving from top to bottom the QPC is opened from the 1st to the 2nd and then the 3rd mode. As each new mode is added new branches of current appear. Also, the images are decorated by interference fringes spaced by half the Fermi wavelength. These are due to constructive and deconstructive backscattering of electron waves from the tip back through the QPC. They demonstrate that coherent electron wave flow is being imaged.

where S is the wire's cross-section area, L is the length, and δ is the electrical conductivity. Experiments by Krans *et al.* on sodium wires [48] gave real evidence for the presence of quantized atomic channels. However, in metallic atomic size contacts, it is necessary to understand that each conductance channel (j) is characterized by a transmission coefficient τ_j, which accounts for the probability of an electron to be elastically back-scattered in the contact. The illustration is given in the top panel of Fig. 3, which represents the simplest case of the Landauer-Imry scattering model [51, 52, 39]. In this model, the left and right charge reservoirs (or electrodes) emit electrons which propagate as plane waves towards the sample (coherent scatterer) along the leads. The electrodes emit electrons with an energy distribution corresponding to the electrochemical potentials μ_L and μ_R, respectively. Electrons reflected from the sample are perfectly absorbed by the reservoirs. The leads are considered to be perfect (without scattering), and contain one or more conductance modes, whose number in the left and the right leads, N_L and N_R, respectively, are not required to be equal.

If there is only one conduction mode (top panel in Fig. 3), the amplitudes of incident and outgoing (scattered) waves are related by a (energy dependent) scattering matrix $\hat{S}$:

$$\begin{pmatrix} \hat{b}_1 \\ \hat{b}_2 \end{pmatrix} = \begin{pmatrix} r & t' \\ t & r' \end{pmatrix} \begin{pmatrix} \hat{a}_1 \\ \hat{a}_2 \end{pmatrix} \equiv \hat{S} \begin{pmatrix} \hat{a}_1 \\ \hat{a}_2 \end{pmatrix} \tag{2}$$

In the most general case of multi-mode leads, a wave occupying each mode can be transmitted through any mode in the opposite lead or be scattered onto any mode in the same lead (middle panel in Fig. 3). The scattering matrix then takes the form [14, 7]:

$$\hat{S} = \begin{pmatrix} \hat{s}_{11} & \hat{s}_{12} \\ \hat{s}_{21} & \hat{s}_{22} \end{pmatrix} \equiv \begin{pmatrix} \hat{r} & \hat{t}' \\ \hat{t} & \hat{r}' \end{pmatrix}, \tag{3}$$

where $\hat{s}_{\alpha\beta}$ is a $N_\alpha \times N_\beta$ matrix whose components $(\hat{s}_{\alpha\beta})_{mn}$ are the ratio between the outgoing amplitude of mode n in lead α and the incoming amplitude on mode m in lead β.

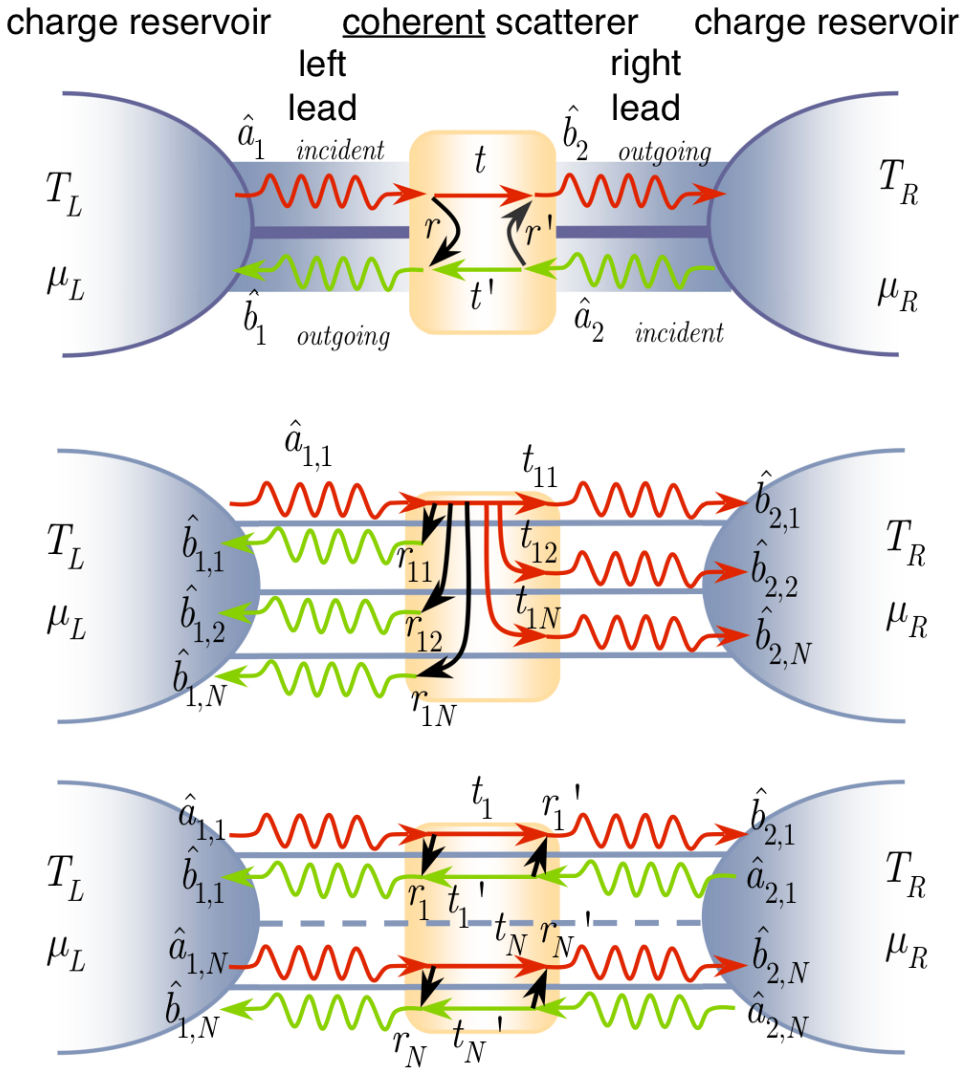

Figure 3: Illustration of the Landauer-Imry scattering approach. (top) Formation of the incident and outgoing states in the simplest case of a single mode in each of the leads. (middle) The most general scattering case, where an incident electron (e.g., $\hat{a}_{1,1}$) has finite probabilities for being transmitted onto any of the modes in the opposite lead, or being scattered onto any of the modes in the same lead. In this panel, the same number of modes, N, is drawn in both leads. (bottom) By a unitary transformation, the problem can be reduced to N independent scattering problems, making the total conductance the sum of conductances of independent eigenmodes (conductance channels).

The current on mode m of lead α is due to the imbalance between the *population* of the incoming and outgoing states by the two electrodes and is given by [14]:

$$I_{m\alpha} = \frac{2e}{h} \int_{-\infty}^{+\infty} d\varepsilon \left[\left\langle a^{\dagger}_{m\alpha}(\varepsilon) a_{m\alpha}(\varepsilon) \right\rangle - \left\langle b^{\dagger}_{m\alpha}(\varepsilon) b_{m\alpha}(\varepsilon) \right\rangle \right]. \tag{4}$$

This equation is written in terms of creation and annihilation operators $a^{\dagger}_{m\alpha}(\varepsilon)$ and $a_{m\alpha}(\varepsilon)$, which create and destroy an incoming electron on mode m in lead α with energy ε. Similarly, creation and annihilation operators are written for the outgoing states $b^{\dagger}_{m\alpha}(\varepsilon)$ and $b_{m\alpha}(\varepsilon)$.

Since $b_{m\alpha} = \sum_{n\beta} \left(\hat{s}_{\alpha\beta}\right)_{mn} a_{n\beta}$ and the population of the incoming modes is fixed by $\left\langle a^{\dagger}_{m\alpha}(\varepsilon) a_{m\alpha}(\varepsilon) \right\rangle = \delta_{mn}\delta_{\alpha\beta} f_{\alpha}(\varepsilon)$, where $f_{\alpha}(\varepsilon)$ is the Fermi distribution of the electron reservoir connected to lead α, the current $I_{m\alpha}$ can be expressed in terms of the components of the scattering matrix. Adding contributions from all the modes, the current in lead 1 is given by:

$$I_1 = \frac{2e}{h} \int_{-\infty}^{+\infty} d\varepsilon (f_1(\varepsilon) - f_2(\varepsilon)) Tr\left(\hat{t}^{\dagger}\hat{t}\right) \tag{5}$$

Therefore, the linear response conductance (bias voltage $V \ll E_F$) at $T = 0$ K is given by:

$$G = \frac{2e^2}{h} Tr\left(\hat{t}^{\dagger}\hat{t}\right) \tag{6}$$

Due to Hermicity and unitarity, the matrix $\hat{t}^{\dagger}\hat{t}$ has N_1 *real* eigenvalues τ_j and can be diagonalized. This calculation may be followed by producing eigenvectors of $\hat{t}^{\dagger}\hat{t}$, called *eigenchannels*, each of which is a linear combination of the originally considered incoming modes. This transformation removes the channel mixing shown in the middle panel in Fig. 3. In the basis of eigenchannels, the transport problem is reduced to the superposition of independent single scattering problems without any coupling (see bottom panel in Fig. 3). The expression for the linear response conductance is then given by the famous Landauer formula:

$$G = G_0 \sum_{i=1}^{N} \tau_i, \text{ where } G_0 \equiv \frac{2e^2}{h} \approx \frac{1}{12906\ \Omega}. \quad (7)$$

1.3 Production of Atomic-Size Contacts and Nanowires

There are three major methods of producing atomic-size contacts. The first method is based on the scanning tunneling microscopy (STM) technique. The second method is the mechanically controllable break junction (MCBJ) technique. The last method is based on chemical anodization of notched wires [27]. Because of contamination problems, the last technique is rarely used in quantum transport experiments.

1.3.1 Scanning Tunneling Microscope Method

The possibility of forming atomic-size contacts and wires using scanning tunneling microscopes was predicted theoretically by Landman *et al.* in 1990 [53]. Their molecular dynamics simulations are illustrated in Fig. 4(a) and (b). Simulations predicted that gently crushing a tip into a metallic crystal surface will cause atoms from the crystal to migrate and adhere to the tip. Subsequent pulling of the tip away from the surface creates strong necks (nanowires), which change their structure by rearranging atoms as the nanowire is elongated. Early experiments on single atom positioning [24] with STM tips and STM-based atomic switches [23] qualitatively confirmed the validity of the concept proposed in the simulations.

In one of the most famous experiments on STM-formed ASCs, Ohnishi *et al.* [66] performed conductance measurements while observing the break up process in a high-resolution transmission electron microscope (HRTEM) (Fig. 4(c)). In those measurements, jumps in conductance were related to changes in the atomic configuration of the nanowires. In the smallest contact formed by two- and one- atom wide strands, the corresponding conductance was close to two and one conductance quanta ($2e^2/h$), respectively.

There are several drawbacks related to this method. Firstly, this method requires very good insulation from mechanical vibrations. Secondly, it is relatively difficult to construct a STM running at low temperature. Lastly, there is a possibility for contaminating the

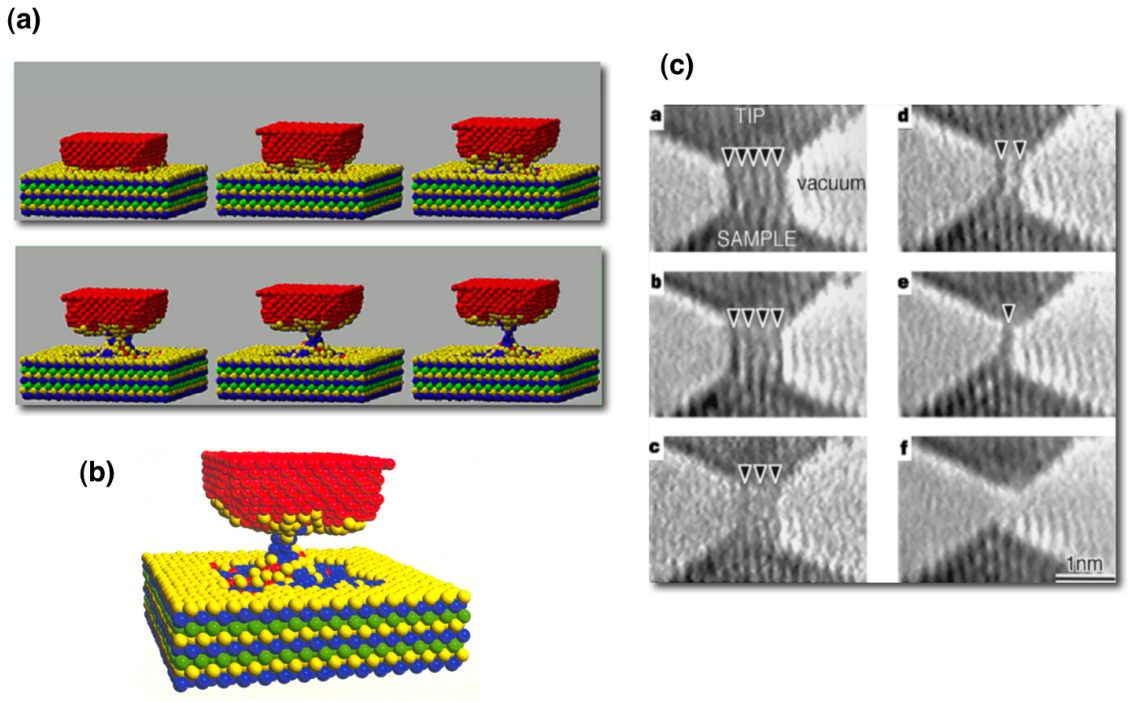

Figure 4: (a),(b) Molecular dynamics simulation shows the process of a Ni tip pulling away from a Au substrate [53]. The cross section of Au contact is decreasing as the tip is pulling away (courtesy by Prof. Landman) (c) Direct high-resolution transmission electron microscope imaging of a pulling process [66] showing thinning of the nanowire starting from 5 linear threads of Au atoms until the direct contact is broken up. Simultaneous conductance measurements suggested that two- and one- atom wide contacts had the conductances of two and one conductance quanta. While this appears to be common in gold, this is not the case for almost any other metal.

contact area since the tip and the substrate are usually prepared independently.

1.3.2 Mechanically Controlled Break Junction Method

The concept of a break junction was first introduced by Moreland and Ekin [62]. This technique was further improved by Muller *et al.* [63], and christened the "mechanically controlled break junction (MCBJ) technique". The basic setup of MCBJ is shown and explained in Fig. 5. It is relatively easy to construct and operate a sample made of a manually notched thin wire (Fig. 5(b)). However, the stability and the degree of precision in manipulating the sample are inferior to microfabricated samples such as the one shown in Fig. 5(a). The calibration procedure allowing to determine the sample elongation in real units is discussed in Sec. 2.3. Besides stability, precision, and cleanliness of contacts freshly broken in ultra-high vacuum conditions at low temperatures, microfabricated break junctions can be incorporated into circuits with other microscopic elements in the immediate vicinity. Our novel composite superconducting circuit, which includes a niobium break junction, and its operation are described in Ch. 4.

1.3.3 Conductance Quantization in Metallic Atomic-Size Contacts: Conductance Histograms

Analysis of experiments, where conductance is recorded as atomic-size contacts are elongated and/our compressed, usually involves construction of conductance histograms, made of the magnitude (and sometimes length) of the flat segments (plateaus), which appear in the conductance evolution traces (see Fig. 6(a)). Building a representative histogram requires processing data from several thousand traces. By virtue of its chemical inertness, gold has become the material of choice for early studies of the quantization of conductance in atomic-size contacts. Due to the relative simplicity of conductance measurements on gold, many groups, using various set-ups, built conductance histograms for different temperatures and various ambient conditions (see an example in Fig. 6(b)). Despite of some discrepancies in observations by different groups, one feature remains reproducible in all those experiments, namely the presence of a sharp peak at almost exactly one conductance

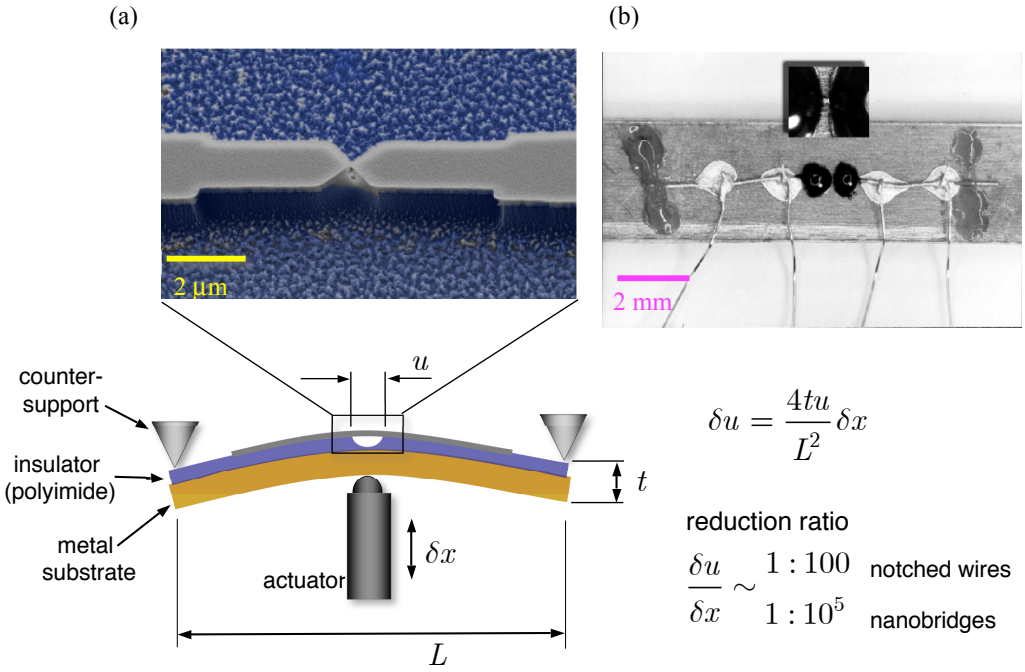

Figure 5: (a) The schematic setup of a mechanically controllable break junction (MCBJ). A notched wire or a thin-film sample is attached to the top of an insulator-covered flexible substrate. This substrate is bent in a three-point support by pushing from underneath. On top of the schematic, there is a colorized electron micrograph of a microfabricated sample produced in our group. Blue color corresponds to the insulating polyimide substrate. (b) Top view of a manually notched wire sample (from Ref. [1]). The substrate is 4.5 mm wide and the sample wire is a 0.1 mm diameter gold wire. The wire is glued on top of an insulator-covered bronzed plate by two drops of Stycast 2850 on each side of the notch. The inset shows an enlargement of the wire with the notch between the two drops of epoxy. The distance between these two drops of Stycast can be made as small as 0.1 mm.

quantum, seen at all temperatures (Fig. 6(b)). It is natural to suggest that this peak corresponds to the smallest contact which consists of a single atom or, as observed by Ohnishi *et al.* [66], by a single-atom chain. Other pronounced peaks in the histograms are believed to correspond to other frequently encountered contact atomic configurations. Nevertheless, interpretation of other peaks and the total structure of histograms is much less obvious even for gold, and requires microscopic modeling (see Ch. 3).

For elements, whose chemical nature is different from gold, the histograms are vastly different as well. A histogram for niobium and vanadium is shown in Fig. 7. This plot gives a clear illustration that histograms are alike for elements whose electronic structures are similar. On the other hand, the most common atomic configurations do not have conductances near the conductance quantum, or one of its integers. Again, microscopic modeling, which takes into account chemical bonding between the atoms forming contacts is required. In chapter 3, I describe a synergetic experiment-theory study, which allowed us to identify the atomic configuration of the smallest niobium contact as a dimer (Nb_2 "molecule") suspended between two bulk electrodes.

The fact that conductance steps in metals are not equal to integers of the conductance quantum is in a perfect accord with the Landauer formula (Eq. (7)). It is understood that, due to disorder, ASCs contain imperfect conductance channels, with transparencies $\tau_j < 1$. However, the conductance channel composition can not be determined from the conductance versus elongation curves, since there is not enough information in those traces that allows to select a certain CCC out of an infinite number of possibilities. The only known method which allows to deciphering of the CCC is based on transport measurements in the superconducting state.

1.4 Transport in Superconducting Point Contacts

In this section, I discuss electronic transport in a system consisting of two superconductors weakly coupled to each other. This means that two superconductors are separated either by a narrow tunnel gap (either vacuum or filled with an insulator) or are connected by a small (in comparison with the superconductor's coherence length) conducting constriction.

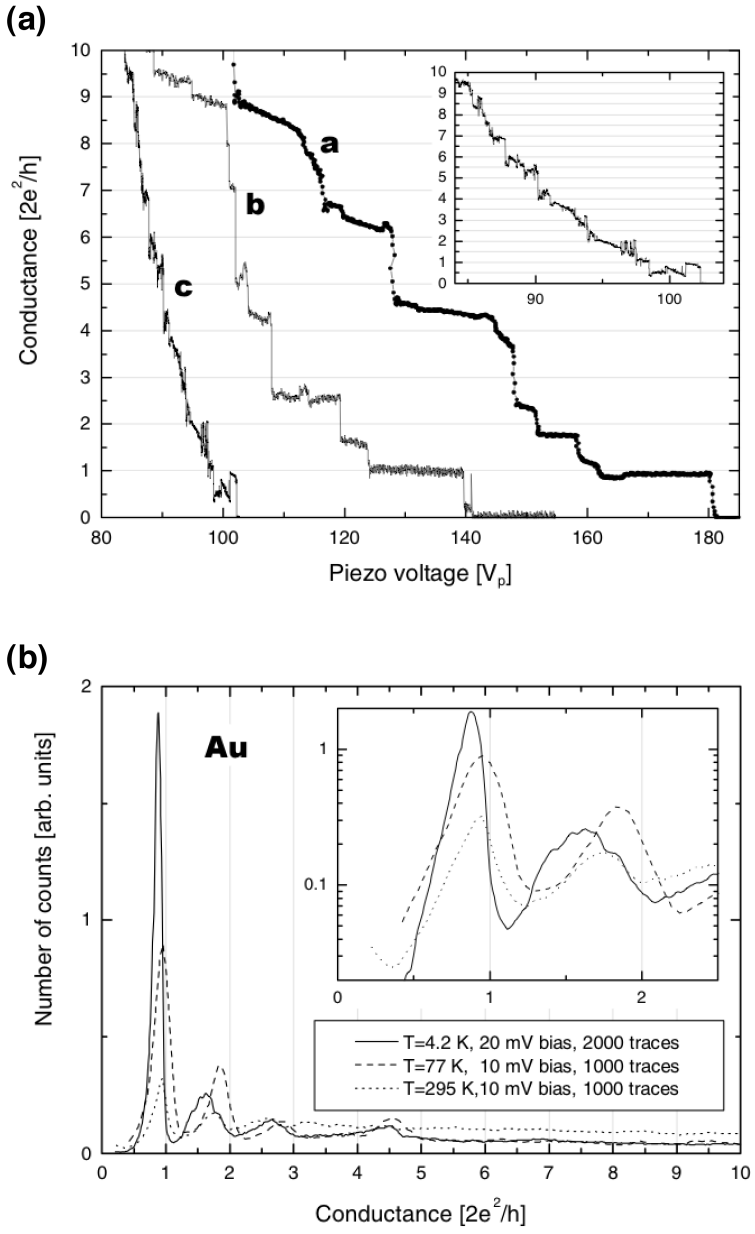

Figure 6: (Adapted from Ref. [100]) (a) Conductance as a function of piezo voltage recorded on gold MCBJ at liquid helium(**a**), liquid nitrogen (**b**), and room temperature (**c**). Inset shows the room temperature trace on the expanded scale. (b) Conductance histograms of gold at different temperatures. Inset shows the first peaks on the expanded scale.

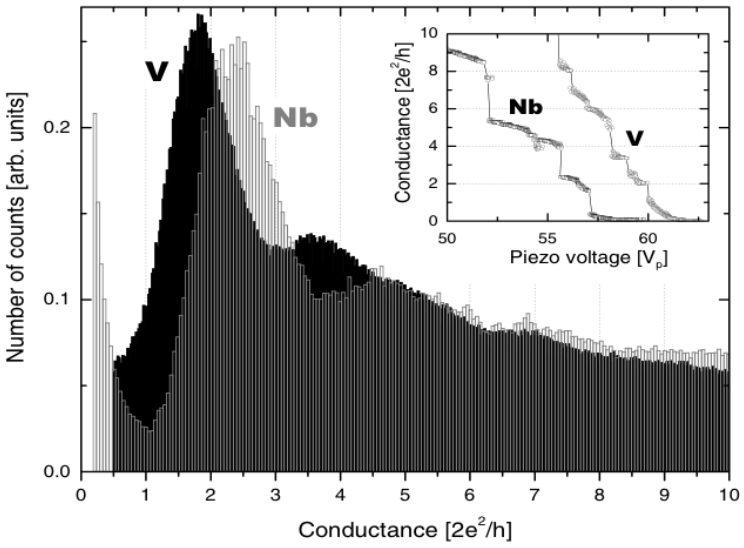

Figure 7: (Adapted from Ref. [100]) Conductance histograms of vanadium (black) and niobium (gray) composed of 58000 and 1200 individual conductance traces, respectively. Typical conductance traces for both metals are hown in the inset. The samples were notched-wire MCBJs. For niobium, there is a single broad peak centered at $\sim 2.5\ G_0$ (also, see Ref. [58]).

Transport in a superconductor-insulator-superconductor (SIS) system is described by the famous Josephson relations. If the superconductors are coupled by a weak link (i.e. a microscopic normal metal bridge, 2DEG, a carbon nanotube, or any other constriction, forming a superconductor-constriction-superconductor (ScS) junction), specific models must be developed for each of these cases. Atomic-size contacts and nanowires, formed from superconducting materials sandwiched between two bulk superconductors, behave as if the constriction is made of a normal metal. Transport properties in these superconductor-normal metal-superconductor (SNS) junction are governed by *Andreev reflection* and *multiple Andreev reflection* processes (Sec. 1.4.1 and 1.4.2). Similar to normal metal point contacts, the mesoscopic N-constriction can behave as an elastic scatterer with a certain conductance channel composition (CCC). In Sec. 1.4.2, the relevant models of electronic transport are discussed. In Sec. 1.4.3, I explain the method for deriving the CCC from low-voltage IV characteristics of superconducting constrictions containing a few atoms. An important property, temperature independence of the CCC, will be demonstrated in Sec. 1.4.4.

1.4.1 Josephson Effects and Andreev Reflection

In 1962, Brian Josephson considered theoretically the behavior of a pair of superconducting electrodes separated by a tunneling barrier. He has demonstrated [43] that a supercurrent consisting of Cooper pairs can flow through such a barrier, driven simply by the difference in the order parameter phases in the two electrodes, φ. This current has a simple form $I_s = I_c \sin(\varphi)$. I_c is the phenomenological critical (maximum) current, which can in some cases be calculated from microscopic parameters of the junction. This equation is known as the dc Josephson relation, and the ability of superconducting junctions to carry a supercurrent is known as the dc Josephson effect. When a voltage V is applied across the junction, φ evolves with time as $d\varphi/dt = 2e/\hbar$. Integrating this relation with respect to time and substituting φ into the dc Josephson equation yields $I_s = I_c \sin(2eVt/\hbar)$. This shows that an applied dc voltage generates an ac supercurrent with frequency $\omega = 2eV/\hbar$ (483 THz/V). This phenomenon is known as the ac Josepson effect.

While the microscopic description of transport in superconducting tunnel junctions is based on electrons tunneling through a barrier, in superconductor-normal metal-superconductor (SNS) devices, such as metallic point contacts, the microscopic description involves the process known as Andreev reflection [2] and its descendant, multiple Andreev reflections (MAR) [8, 65].

To understand Andreev reflection, consider an electron in the normal metal in contact with a superconductor (Fig. 8). The electron cannot enter the superconductor alone if its energy, E_e (measured with respect to the Fermi energy), is less than Δ, the BCS gap in the superconductor. The electron must pair with another electron, whose energy is E_e below E_F, in order to form a Cooper pair in the superconductor. The result of this process is that an electron incident onto a normal metal-superconductor (NS) boundary appears to be reflected as a hole, or vacancy in the Fermi sea (see Fig. 8(a)). Moreover, a peculiar property of such a "superconducting mirror" is that it forces the hole to retrace the electron's path, as if time is reversed. However, since the velocity of the hole is opposite to its momentum, Andreev reflection conserves the momentum of the reflected particle. In contrast, reflection at an ordinary mirror (an insulator) conserves charge, but not the momentum. Andreev

reflection is the key concept needed to understand electronic properties of nanostructures with NS interfaces [39].

The quantum mechanical description of Andreev reflection involves two Schrödinger equations for electron and hole wavefunctions $u(\vec{r})$ and $v(\vec{r})$, respectively, coupled by the superconducting pair potential $\Delta(\vec{r})$ (Bogolubov-De Gennes equations or BdG [20]):

$$\mathcal{H}_{BG} \begin{pmatrix} u \\ v \end{pmatrix} = E \begin{pmatrix} u \\ v \end{pmatrix}, \tag{8}$$

$$\mathcal{H}_{BG} = \begin{pmatrix} H & \Delta(\vec{r}) \\ \Delta^*(\vec{r}) & -H^* \end{pmatrix}. \tag{9}$$

The Hamiltonian $H = \left(\vec{p} + e\vec{A}\right)^2 / 2m + V - E_F$ is the single-electron Hamiltonian in the field of a vector potential $\vec{A}(\vec{r})$ and electrostatic potential $V(\vec{r})$. The excitation energy is measured relative to the Fermi energy E_F.

At a NS interface, the pairing potential $\Delta(\vec{r})$ drops to zero over atomic distances at the normal side. At the superconducting side of the NS interface, $\Delta(\vec{r})$ recovers its bulk value Δ only at some distance away from the interface [90]. This is neglected in the commonly used step-function model ("rigid boundary condition" illustrated in Fig. 9(b)):

$$\Delta(\vec{r}) = \begin{cases} \Delta & \text{if } \vec{r} \subset \text{S}, \\ 0 & \text{if } \vec{r} \subset \text{N}. \end{cases} \tag{10}$$

This assumption greatly simplifies the analysis without changing the results in any qualitative way. One important result, relevant for the future discussion, expresses the probability of Andreev reflection as the function of the electron energy. This probability is equal to one for $|E_{e,h}| < \Delta$ and is rapidly vanishing for $|E_{e,h}| \geq \Delta$.

1.4.2 Multiple Andreev Reflections

If a phase coherent region of normal metal is sandwiched between a pair of superconductors, the electron-hole tandem will make round trips along the same trajectory, in which they are Andreev reflected twice (once from each NS interface). The density of states in the

normal metal will break up into a discrete spectrum of bound states at energies such that the electron's phase advances 2π per round trip (Fig. 9(a)). As each roundtrip transfers a Cooper pair across the normal metal, these Andreev bound states carry supercurrent [49, 50]. Furthermore, the energies of these states depend on the phase difference between the two superconductors, $\varphi = \varphi_L - \varphi_R$ (see Fig. 9(c)). Because an electron can cross the junction in either direction, any "positive" Andreev bound state has a "negative" partner that carries the supercurrent in the opposite direction (Fig. 9(a)). When $\varphi = 0$, these states are degenerate and the supercurrent is equal to zero, however a non-zero phase difference results in a net supercurrent. This accounts for the dc Josephson effect in the SNS junctions. For further discussion please refer to chapter 4.

The study of non-equilibrium superconductivity (transport) in weak links was stimulated by the work of Octavio *et al.* [65]. This work explained features seen in the differential conductance of SNS junctions when biased at an integer fraction of the voltage $2\Delta/e$. These features are called the subgap structure (SGS). The authors introduced the concept of multiple Andreev reflections (MAR), which is now the commonly accepted transport mechanism in atomic size and other diffusive SNS junctions. The MAR concept is illustrated in Fig. 10. As an electron crosses the junction, it gains an energy eV, if this energy is less that 2Δ, which is the minimum amount to find an exited state in a superconductor, it is reflected as a hole. This hole, having the positive charge, keeps gaining energy, moving in the opposite direction. Without scattering, this chain of reflections can continue indefinitely, until either carrier's energy is high enough to enter the superconductor as an electron or hole quasiparticle. This explains sharp step-like features in IV characteristics when $V = 2\Delta/ne$, as at these voltages a new $(n-1)$-fold Andreev reflection process can reach the singularity in the quasiparticle density of states at the gap edge. While Octavio's approach captures the transport mechanism qualitatively, some important omissions, such as omitting Josephson effects, makes any quantitative comparisons unreliable.

More recent theories of transport through SNS junctions take Josephson effects into account [3, 13, 17]. It has been realized that the dynamics cannot be described by substituting the expression for the time evolution of the Josephson phase, $\varphi = \omega_0 t \equiv 2eVt/\hbar$, into a

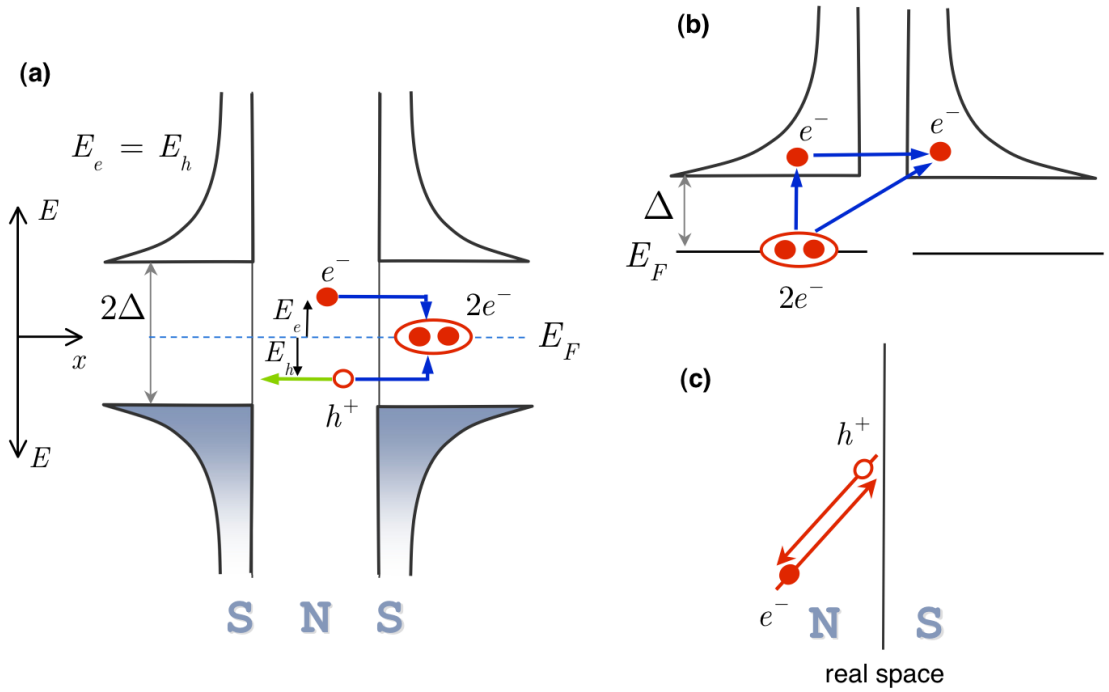

Figure 8: (a) Andreev reflection scheme at a normal metal-superconductor (NS) interface. If an electron with energy smaller than Δ hits an NS interface, it will be reflected as a hole, and a Cooper pair is generated inside the superconductor. If it is a hole, it will be reflected as an electron, and a Cooper pair will be destroyed in the superconductor. (b) Destroying a Copper pair requires the energy in excess of 2Δ. The energy can be provided by a thermal fluctuation, creating *two* electron quasiparticles. If two superconductors are in a tunneling or weak link contact, the energy necessary to destroy a Cooper pair may be provided by the bias voltage. Destruction of a Cooper pair in the left superconductor results in creation of two electron quasiparticles in the right superconductor. (c) Andreev reflection conserves the momentum, but does not conserve the charge; the electron (e^-) is reflected as a hole (h^+) with the same momentum but the opposite velocity (*retro-reflection*). The missing charge of $2e$ is absorbed as a Cooper pair by the superconducting condensate. The electron-hole symmetry is exact at the Fermi level; if the electron energy E_e is above E_F, then the hole is at the energy E_e below E_F.

current-phase relation appropriate for a given weak link (see Ch. 4) and time-averaging due to the fact that excitations of quasiparticles come into play and give the main contribution. Consequently, the total current was expanded in terms of all the harmonics of the Josephson frequency:

$$I(V,t) = \sum_n I_n \exp in\omega_0 t. \tag{11}$$

In 1995, Bratus *et al.* [13] and Averin & Bardas [3] calculated the current in a voltage-biased superconducting contact by matching solutions of the time dependent Bogolyubov-de Gennes equations with adequate boundary conditions. These conditions involved the jump of the superconducting potential Δ at two NS interfaces (Fig. 9(b)) as well as a scattering barrier with transparency τ in the middle of the N phase. On the other hand, Cuevas *et al.* [17] used a Hamiltonian approach together with non-equilibrium Green's functions techniques to obtain the current in a one-channel contact with arbitrary transmission. The result of the scattering and the Hamiltonian approach have been shown to be equivalent [17]. In both cases, the equations for the current must be solved numerically. The shape of these IV curves depends both on the transparency of the scattering barrier (Fig. 11) and other parameters, such as temperature (Fig. 12).

In order to find the conductance channel composition from experiments, one has to match the measured IV curves with a family of numerically generated model curves which give the best approximation of the experimental data.

1.4.3 Determination of the Conductance Channel Composition

Scheer *et al.* [80] were the first to demonstrate that the number and individual transmission coefficients of conductance channels can be extracted from experimental IV curves. The total current going through the junction was assumed to be the sum of currents in each individual channel:

$$I(V) = \sum_{j=1}^{N} i(V, \tau_j, \Delta), \tag{12}$$

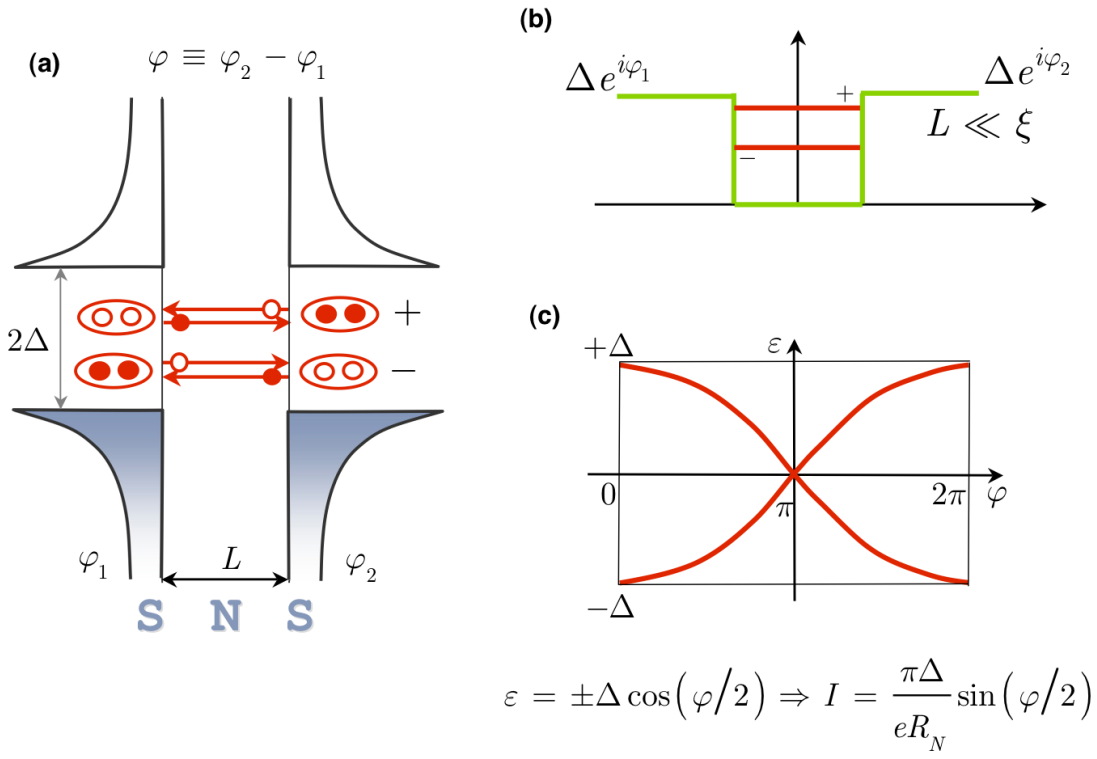

Figure 9: Multiple Andreev reflection scheme in a phase bias SNS junction. An electron with energy smaller than the gap bumps in the right NS interface will be reflected as a hole and a Cooper pair will be generated in the right superconductor. This reflected hole will bump to the left NS interface. It will be reflected as an electron and one Cooper pair will be destroy in the left superconductor. The resulting current is supercurrent.

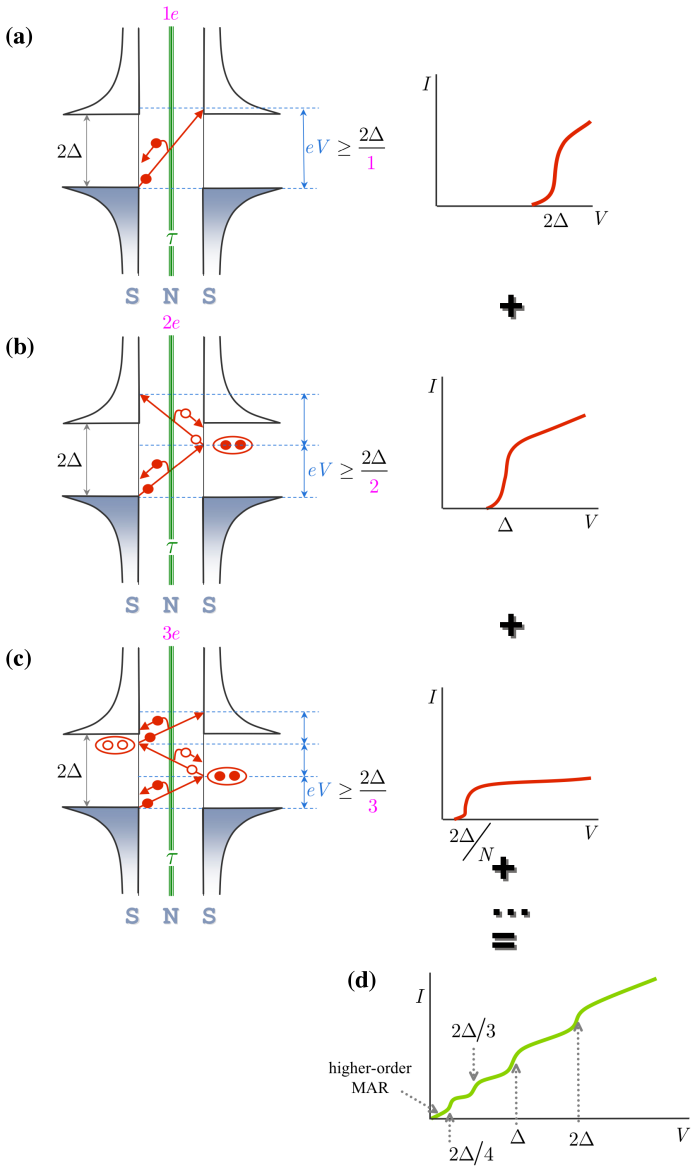

Figure 10: Multiple Andreev reflection scheme in one conductance channel of a voltage-biased SNS junction. (a) One charge transfer process ($eV \geq 2\Delta$) and the corresponding IV curve. An electron can be back-scattered, the transmission probability is τ. (b) Two-charge transfer process ($eV \geq 2\Delta/2$) requires a single Andreev reflection. Both the electron and the hole can be back-scattered; the transmission probability is τ^2 (c) Higher-order processes involve both electron and hole reflections; the transmission probability drops as τ^N. $(N-1)$ is the number of Andreev reflections. (d) The total current is the sum of the contributions of all the MAR processes.

where N is the number of conductance channels in the ASC, Δ is the superconducting gap, and $i(V, \tau_j, \Delta)$ is the current-voltage characteristic of a single channel with the transmission coefficient τ_j. Consequently, the fitting procedure, in essence, selects a set of N model curves $\tau_1, ..., \tau_N$, which minimizes the χ^2 deviation between the experimental data and the model given by Eq. (12):

$$\chi^2(\tau_1, ..., \tau_N) = \frac{1}{M} \sum_{i=1}^{M} \left(I_0(V_i) - \sum_{j=1}^{N} i(V_i, \tau_j, \Delta) \right). \tag{13}$$

In our simulations, the model $i(V, \tau_j, \Delta)$ curves are numerically generated using the code developed by Åke Ingerman and Jonn Lantz in Chalmers University, which is based on the theoretical model by Bratus', Shumeiko, and Wendin [13]. Examples of the model curves, with different transparencies, at $T = 0\ K$ are shown in Fig. 11. To have a better understanding of how the temperature affects the transport curves, a series of the model curves with the same transparency but at different temperatures are shown in Fig. 12. A skilled experimenter can tell presence of one or more high-transparency channels by looking at differential conductance curves.

To fit the experimental curves, the superconducting gap must be found first. The gap can be extracted from fitting a deep tunneling curve without any MAR features with a single-channel low-transparency theoretical curve [94]. Using Eq. (13), both τ and Δ can be found. Fig. 13 shows an example of fitting a tunneling curve of Nb ASC. The superconducting gap can also be estimated from the superconducting transition temperature. The relationship between the superconducting gap and the superconducting temperature is $\Delta = 1.76 k_B T_c$.

Once the superconducting gap is found, experimental IV curves can be normalized and fitted. Normally, I do fitting by trying all possible combination of transparencies (with the resolution of $\Delta\tau_j = 0.01$). An example of the best fit with a varying number of channels is shown in Fig. 14. The experimental curve was fitted with one conduction channel, two conduction channels, etc. The inset of Fig. 14 shows the dependence of χ^2 on the number of channels included into each fitting procedure. The fitting error stops decreasing when the number of fitting channels exceeds five. It turns out that five is the minimum number of channels necessary to obtain a reasonable fit for the smallest Nb junctions. This number

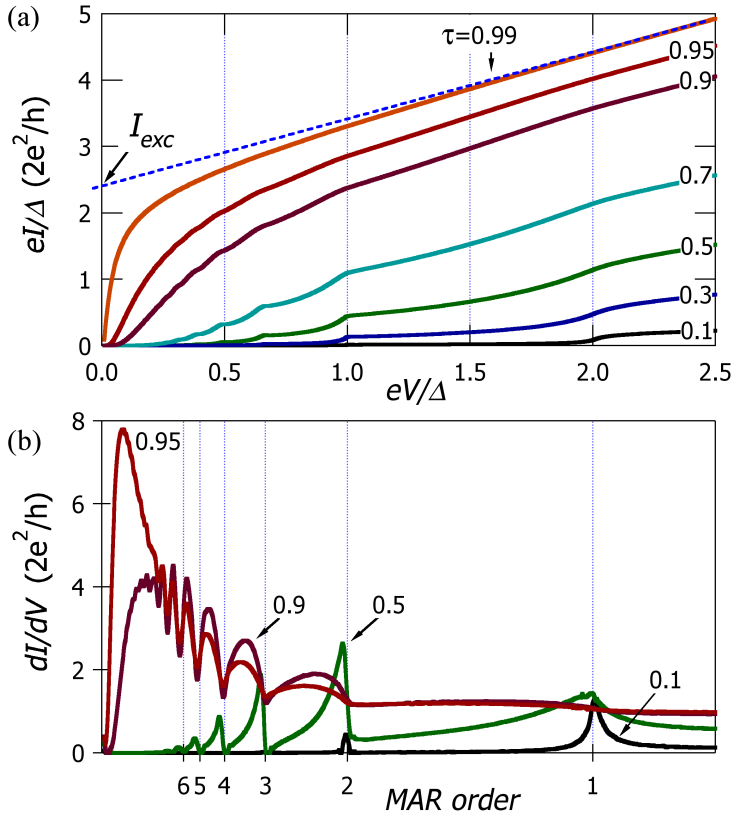

Figure 11: Theoretical IV curves of one conduction channel with different transmission probability at $T = 0$ K. These curves are generated by the computer code developed by Åke Ingerman and John Lantz in Chalmers University.

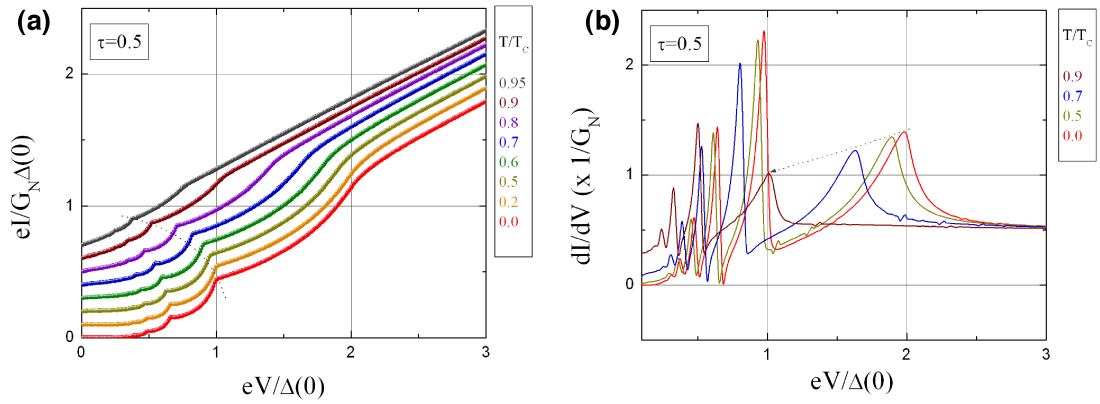

Figure 12: (a) Theoretical IV curves of a single conduction channel with $\tau = 0.5$ at different temperatures. (b) Theoretical conductance curves of a single conduction channel with $\tau = 0.5$ for different temperatures. These curves are computed from the theoretical IV curves.

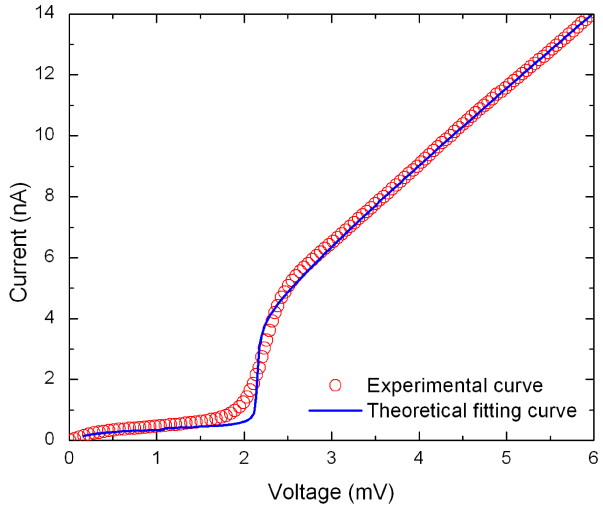

Figure 13: Curve fitting in the tunneling regime. Circles: experimental IV curve measured in deep tunneling regime (about 416 kΩ). The full line is the best theoretical fitting curve with one channel. The parameters determined from the fitting are $\tau_1 = 0.031$ and $\Delta = 1.21$ meV.

is different for other elements, for example, IV characteristics of the smallest aluminum contacts can be fitted with just three channels [78].

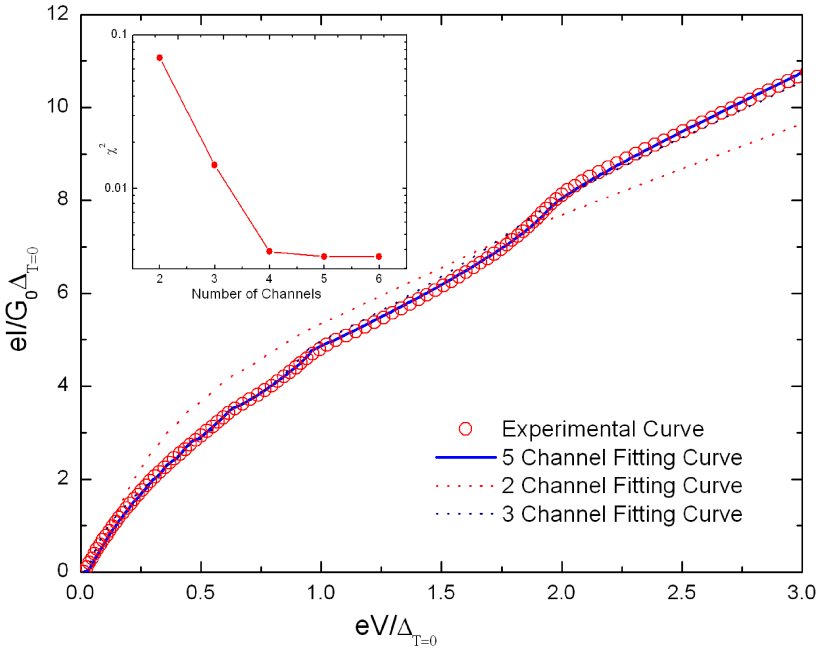

Figure 14: Curve fitting with different number of channels. Circles: experimental IV curve measured in the single-atom regime. The inset shows the dependence of fitting error and number of channels. The fitting error stops decreasing at 5 channels. This proves that the smallest Nb ASCs have 5 conduction channels.

1.4.4 Thermal Stability of the Electronic State of Atomic-Size Contacts

Since temperature plays an important role in the MAR, in this section, I show that the conductance channel composition is actually independent of temperature. Since model IV curves can be generated for an arbitrary temperature, we have tried the fitting procedure for curves acquired at several different temperatures below T_c. The measurements were performed on Nb ASC in the temperature range between 2.4 K and 8.4 K. The experimental results of IV characteristics and their corresponding theoretical fits are shown in Fig. 15. The conductance curves computed mathematically from IV measurement and their best fits are shown in Fig. 16. For temperatures up to $0.8T_c$, we find a satisfactory agreement of experimental data and theoretical fits (Fig. 15). In this range, the conduction channels

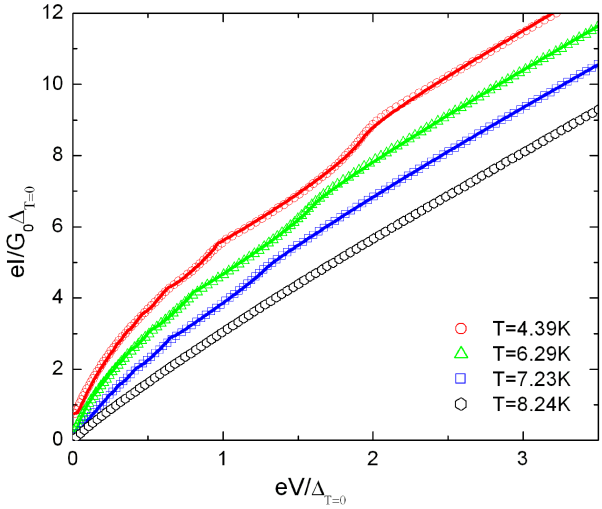

Figure 15: Normalized experimental IV curves of a Nb contact with the total conductance of $\sim 2.5\ G_0$ at different temperature. Solid lines represent best fits using Eq. (12) with five conductance channels. The gap, Δ, was estimated using the superconducting transition temperature of the niobium thin film.

composition was found to be temperature-independent within the fitting precision: $\tau_1 = 0.96$, $\tau_2 = 0.80$, $\tau_3 = 0.40$, $\tau_4 = 0.21$, $\tau_5 = 0.08$. The precision of each of these coefficients were estimated to be ± 0.02. When the temperature is increased, the subgap structure is smeared out due to the thermal activation of quasiparticles and the positions of MAR resonances are shifted due to the reduction of the superconducting gap. Above $0.8T_c$, our fitting procedure is not sufficiently sensitive. When temperature goes up to 8.24 K, the MAR features are not clearly distinguishable. Scheer *et al.* have demonstrated temperature-independence of CCC in aluminum point contacts; in the same work, they found that the conductance channel composition does not change in magnetic fields as well.

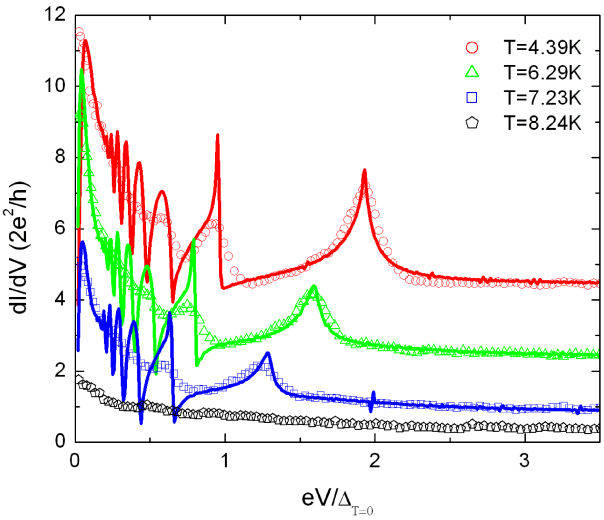

Figure 16: Normalized differential conductance (dI/dV) calculated from curves shown in Fig. 15. For clarity, $T = 4.39$ K results are shifted vertically by 2, $T = 7.23$ K results are shifted vertically by -1.5, and $T = 8.24$ K results are shifted by -2.0. Near T_c, the MAR peaks are not clearly distinguishable.

CHAPTER II

SAMPLE MANUFACTURING AND EXPERIMENTAL SETUP

In this chapter, I give a detailed description of the microfabrication procedures for manufacturing niobium break junctions with and without embedded resistive shunts (Sec. 2.1). In reality, resistive shunts are also made of a superconducting material, tantalum, whose transition temperature is lower that that of niobium (T_c = 9.2 K for Nb and T_c = 4.5 K for Ta). Therefore, at sufficiently low temperatures both Nb and Ta will be in the superconducting phase. In Ch. 4, I describe a device that utilizes the difference in the transition temperatures of the two elements in order to perform voltage-biased and phase-biased measurements on Nb Josephson junctions with the same atomic configurations. Effectively, the device is an rf-SQUID, which incorporates a Nb break junction as a Josephson weak link and has a part of the SQUID loop switchable between the normal and superconducting states. In such a system, a perfect contact must be achieved between the two superconductors, which required deposition of the thin Nb and Ta films on top of each other in the same deposition cycle without breaking the vacuum. Consequently, most of the standard additive and subtractive microfabrication techniques had to be adapted for this restriction. Operation principles and first tests of this composite device are described in detail in Ch. 4.

In Sec. 2.2, I describe the experimental setup used in all the experiments included in this thesis. Finally, in Sec. 2.3, I describe the calibration technique that allows one to relate the atomic-size contact or nanowire elongation with the displacement of a precision piezoelectric actuator.

2.1 Microfabrication Procedures

The microfabrication sequence is partially based on the thin-film MCBJ technology introduced by van Ruitenbeek *et al.* [95]. Most of the fabrication steps were done in Georgia

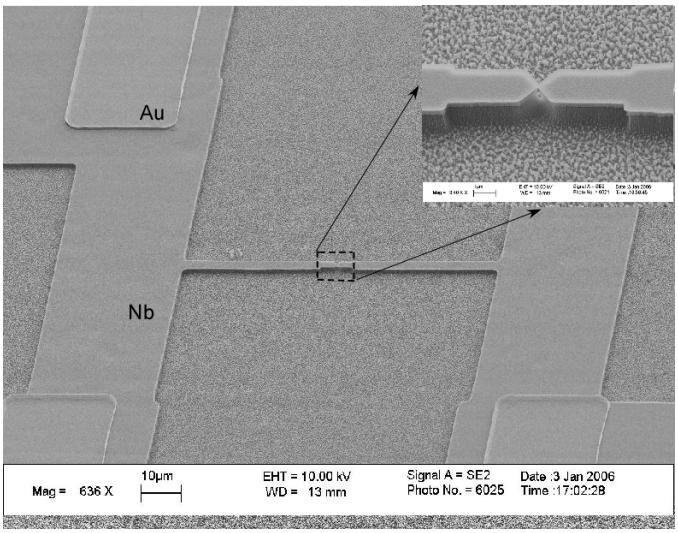

Figure 17: Scanning electron micrograph of microfabricated Nb MCBJ. The inset shows a zoom-in picture of the Nb bridge with a clear undercut in the insulating substrate, which is necessary for successful operation. Metal films (Au and Nb) are much smoother that the insulating polyimide layer.

Tech's Microelectronics Research Center (MiRC) cleanroom. The Oxford Energy Dispersive X-ray Spectroscopy (EDS) tool is available in the Center for Nanostructure Characterization and Fabrication in the School of Materials Science and Engineering. The electron-beam lithography tool is available in the School of Physics as a shared facility. Sputtering Nb and Ta thin films were done using our group's own cluster sputtering tool.

An SEM image of a typical Nb MCBJ is shown in Fig. 17. The inset shows a zoom-in picture of the Nb bridge with a clear undercut in the insulating substrate, which is necessary for successful operation. A top-view image of a typical Ta shunted Nb MCBJ and a zoom-in image of the Ta shunt are shown in Fig. 18.

2.1.1 Procedure Outline

The sequence of steps in the microfabrication procedure of Nb MCBJs is as follows (also, see Fig. 20):

1. Bronze plate preparation and deposition of the insulating layer (PI 2610 polyimide).

2. Nb deposition by sputtering.

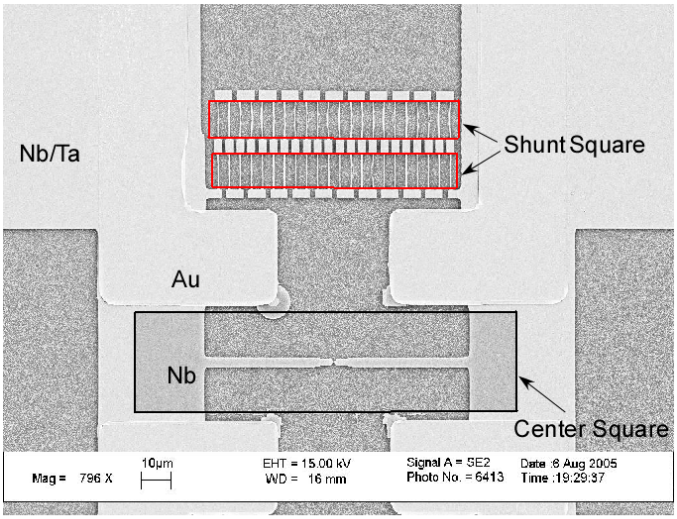

(a)

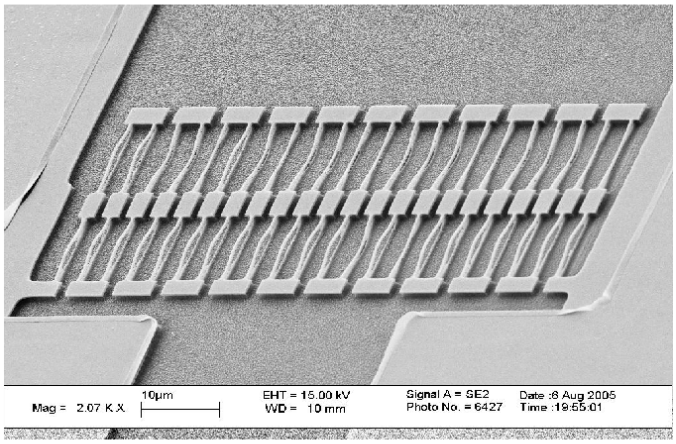

(b)

Figure 18: (a) Top-view SEM image of a Ta shunted Nb MCBJ. Both Nb and Ta are deposited in the same vacuum cycle to avoid an oxidation layer between them. In the "Center Square", the top Ta layer is removed by reactive ion etching (RIE in SF_6 plasma). In the "Shunt Squares", the underneath Nb layer is wet etched by a Nb etchant. Nb and Ta in other areas are removed by RIE. (b) SEM image of a tantalum shunt. Nb is removed from the thin wires spanning the rectangular pads. The shunt geometry shown in this panel produced resistances of up to 3 kΩ at liquid helium temperature (see Ch. 4).

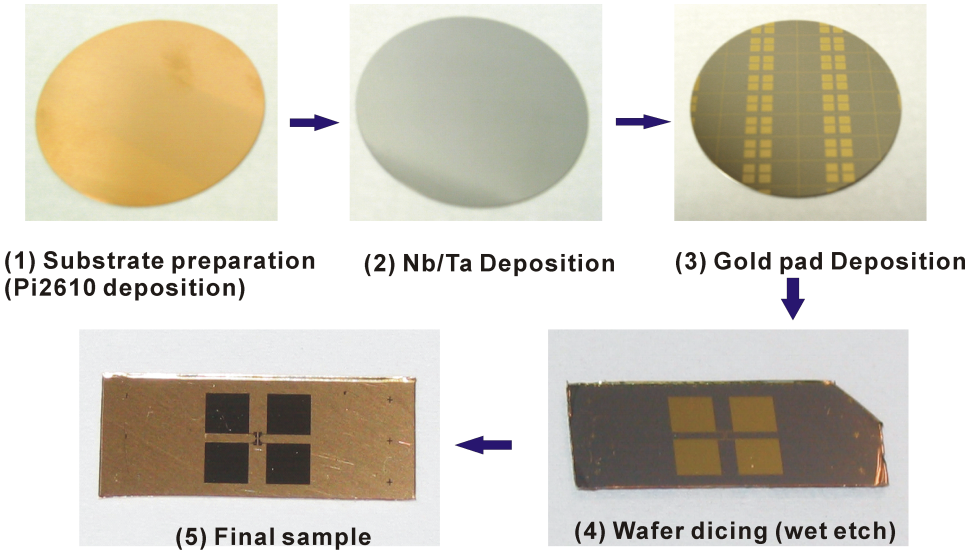

Figure 19: Outline of the microfabrication procedure of Nb MCBJ and Ta shunted Nb MCBJ: (1) Spin and cure a thin polyimide insulating layer on a bare bronze wafer. (2) Sputter Nb layer or a Nb/Ta bilayer. (3) Make Au contact pads and leads. The pads are patterned by photolithography. (4) Dice the wafer: pattern the backside of the bronze wafer by photolithography and wet etch in $FeCl_3$ solution to make sample chips. (5) Pattern Nb MCBJs or composite Nb/Ta devices on individual chips by e-beam lithography, perform dry and wet etching operations to obtain the desired samples.

3. Manufacturing gold contact pads: photolithography, metal deposition and liftoff.

4. Wafer dicing: photolithography and metal wet etching.

5. Pattern the MCBJ by e-beam lithography.

6. Deposit the dry etch aluminum mask.

7. Dry etch Nb.

8. Remove the aluminum dry etch mask by wet etching.

9. Dry etch the polyimide to create undercut.

The first 4 steps in the fabrication process are shown as (1) to (4) in Fig. 19. The remaining steps are shown in Fig. 20. The microfabrication procedure for Ta shunted Nb MCBJs contains steps from the Nb MCBJs procedure, but it is substantially more elaborate:

1. Bronze plate preparation and deposition of the insulating layer (PI 2610 polyimide).

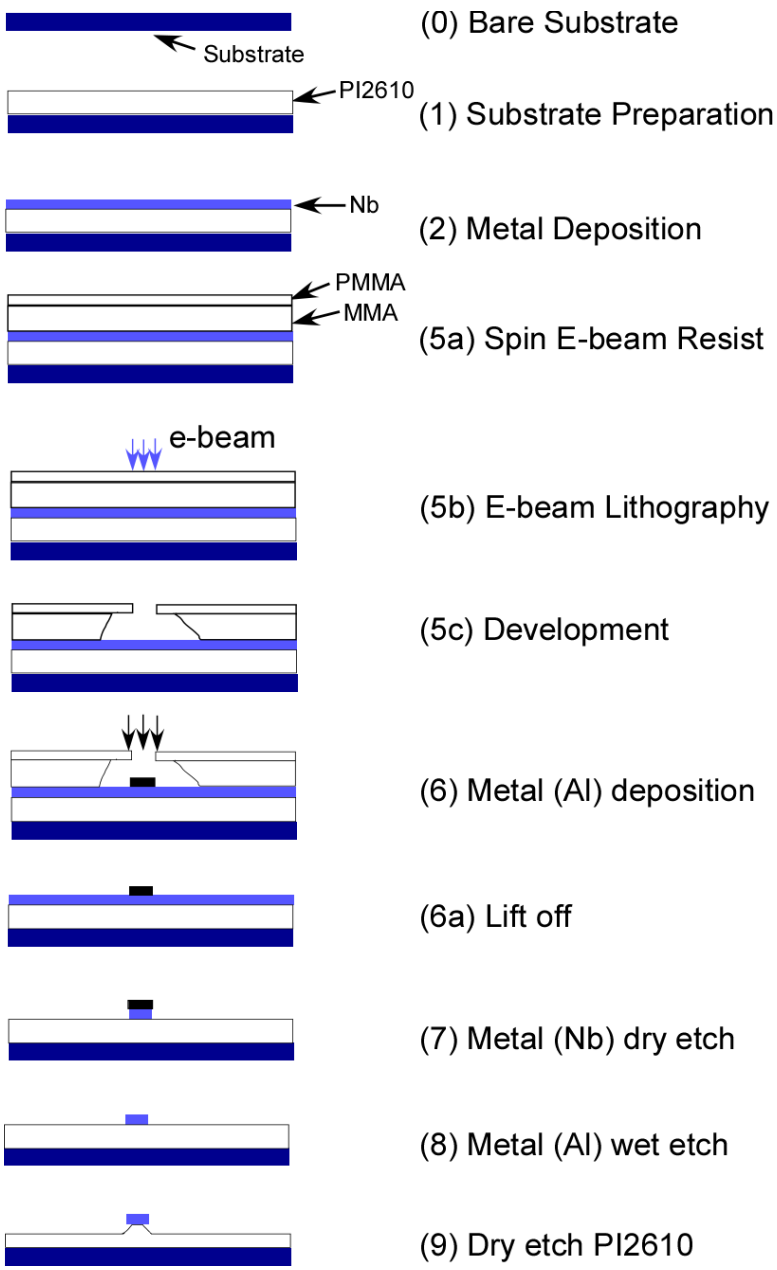

Figure 20: Sequence of microfabrication processes for producing Nb patterns. Patterns n top of the e-beam resist are drawn by an e-beam lithographer. Subsequently, a 20 nm Al film is deposited as a dry etch mask. The Nb layer which is not cover by Al is dry etched away by RIE. The Al mask then removed by wet etching in Al etchant. The final step involves dry etching of ~ 1 μm layer of the PI 2610 photoresist.

2. Nb/Ta bilayer deposition by sputtering.

3. Manufacturing gold contact pads: photolithography, metal deposition, and liftoff.

4. Wafer dicing: photolithography and metal wet etching.

5. Using e-beam lithography, open a window in MMA/PMMA (black rectangle in Fig. 18) in the junction area.

6. Remove all Ta in the window by RIE, monitor the process by Energy Dispersive X-ray Spectroscopy (EDS).

7. Pattern the MCBJ by e-beam lithography.

8. Deposit the dry etch aluminum mask.

9. Dry etch Nb.

10. Remove the aluminum dry etch mask by wet etching.

11. Using e-beam lithography, open a window in MMA/PMMA (red rectangles in Fig. 18 in the shunt area.

12. Dry etch 0.5 μm of PI 2610 to create the undercut.

13. Wet etch Nb.

14. Remove all the e-beam resist.

15. Dry etch 1 μm PI 2610 to create the undercut.

2.1.2 Substrate Preparation

The flexible substrates for MCBJs are made from phosphorus bronze wafers (Cu94/Sn6) supplied by Goodfellow, Inc. We use 0.25 mm thick 50 mm diameter wafers. These bronze wafers are smooth enough enough and do not require further mechanical polishing. The procedure for preparing the insulating substrate is as follows:

1. Spin VM 652 (primer) on the bronze wafer at 2000 rpm for 30 seconds.

2. Softbake at 110^{o}C for 1 minute on a hotplate.

3. Spin PI 2610 (polyimide) at 2000 rpm for 45 seconds.

4. Softbake at 90^{o}C for 2 minutes and at 150^{o}C for another 2 minutes .

5. Anneal in a nitrogen environment (Lindberg furnace) for 3 hours at 350^{o}C.

Both VM 652 and PI 2610 were purchased from HD Microsystems. The VM 652 is a primer layer which makes PI 2610 stick well on the phosphor bronze wafer. The PI 2610 layer serves three purposes: (a) to further smooth out the bronze wafer surface; (b) to act as an insulting layer between the flexible substrate and the metallic device; (c) to be etched to form an undercut. After the PI 2610 layer is fully cured, the substrate is ready for metals deposition.

2.1.3 Metals Deposition

In the device fabrication process, an AJA cluster DC/RF sputter is used to deposit both Nb and Ta. Because of their high melting temperatures (2750 K for Nb and 3290 K for Ta), it is difficult to deposit Nb or Ta by evaporation. Therefore, both Nb and Ta thin films were deposited by sputtering. Ultra-high purity Ar gas (99.9999% purity) was used for creating the plasma. Inside the sputtering chamber, we designed and installed a liquid nitrogen-cooled screen ring surrounding the sample holder. The cold trap is used to remove water vapor and other impurity gases during the metal deposition [38]. The trap must be cooled before starting the deposition during the time of the sample cooling. Without the trap, we were unable to produce superconducting thin-film samples; moreover, the tendency in Nb was to substantially increase the resistance upon cooling to liquid helium temperatures.

The superconducting temperature, T_c, of our Nb films is always in the range between 8.3 K and 8.9 K. The T_c of our Ta films is around 4.2 K (Ch. 4), which is somewhat lower that corresponding bulk critical temperatures (e.g. 9.3 K for Nb). This is the result of our inability to heat the polyimide substrate during the metal deposition process as required for producing highest quality Nb thin films with T_c near the bulk value [73].

Typically we deposit a 100 nm thick Nb layer on top of PI 2610 and the same thickness Ta layer on top of Nb, if required. Before either Nb or Ta deposition, we pump the sputtering chamber to below 3×10^{-6} mbar with a turbo pump. After the pump-down, liquid nitrogen is allowed to cool the cold screen. Due to the cryosorption effect, the chamber pressure drops down to $\sim 3 \times 10^{-7}$ mbar. Then we throttle the pumping line and let argon into the chamber; the desired dc plasma pressure is 7×10^{-3} mbar. After igniting the plasma, we keep the DC power supply at 30 W during the deposition, which results in the deposition rate of ~ 6 nm/min. To make Ta shunted Nb MCBJ, a 100 nm thick Ta layer is deposited on top of the Nb film in the same vacuum cycle. It is important to know that Ta thin films have two different crystallographic phases, α-Ta and β-Ta. α-Ta has body-centered-cubic crystal structure and β-Ta has tetragonal crystal structure [25]. α-Ta's superconducting transition temperature is 4.4 K and its resistivity is about 13.6 $\mu\Omega$ cm. β-Ta has tetragonal structure. Its superconducting transition temperature is 0.5 K, which is far below the bulk superconducting transition temperature. Its resistivity is 150 $\mu\Omega$ cm, which is much larger than the resistivity of α-Ta. When Ta is grown on Si, SiO_2 or polyimide etc., we will have β-Ta. When Ta is grown on Al (111), Nb, Cr etc., α-Ta can be obtained. This is the major reason why Ta is deposited on top of Nb and not the other way around.

The CVC e-beam evaporator in the MiRC cleanroom was used to deposit Al, Ti and Au. The chamber pressure during the deposition is kept around 2×10^{-6} torr. To make contact pads, a 15 nm thick Ti layer and a 185 nm thick Au layer are deposited on top of each other in the same vacuum cycle. Nb and Ta dry etch masks are formed by 20 nm thick Al layers.

2.1.4 Photolithography

Photolithography is used at two distinct stages in the device fabrication procedure. Firstly, photolithography is used to define the gold contact pads and leads. Secondly, it is used to pattern the backside of the bronze wafer for etching and dicing. The following steps are necessary in the contact pads fabrication:

1. Spin 1813 photoresist (Shipley Corp.) at 500 rpm for 5 seconds and 3000 rpm for

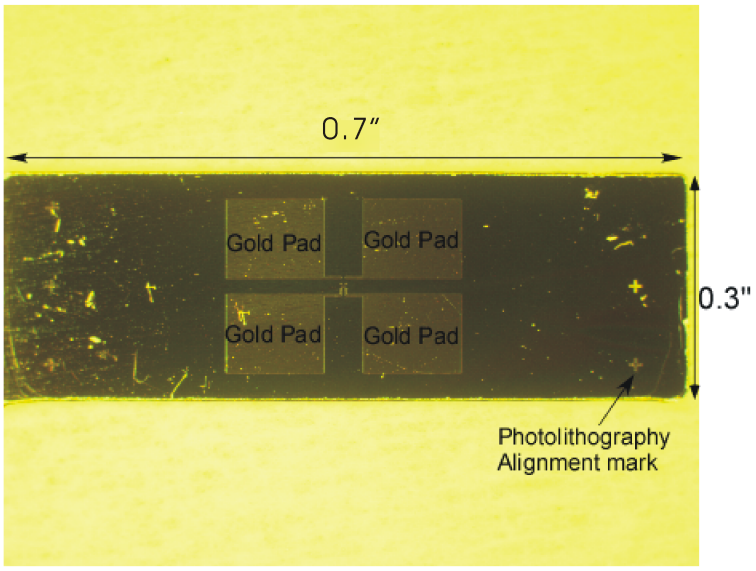

Figure 21: A bronze sample chip after the bronze wafer is wet etched from the backside in $FeCl_3$ solution and cut by surgeon knife.

45 seconds.

2. Softbake at 115^{o}C for 2 minutes.

3. Apply the mask and expose in a mask aligner (we used Karl Suss MA-6).

4. Soak in chlorobenzene for 15 minutes.

5. Develop in Shipley 354 developer solution for 45 seconds.

6. Deposit 15 nm of Ti and 135 nm of Au using e-beam evaporator.

7. Lift-off: soak in Shipley 1165 photoresist stripper at 70^{o}C for 2 hours.

The purpose of soaking the wafer in chlorobenzene is to harden the surface of the photoresist. This step is necessary for creating an undercut in the photoresist profile after developing, which makes the following liftoff process much easier.

To define the pattern for wet etching, steps 4, 6 and 7 are skipped. The development time in Shipley 354 is 25 seconds. After developing, hard baking (90^{o}C for 10 minutes on a hotplate) will help hardening the photoresist.

2.1.5 Wafer dicing and metals wet etching

After the backside of the bronze wafer is patterned by photolithography for dicing, the wafer is soaked in $FeCl_3$ solution (1:1 in water) at 70^oC for about 8 hours. When tear lines on bronze wafer are almost etched through, the wafer can be cut into 0.7" $\times$ 0.3" pieces with a surgical knife. One of the sample chips is shown in Fig. 21. The remaining photoresist is removed by soaking chips into Shipley 1165 photoresist stripper for 30 minutes at 70^oC. Then E-beam resist is spinned on them for E-beam lithography.

The aluminum dry etch mask can be etched by aluminum etchant (19 H_3PO_4 : 1 HAc : 1 HNO_3 : 2 H_2O) at 50^oC; the resulting etching rate is 4 nm/s. Nb etchant was purchased from Transene Company; Nb etching rate is about 3 nm/s. The etch rate for Ta in the Nb etchant is negligible. Good selectivity of Nb etchant between Nb and Ta makes it possible to etch the Nb layer beneath the Ta layer and form Ta wires in the shunt.

2.1.6 Electron-beam lithography

The photolithography tools in the MiRC cleanroom can only be used to define patterns whose minimum features are larger than 3 μm. For smaller features, such as the the break junction area and the shunt area, e-beam lithography is needed. The e-beam lithography tool in our possession is a converted JEOL 5910 Scanning Electron Microscope equipped with Nano Pattern Generation System (NPGS) from JC Nabity Lithography Systems. The minimum feature size which can be written by this tool is about 40 nm with the accelerating voltage of 25 kV. In essence, using e-beam lithography, we create aluminum contact masks for dry etching of the metals not covered by those masks, and open rectangular areas for creating MCBJs and shunts. To remove the e-beam lithography resist, the samples are soaked in acetone for 5 minutes. The MMA (methylmethacrylate) layer is more sensitive than the PMMA (polymethylmethacrylate) layer to the electron beam. Using MMA/PMMA creates an undercut which make the liftoff much easier (see Fig. 20). The following recipe was developed:

1. Spin MMA (6% in Ethyl Lactate) at 500 rpm for 5 seconds and then at 2250 rpm for 45 seconds.

2. Softbake at 150^{o}C for 90 seconds.

3. Spin 950K PMMA (2% in Anisole) at 500 rpm for 5 seconds and then at 2250 rpm for 45 seconds.

4. Softbake at 180^{o}C for 90 seconds.

5. Write the pattern in the bi-layer by the e-beam lithography tool.

6. Develop in 1:3 MIBK:IPA solution (MicroChem Corp.) for 45 seconds.

7. Rinse in IPA for 20 seconds.

8. Deposit (by evaporation) a 20 nm thick Al film.

9. Lift-off: soak in acetone for 20 minutes.

2.1.7 Reactive Ion Etching

The dry etching tool we used is a Plasma-Therm RIE (700 series) available in the MiRC cleanroom. It is used to etch Nb, Ta and PI 2610 polyimide. Pure SF_6 gas (pressure: 30 mTorr, power: 100 W, flow: 25 standard cubic centimeters per minute, sccm) is used to etch both Nb and Ta. The resulting etching rate is about 70 nm/min. To etch PI 2610, we used pure oxygen plasma (pressure: 200 mTorr, power: 250 W, flow: 40 sccm). The resulting etching rate is about 500 nm/min. Since this RIE is a shared tool, a 30 minute oxygen plasma cleaning process must be run before our etching processes to avoid polymer redeposition.

When etching Ta in the break junction area, the sample must be analyzed for Ta presence during after etching is finished. Too long etching will result in removing of Nb from the junction area, which is undesirable. Multiple etching/energy dispersive X-ray scans might be necessary to insure that Ta is completely removed. Typically, after the EDS spectrum shows less than 3% of Ta, we dry etch for 10 seconds to finish the procedure. Two EDS spectra are shown in Fig. 22.

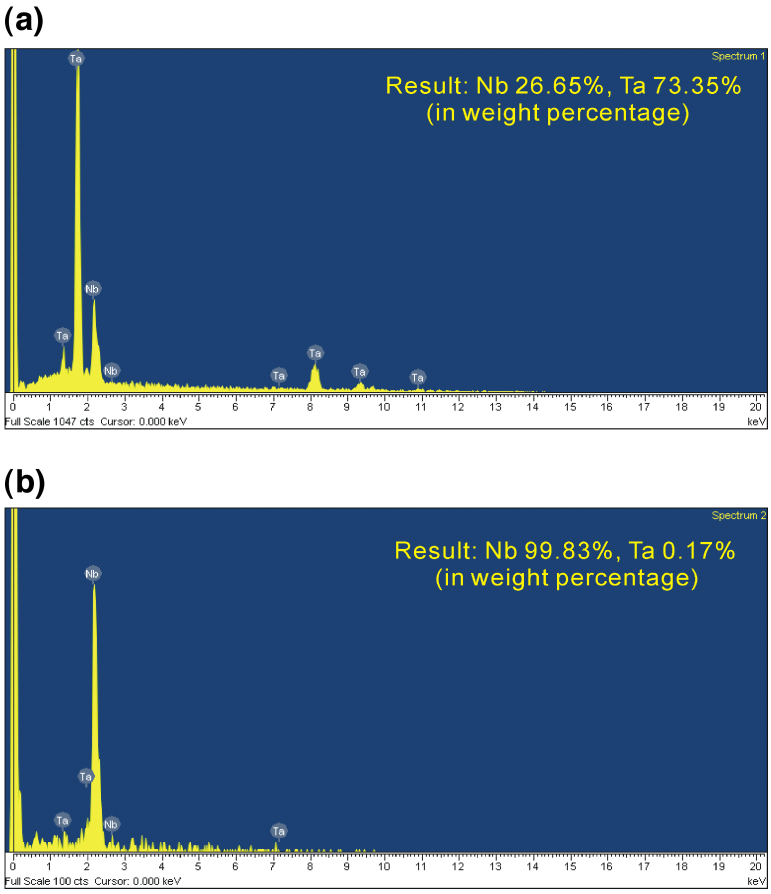

Figure 22: Energy Dispersive X-ray Spectroscopy (EDS) analysis of the efficiency result of Ta dry etching process in the break junction area. Panel (a) shows high concentration of Ta in the early stages of the process. Panel (b) shows that Ta is practically removed. For EDS analysis, etching must be interrupted and the sample transfered to the spectroscopy tool.

2.2 Experimental Setup

Both the Nb MCBJs experiments and the Ta shunted Nb MCBJ experiments were done in a custom-built dip-stick refrigerator shown in Fig. 23. The top manifold (Fig. 23(b)), which contains all the electrical, measurement, and mechanical feedthroughs as well as the evacuation ports, is assembled from ultra-high vacuum (UHV) rated Conflat (CF) components with OFE copper gaskets. This sample chamber of this cryostat can be pumped down to 10^{-7} torr at room temperature. This high vacuum combined with low temperatures is necessary to make sure the contact area of freshly broken Nb junctions is free of contamination. After evacuation, the dipstick is pre-cooled in a separate liquid nitrogen

dewar down to 77 K and inserted into a liquid helium-grade super-insulated nitrogen-free dewar (model PVS-4.0/54) manufactured by Precision Cryogenic Systems (Fig. 23(c) and (d)). The sample can be cooled down to $\sim$ 1.5 K by pumping on the liquid helium bath. Measurements are done in a Lindgren copper RF shielded room equipped with filtered AC power lines.

Fig. 23(a) shows the sample holder and manipulation system. We use a two-stage actuator system, which includes a micrometric screw for coarse adjustment and a piezoelectric actuator for fine adjustment (also see Fig. 24). The sample holder is thermally connected to the liquid helium bath through a thin copper wire, which allows manipulating the sample temperature between 1.5 and 40 K without a substantial additional helium consumption. The temperature of samples is measured by a Lakeshore Cernox-1010 thin film resistance thermometer. The sensor is glued to the copper sample holder by Stycast 2850; the resistance is measured by a Lakeshore 370 AC resistance bridge using the four point measurement scheme. On the sample holder, we also have a 150 Ω thin metal film resistor used as a heater.

2.2.1 Bending System

A picture of the real bending system is shown in Fig. 23(a). Its schematic is shown in Fig. 24. Inside the vacuum chamber, the sample can be coarsely adjusted by the 1/2" $\times$ 40 custom made micro-screw. The screw is made of brass and the nut is made of stainless steel to insure that the screw actuator does not jam after cooling to cryogenic temperatures. For the same reason, it is also extremely important to insure that the actuator is dehumidified (we usually pump on the vacuum chamber for at least 12 hours before cooling). The piezotube, which is made by Staveley Sensors, is used to precisely control the sample bending. The bias voltage for the piezotube is supplied by a Kepco bipolar operational power supplier/amplifier (BOP 500M). Its voltage output ranges from -500 V to 500 V. The piezo tube is 1" long, 0.25" diameter with 0.02" wall thickness. Macor ceramic pieces, which are glued on both ends of the piezo tube by Stycast 2850, are serve as electric insulators between the piezo actuator and the other components of the bending system. Staveley actuators are rated for cryogenic

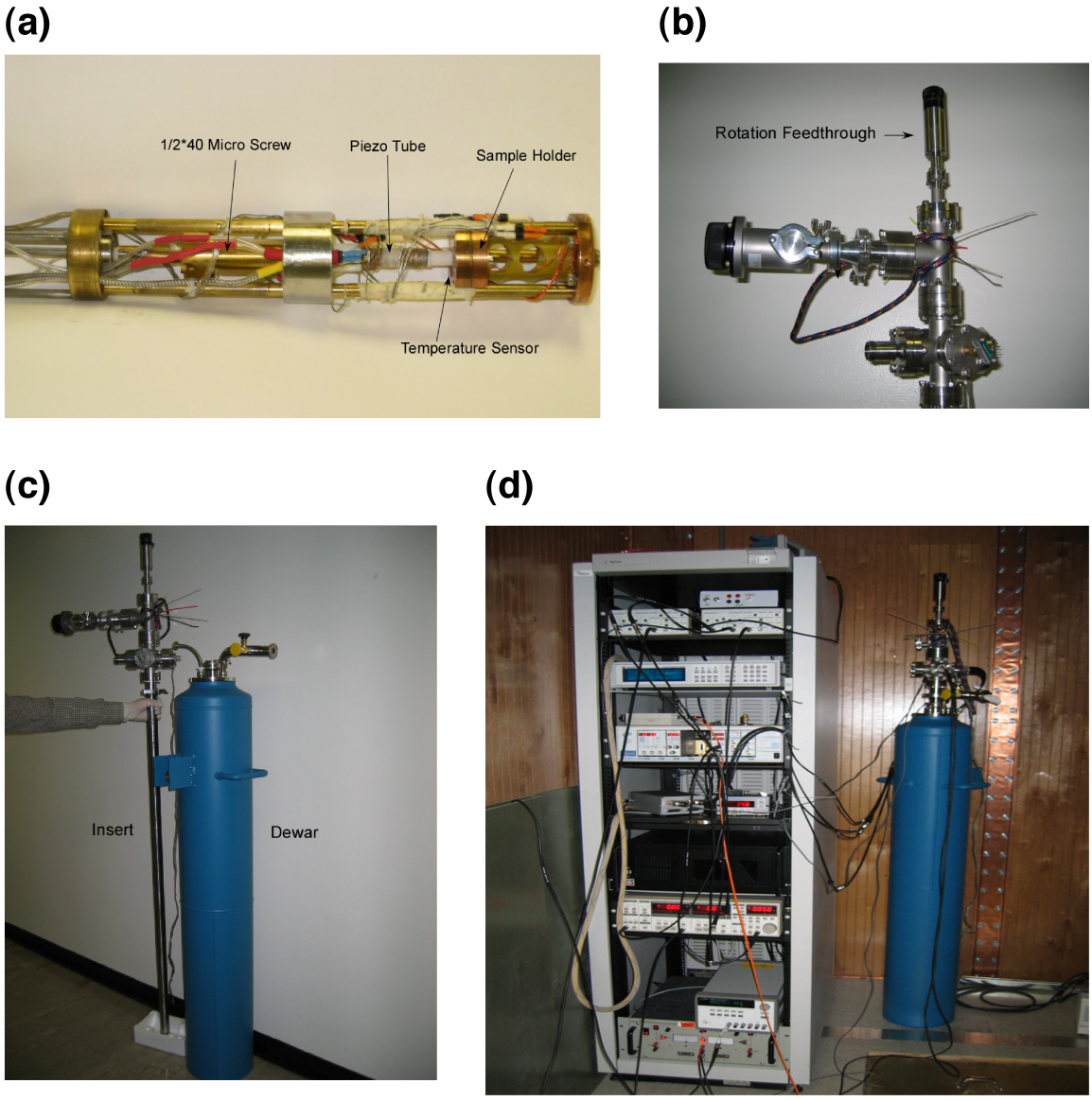

Figure 23: (a) A picture of the bending system. The coarse bending mechanism is a 1/2" × 40 custom-made micro-screw and the fine bending mechanism is a piezotube suitable for operation in cryogenic conditions. (b) The top manifold showing electrical, mechanical, and vacuum feedthroughs made of UHV rated CF components sealed with OFE copper gaskets. (c) Assembled dipstick refrigerator and liquid helium dewar. (d) Picture of experiment in progress. From top to the bottom of the rack, there are: SR 560 low noise preamplifiers, Lakeshore 370 AC resistance bridge, SIM 983 scaling amplifiers, liquid helium level meter controller, SR 830 lock-in amplifier, Agilent E3631A voltage supply, and Kepco BOP500M power supply.

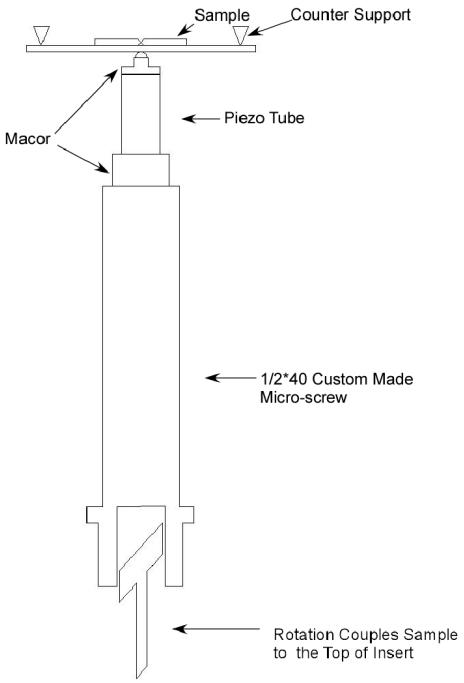

Figure 24: Schematic of the bending system. A rigid design is extremely important in producing high-stability atomic-size contacts and nanowires.

operation. Its elongation can be estimated from the relation provided by the manufacturer:

$$\Delta L = \frac{|d_{31}|L}{t} \times V = \frac{0.031 \times 1}{0.02} nm \times V = 1.55 \times V \ nm, \tag{14}$$

where V is the voltage bias on the piezo tube, L is the tube length, t is the wall thickness, d_{31} is -0.031 nm/V is the elongation constant at 4.2 K for PZT-5A ceramic. Hence, we can expect ~ 1250 nm elongation for the voltage range from -400 V to $+400$ V.

2.2.2 Measurement Circuits

The schematic of the measurement circuit is shown in Fig. 25. The preamplifiers are Stanford Research Systems SR560 with selectable gain. The lock-in amplifier is a Stanford Research Systems SR830. The data is collected by a National Instruments data acquisition board. This circuit allows measuring IV and dI/dV versus V curves simultaneously. In this circuit, the sample bias resistor, R_b, must be much larger than the resistance of MCBJ. Consequently, we can assume that:

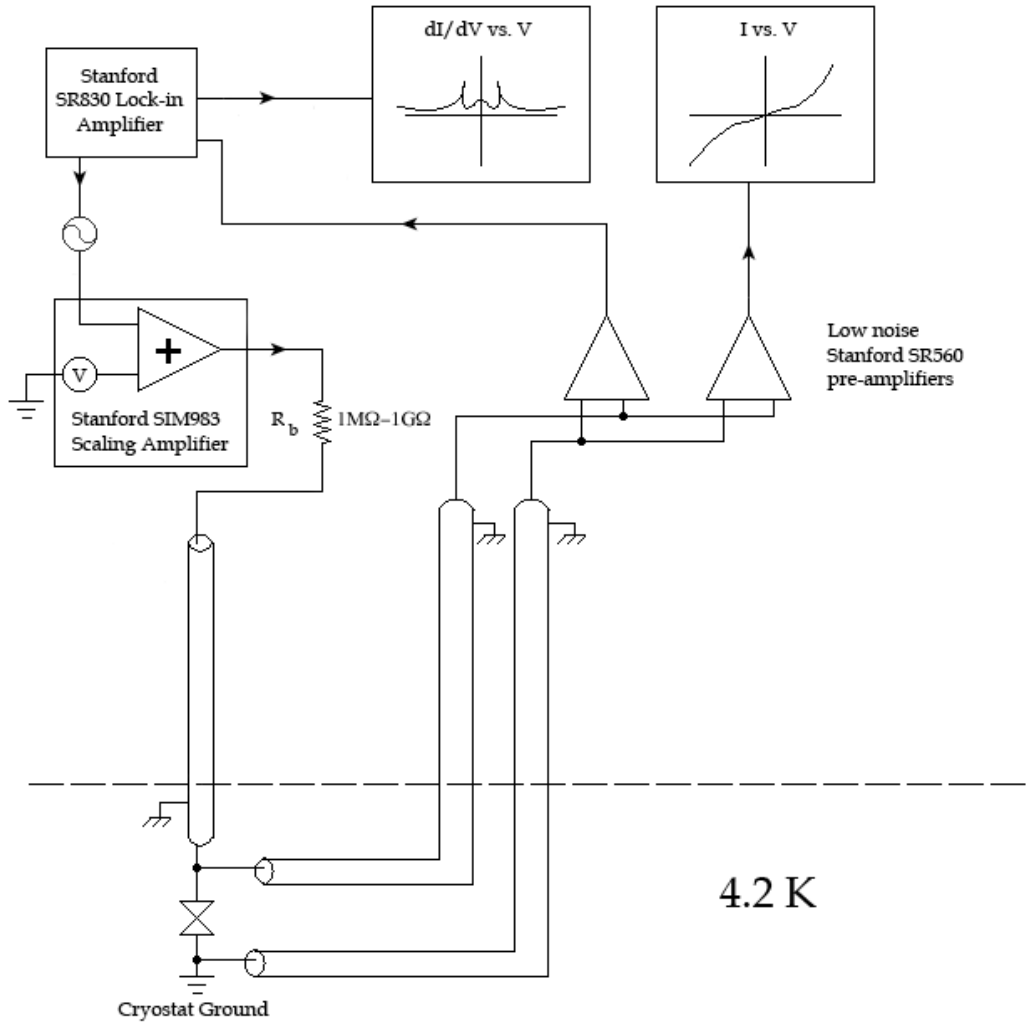

Figure 25: The measurement circuit for IV and dI/dV versus voltage measurements. The dc bias is provided by a low frequency (~ 0.005 Hz) triangular wave generated by a SRS DS 345 function generator. The low-amplitude ac bias is generated by the Stanford Research Systems SR830 lock-in amplifier, which is used in the dI/dV measurements. Both signals are added in a SRS SIM963 scaling amplifier and are fed to the sample through a resistor, whose value is much larger than that of the sample. Therefore, our samples are effectively current-biased. The voltage across the sample is amplified and filtered by two battery operated SRS SR560 preamplifiers, one in the dc mode for IV measurements and the other in the ac mode for the conductance measurements. All the measurement leads are made of ~ 2 meters cuts of Thermocoax high-resistivity semi-rigid coaxial cables, which are very efficient cryogenic RF filters.

$$|I_{AC}| = \frac{|V_{AC}|}{R_{MCBJ} + R_b} \approx \frac{|V_{AC}|}{R_b} \tag{15}$$

For typical $R_{MCBJ} \leq 10$ kΩ, we use $R_b = 1$ MΩ, and $R_b = 10$ MΩ higher junction resistances (tunnel contacts). Hence, the dc, I_{dc} and the ac, $I_{ac} \equiv dI$ can be calculated by dividing the bias voltages, V_{dc} and $V_{ac} \equiv dV$, respectively, by R_b. The output of the lock-in amplifier, $V_{lock-in}$, is proportional to the amplitude of the ac voltage drop across the junction, dI_{MCBJ}; therefore, the junction conductance is:

$$(\frac{dI}{dV})_{MCBJ} \propto \frac{I_{ac}}{V_{lock-in}} \tag{16}$$

2.3 Calibration of Sample Elongation

In high precision experiments, it is extremely important to have a precise measurement of the change in the distance between the contacts attached to an atomic-scale conductor, a molecule, or a nanowire. There are three basic methods which can be used to estimate such an elongation. The first method is based on calculating the displacement reduction ratio from the known geometry of the contact area. The product of the displacement reduction ratio and the piezo tube expansion gives the elongation. The second method is based on measurements of the tunnel resistance as a junction of the actuator displacement. In this case, the junction resistance depends exponentially on the distance between the two electrodes. The third method is base on field emission resonance [45], which will not be described here.

The relation for the displacement reduction ratio was introduced in Ch. 1:

$$K = \frac{\delta}{\Delta} = \frac{4tu}{L^2} \tag{17}$$

For our samples (see Fig. 5), we estimate $L = 1.5$ cm, $t = 0.25$ mm, $u = 2$ μm, giving the displacement reduction ratio of 2.7×10^{-5}. The manufacturer's specification for the piezo actuator at 4.2 K gives (Eq. 14) $\delta u = 1.55$ nm/V. Therefore, the estimated elongation rate is:

$$k = \frac{\Delta L}{V} \times K = 1.55 \times 2.67 \times 10^{-5} \text{ nm/V} = 4.14 \times 10^{-5} \text{ nm/V} \tag{18}$$

However, for microfabricated MCBJs this method turns out to be very unprecise, mostly due to the uncertainties in the thickness t and the separation of the anchoring points u. Therefore, it should only be used for order-of-magnitude estimates. A better method utilizes measuring the MCBJ tunneling exponent, where the resistance dependence on the separation between the tunneling points is given by:

$$R \propto exp[\frac{2}{\hbar}\sqrt{2m\phi} \times \delta], \tag{19}$$

where δ is related to the piezo actuator voltage, V, through the sample stretch rate k as: $\delta = kV$, and ϕ is the material's work function. Therefore, defining

$$\alpha \equiv \frac{\partial ln(R)}{\partial V} = \frac{2}{\hbar}\sqrt{2m\phi} \times k \tag{20}$$

yields

$$k = \frac{\hbar}{2\sqrt{2m}}\frac{\alpha}{\sqrt{\phi}} \approx 0.97\frac{\alpha}{\sqrt{\phi_{eV}}}, \tag{21}$$

where ϕ_{eV} is the material's work function in electron-volts. An example of such a calibration is shown in Fig. 26. The linear fit of $ln(R)$ versus the piezo voltage gives $\alpha = 0.0042$. Since the work function for Nb is 4.3 eV, this sample's stretch rate is:

$$k = 0.97\frac{0.0042}{\sqrt{4.3}} \text{ Å/V} = 1.96 \times 10^{-4} \text{ nm/V}. \tag{22}$$

Nonetheless, the relative inaccuracy of this method can exceed 30% primarily because of the assumption that the work function is equal to clean and smooth surface value. In our atomic-scale samples, characterized but extremely high curvature radii, the work function value is most likely larger, hence Eq. (21) most likely overestimates the sample elongation. Despite this drawback, this is the method which we used in our experiments where the elongation is an important experimental parameter.

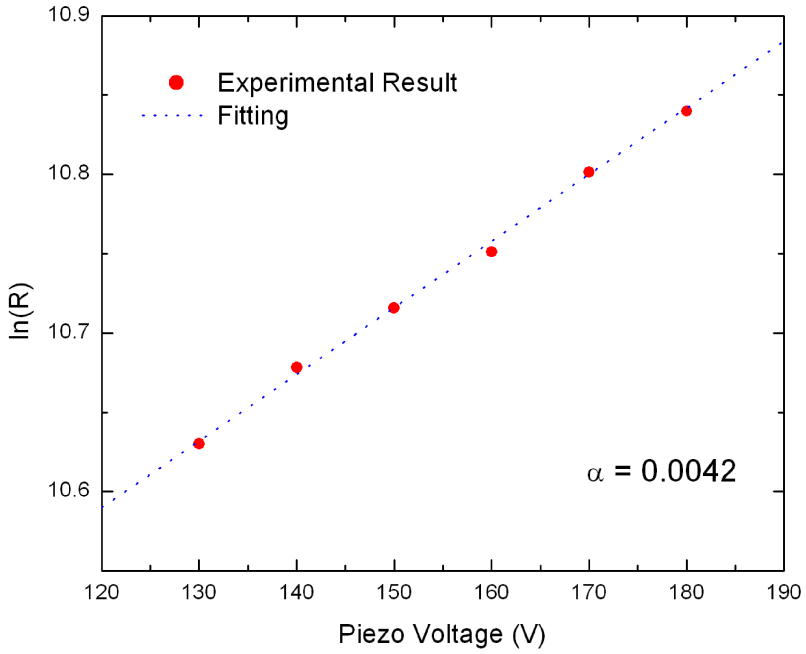

Figure 26: Resistance of a Nb MCBJ in tunnel mode versus the piezo actuator voltage. Red dots are the experimental points and the dotted line is the fitting. From the slope α, the MCBJ elongation ratio can be determined.

CHAPTER III

STRUCTURE AND TRANSPORT PROPERTIES OF NIOBIUM ATOMIC-SIZE CONTACTS AND WIRES

In this chapter, I report on high-resolution conductance measurements in niobium nanowires at the final stages before break-up, when the conductance is of the order of $2-5\ G_0$ with a few contributing channels. Experiments were performed on microfabricated mechanically-controlled break junctions (MCBJ) in a cryogenic setup that permits very high levels of stability and control over the elongation process. First, results for a closed multistage elongation-compression cycle of a nanoscale contact, starting with a relatively high conductance of $\sim 4.5G_0$, are shown and discussed. Then, the focus is shifted to a conductance bistability region (perpetually found around $2.5G_0$) which manifests itself as random telegraph noise. Analysis of data obtained during reversible manipulation of the contacts below [12, 82, 42, 40, 58, 18] and above the superconducting transition temperature, allowed determination of the conductance channel compositions at various stages of the elongation process, including a switching region where two-level RTN is observed. The use of density functional theory (DFT) electronic structure calculations [4], coupled with structural optimizations and evaluations of the electric conductance (using the non-equilibrium Greens function (NEGF) method [87, 11]) allowed us to determine that the nanowire (NW) structure underlying, and consistent with, the complete set of experimental observations, consists of a Nb dimer suspended between the two electrodes. The calculated conductance variations as a function of elongation, reversibility, patterns revealed in the channel composition, and two-level switching behavior between HG and LG states corresponding to symmetric and asymmetric positions of the dimer in the gap (with the latter one predominating for larger gap widths), faithfully reproduce the experimental observations.

This work was performed in collaboration with Dr. Chung Zhang, Dr. Robert N. Barnett, and Prof. Uzi Landman from the School of Physics at Georgia Tech, who have

performed the DFT/NEGF simulations. The results described in this chapter were submitted for publication to Physical Review Letters and as an invited keynote paper for the Proceedings of the International TNT2006 ("Trends in Nanotechnology") Conference held between Sept. 4 and Sept. 8, 2006, in Grenoble, France.

3.1 Previous Work

Formation of nanowires (NWs) suspended between an atomically sharp tip and a metallic crystal surface was discovered in 1990 by Landman *et al.* through molecular dynamics simulations [53] (see Fig. 4(a) and (b)), which were aimed at exploring contact formation, nanoindentation, the atomic origins of frictional processes, and tip-substrate interactions [53, 6, 54]. Experimental and theoretical studies of the structural, mechanical, electrical, and chemical properties of atomic-size contacts and nanowires continue to be an active research area [1, 70, 55, 76, 78, 63, 69, 67, 83, 84, 99]. These simulations have shown the formation of a nanowire junction at room temperature, during the course of an adiabatically slow separation of a nanocontact between a tip and a surface (nickel tip and gold surface in the original work [53]). Nanowires formed in this manner (or via adiabatic elongation of a contact in general, for example through the use of a mechanically controlled break junctions) were found in the simulations to exhibit highly ordered crystalline structures. These nanowires are predicted to possess nearly ideal mechanical properties (that is, enhanced critically resolved axial stresses that are much higher than those of the bulk metal [53, 55, 76]) reflecting the defect intolerance of nanoscale structures, their high annealing propensity resulting from a very large surface-to-volume ratio that is characteristic to nanoscale systems, and their dislocation-less mechanical deformation mechanisms.

The contact elongation process was found to proceed through a sequence of structural instabilities, each comprised of stress accumulation and yield stages (with the elongation process localized to the neck region of the junction). These structural evolution patterns have been shown through the simulations [53] to cause oscillations of the force required to elongate the wire, with a period approximately equal to the crystal interlayer spacing. The saw-tooth character of the predicted force oscillations reflects the stress accumulation and

relief stages of the elongation mechanism.

These predictions, as well as anticipated electronic conductance properties (that is, point contact characteristics and conductance quantization in units of the conductance quantum ($G_0 = 2e^2/h, G_0^{-1} = 12.9$ kΩ), have been corroborated in a number of experiments using scanning tunneling and force microscopy [70, 76, 1, 69, 67, 83, 84], break junctions [63, 1], and pin-plate techniques [55] at ambient environments, as well as under ultrahigh vacuum and/or cryogenic conditions. Particularly interesting are experimental (room temperature) observations [76] of the oscillatory behavior of the elongation forces and of direct correlations between the step-wise changes in the conductance and the force oscillations (portraying the predicted structural evolution) [99]. The conductance quantization in nanowires is in accord with the Landauer theory [51, 52, 39] where the total conductance is given by $G = G_0 \sum_{j=1}^{N} \tau_j$ with $\{\tau_j\} \equiv \{\tau_1, ..., \tau_N\}$ denoting the set of transmission coefficients of the N channels that contribute to the NW conductance at a given NW configuration. The channel composition $\{\tau_j\}$ can be deduced from low-voltage IV characteristics of atomic-size superconducting point contacts or NWs [12, 82, 42, 40, 80, 58, 18] (see Sec. 1.4.3).

One of the most fascinating aspects of nanowires is the prospect of formation of atomic-scale contacts and switches [53, 83, 56, 30, 23, 9, 88], which may occur towards the ultimate stages of elongation (that is before complete physical separation, or breaking, of the wire). Such atomically thin nanowires have indeed been observed in the aforementioned early simulations of gold nanowires [53]. More recently gold nanowires have been imaged by high-resolution transmission electron microscopy (HRTEM) as a gold STM tip was retracted from a gold surface [66], confirming the early theoretical predictions (see Fig. 4(c)). Moreover, gold dimers suspended in the gap between the tips of two opposing electrodes has been predicted through first-principles molecular dynamics simulations [34]; in this study it was shown that elongation leads eventually to breakup of the dimer with one of the atoms bonding to one of the electrodes and the second one adhering to the the other electrode. Formation of atomic gold chains comprised of several atoms has also been reported in break-junction experiments [101], and imaged via HRTEM as connecting bridges between areas in thin gold films perforated by impact of energetic electrons [66, 75].

Correlation between the structural and transport properties in NWs is spectacularly demonstrated by large-scale conductance fluctuations caused by atomic rearrangements. In particular, adjusting a contact precisely at conductance jumps between neighboring plateaus in a conductance versus elongation curve may lead to fluctuations between two discrete values in the form of random telegraph noise (RTN), involving high and low conductance states (HG and LG, respectively), whose origin remains unknown [63, 93]. However, short of direct imaging of the NW structure during elongation and simultaneous measurement of the conductance [66], evidence for the aforementioned close correlation between the structural and transport characteristics is still lacking.

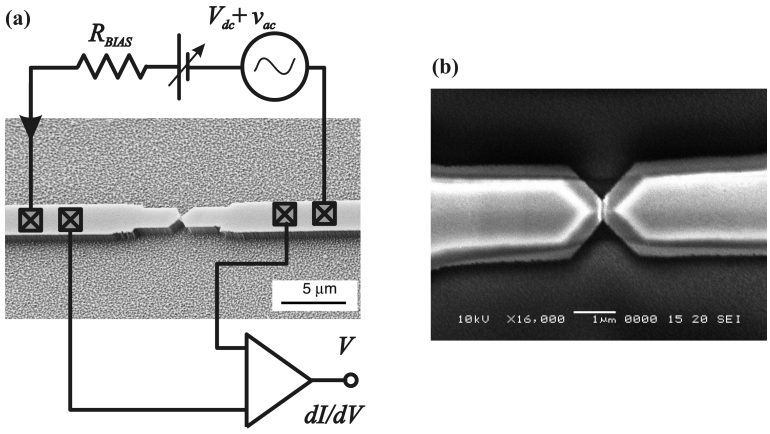

Figure 27: (a) Scanning electron micrograph of a niobium microfabricated mechanically controlled break junction. A diagram of the measurement setup is superimposed. (b) Magnified top view of one of the junctions taken after a breaking experiment. Unlike tensile materials, such as gold or aluminum, which show substantial plastic deformations in the contact region, our niobium samples appear to break along two microcrystalline facets. The horizontal bar at the middle bottom of panel (b) correspond to a length of 1 μm.

3.2 Methods

We used microfabricated samples in a cryogenic MCBJ set-up (see Fig. 27), prepared by dc-magnetron sputtering of Nb onto a 1 μm thick insulating polyimide layer covering a flexible bronze substrate (see Ch. 2). The film deposition was performed in the presence of a liquid-nitrogen shield to avoid deterioration of the superconducting properties of niobium by outgasing of water, polyimide and the organic photoresist (PMMA) mask. The width,

thickness, and length of the suspended constrictions were all $\sim$ 100 nm. The procedure was optimized for producing high superconducting transition temperatures, which tends to yield microcrystalline thin films [36]. SEM micrographs of samples previously used in our experiments indicate that breaking occurs by cleaving along the boundary between two microcrystallites (see Fig. 27(b)). Our MCBJ set-up yields remarkably stable contacts and allows reversible manipulation of the electronic structure of the contact within $\sim$ 1 Å elongation range. We could restore the length of the contact with an accuracy better than 1 pm and reproduce highly nonlinear IV and conductance (dI/dV) characteristics, even after more than 12 hours of experimentation involving several atomic configurations. All measurements reported here were performed in ultra-high vacuum conditions at 4.2 K and 9 K.

Insights into the nature of bonding, atomic arrangements, structural transitions and electronic transport in Nb nanowires formed upon the separation of the leads were obtained through density functional theory (DFT) electronic structure calculations [4] and conductance calculations with the combination of DFT and the non-equilibrium Green's function method (NEGF) [87, 11, 105]. The DFT calculations include the generalized gradient approximation, GGA [72], using a plane wave basis (kinetic energy cutoff $E_{cut} = 68$ Ry), and norm-conserving soft pseudopotentials [92]. In the pseudopotential construction we used as a reference configuration [Kr]$4s^2 4p^6 4d^5 5s^0$, i.e. 13 valence electrons per atoms as described in Ref. [32]. In this scheme the electronic configuration of the atom is given correctly to be [Kr]$4s^2 4p^6 4d^4 5s^1$. One of the key capabilities of the DFT/NEGF formalism is the capability of constructing the conductance eigenstates (independent conductance channels) starting from the plane wave basis as well as calculating the corresponding (energy-dependent) transmission coefficients (CCC) (see appendix A). This capability allows to scrutinize the match between the channel compositions obtained by microscopic modeling and derives from transport experiments.

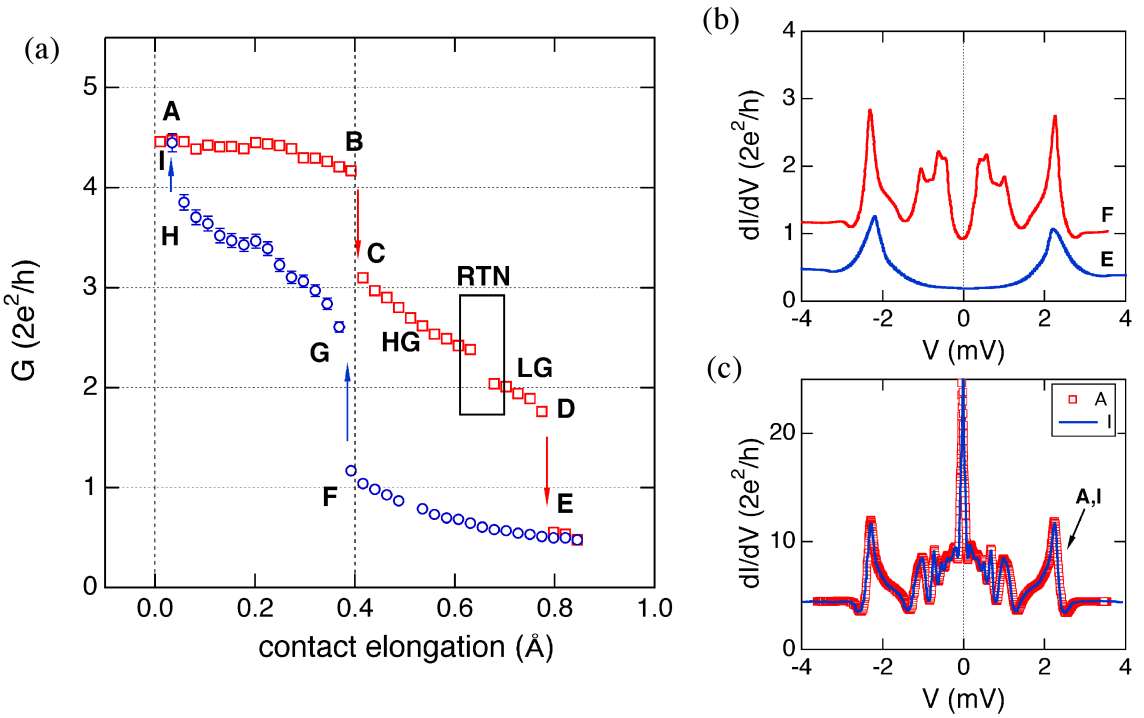

Figure 28: (a) Elongation-compression cycle of a Nb contact at 4.2 K. Squares (red online) represent stretching of the contact and formation of the nanowire; circles (blue online) correspond to compression. In this contact configuration, the initial conductance was $\sim 4.4G_0$. After elongating the nanowire by 0.4 Å (interval **AB**), a sudden jump occurred (**BC**), indicating switching of the contact into another configuration (interval **CD**). This interval contains a region of slow two-level random telegraph noise (**RTN**) flanked by high (**HG**) and low (**LG**) conductance branches. After elongating the NW by 0.8 Å from the initial configuration (point **D**), the contact switched abruptly into a tunnel junction (**E**), as evidenced by the exponential dependence of the conductance on the elongation during the nanowire compression (interval **EF**), as well as from the conductance spectra (dI/dV vs. V) shown in panel (b), where we display data corresponding to points **E** and **F** (see panel(a)). The compression of the tunnel junction culminates in a sudden jump to contact (**F** to **G**) at nearly the same electrode separation as the **B** to **C** step during the stretching. The resulting configuration was further compressed up to a conductance of $\sim 3.8G_0$ (**H**), where it abruptly switched into configuration **I**. This last configuration was found to be identical to the one at the beginning of the cycle (**A**). To demonstrate this finding we show in panel (c) the conductance spectra for configurations **A** and **I**. The total time interval between the measurements of the spectra at **A** and **I** was 12 hours.

3.3 Results

A full elongation-compression cycle of the nanowire contact that started at a configuration having a conductance of $\sim 4.4G_0$ is shown in Fig. 28. Upon elongation of the contact by 0.4 Å (interval **AB**), a sudden jump occurred (**BC**), indicating switching of the contact into another configuration (interval **CD**). This interval contains a region of slow two-level random telegraph noise (RTN) flanked by high (HG) and low (LG) conductance branches. For this particular contact realization, the difference in conductance between the HG and LG states in the RTN region was unusually small; the step sizes that we normally observe are $\sim 0.5G_0$ (see Fig. 29). Subsequent elongation of the NW by 0.8 Å from the initial configuration (point **D**) caused the contact to switch abruptly into a tunnel junction (**E**), as evidenced by the exponential dependence of the conductance on the elongation during the nanowire compression (interval **EF**), as well as from the conductance spectra (dI/dV vs. V) shown in panel (b), where we display data corresponding to points **E** and **F** (see panel(a)). Here we note low values of differential conductance at a vanishing bias voltage. The compression of the tunnel junction culminates in a sudden jump to contact (**F** to **G**), that occurred at nearly the same electrode separation as the **B** to **C** step during the stretching. The resulting configuration was further compressed up to a conductance of $\sim 3.8G_0$ (**H**), where it abruptly switched into configuration **I**. This last configuration was found to be identical to the one at the beginning of the cycle (**A**). To demonstrate this finding we show in panel (c) the conductance spectra for configurations **A** and **I**. The total time interval between the measurements of the spectra at **A** and **I** was 12 hours.

In what follows, we focus on investigations of the random telegraph noise region and the high and low conductance branches adjacent to it. For this purpose we display results corresponding to measurements with a larger difference between the HG and LG branches, i.e. $0.55G_0$, see Fig. 29(a). In this measurement we started by adjusting the contacts' conductance to just below $\sim 3G_0$ using a coarse screw actuator. This conductance corresponds to the most probable atomic configuration as can be judged from the conductance histogram obtained using notched-wire samples [58] (see Fig. 7). From this point, we used the fine piezo actuator. After adjusting the length, we measured the contact's current-voltage (IV)

and conductance (dI/dV) characteristics and determined the channel composition. Typical behavior seen in 18 contact realizations from 5 different samples is as follows: as the contact was stretched, the conductance gradually decreased to $2.4 \pm 0.15 G_0$ (Fig. 29(a)); subsequently, in an elongation range of ~ 0.1 Å we observed slow two-level fluctuations (with a conductance difference of up to $0.6 G_0$) between well defined HG and LG values, which showed characteristics of RTN (Fig. 29(d)-(f)); upon further elongation, the state with lower conductance was stabilized (Fig. 29(a)(e)). At any point, the direction of the contact length adjustment could be reversed and the conductance behavior reproduced without detectable hysteresis. Elongation beyond the range shown in Fig. 29(a) results in breakup of the contact.

The conductance evolution curve shown in Fig. 29(a) includes multiple traversing of the RTN region, where the conductance was obtained by time-averaging of the two-level fluctuations (Fig.29(d),(e)). This behavior was reproduced both in the superconducting state, where the conductance is determined from dI/dV on the resistive branch ($eV > 2\Delta$, where Δ is the superconducting gap), and in the normal state at temperatures above our devices' superconducting transition temperature of ~ 8.8 K. It has been previously shown that suppression of superconductivity in aluminum atomic-size contacts by either raising the temperature or applying a magnetic field does not affect their electronic structure seen through the channel composition [79]. We have experimentally verified the temperature independence of our results for both the HG and LG states (see Sec. 1.4.4 and 5.1.2). Differential conductance curves of the HG and LG configurations taken in the vicinity of the RTN region are shown in Fig. 29(b)-(c); the corresponding IV curves are shown in Fig. 29(f). The most noticeable difference is that there are two high-transparency ($\tau_j \geq 0.6$) channels in the HG state, while there is a single such channel in the LG state (see the inset in Fig. 29); for all experimental contact realizations it is the transparency of the latter channel that was higher than that of the highest-transparency channel of the HG state. This can be qualitatively seen from the higher conductance in the LG state near zero voltage bias (compare Figs. 29(b) and (c)).

Manipulation of the contact length in the RTN region allowed us to change the ratio of

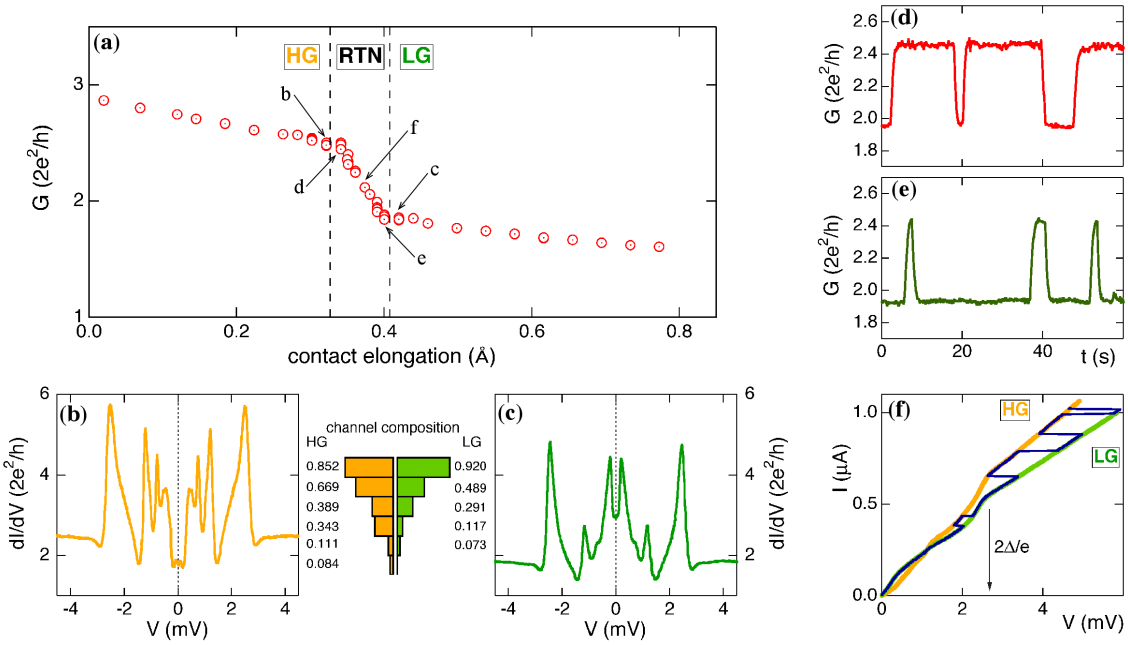

Figure 29: (a) Reversible variation of the conductance versus elongation distance recorded at 4.2 K. Similar results were obtained above the superconducting transition temperature. With further elongation the NW breaks. (b), (c) The differential conductance of the HG (b, yellow online) and the LG (c, green online) states versus voltage measured at 4.2 K. The measurements correspond to points b and c in panel (a). The corresponding channel compositions are shown in the inset between (b) and (c). (d), (e) Temporal conductance fluctuations near the HG and LG states, respectively, taken at points d and e in panel (a). The contacts were current-biased at $I_{bias} = 0.75$ μA. (f) Switching between the two states recorded while acquiring the IV characteristics in the middle of the RTN region (solid line, blue online). The curves marked HG and LG (yellow and green online) correspond to the dI/dV curves shown in (b) and (c). The acquisition of each curve in (f) takes about two minutes.

the time the NW spent in the two states (Fig. 29(d)-(f)), which is consistent with adjusting the two minima in the double-well potential describing the two-level fluctuating system [97, 35]. To summarize the experimental observations, we have measured the conductances and the channel compositions of the two states, separated by a narrow region of two-level fluctuations, where the time, which the contact spends in each of those states, can be continuously adjusted by stretching or compressing the nanowire. From the extremely slow rate of these fluctuations, we assumed that they are caused by the contact changing its atomic configuration, which, in turn, causes the change in the conductance. Since the conductance of the contact is small, we assumed that there are only a few atoms which are involved in these configurational transformations. In Fig. 30, I show cartoons of several thought-up possibilities of the structure of the smallest atomic contacts with two distinct configurations. In the DFT/NEGF simulations, these configurations (real crystal lattice structures are considered) are first relaxed, i.e., the atoms are allowed to move until they reach their equilibrium positions. DFT structural optimizations must confirm that the HG and LG configurations are energetically stable and can be of nearly equal energy with a relatively low barrier between them. This requirement comes from the experiment, where two states were observed with nearly the same average occupation time (Fig. 29(f)). Subsequently, the electronic structure, conductance and the channel composition calculations provide a definitive conclusion on the match of a given structure with the experiment.

We explored first the electronic and atomic structures of several atomic contacts and nanowire configurations spanning the gap between two opposing Nb electrodes of pyramidal shapes (Fig. 31). In structural optimizations all the Nb atoms included in the "contact region" (see Fig. 31(a)) are fully relaxed, while the other atoms (considered as part of the leads) are held in their bulk Nb lattice positions; we have found that changes in the distance between the electrodes express themselves essentially entirely in variations of distances in the gap region only. These relaxed local structures are subsequently used in the NEGF transport calculations which employ semi-infinite bcc (100) leads (consisting of bcc stacked alternating 4- and 5-atom layers) and the contact region (see Fig. 31(a)). In the NGEF calculations we used an atomic basis with the same 10 orbitals per atom as those used in

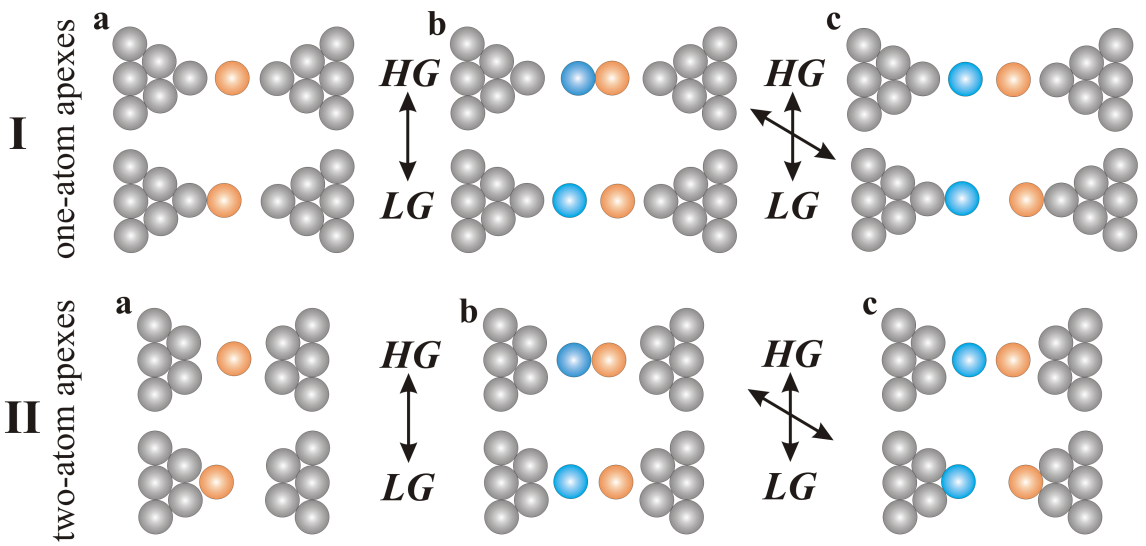

Figure 30: Cartoons of several thought-up possibilities of the structure of the smallest atomic contacts with two distinct configurations. In the DFT/NEGF simulations, these configurations are first relaxed, i.e. the atoms are allowed to move until they reach their equilibrium positions. DFT structural optimizations must confirm that the HG and LG configurations are energetically stable and can be of nearly equal energy with a relatively low barrier between them. This requirement comes from the experiment, where two states were observed with nearly the same average occupation time. Subsequently, the electronic structure, conductance and the channel composition calculations provide a definitive conclusion on the match of a given structure with the experiment.

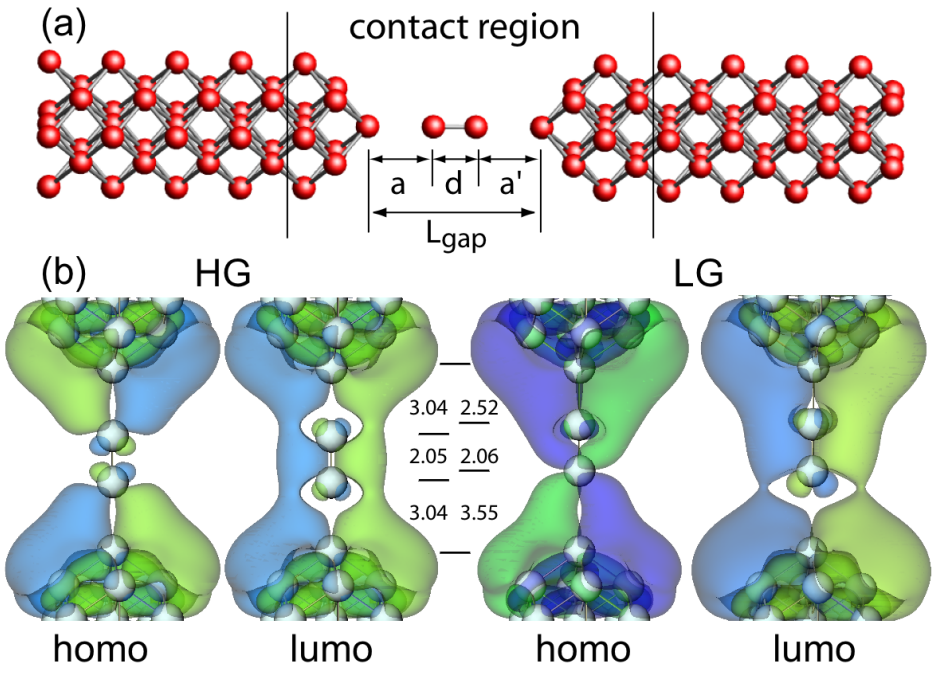

Figure 31: Nb nanowire configurations and wave functions. (a) The division of the system into the contact region and the two leads. A symmetric Nb dimer is shown in the gap (i.e. $a = a'$). (b) A symmetric high-conductance (HG) configuration (left) and an asymmetric low-conductance (LG) one, both corresponding to $L_{gap} = 8.13$ Å. For both we show superimposed on the atomic structure iso-surfaces of the highest (lowest) occupied (unoccupied) molecular orbitals, homo (lumo) respectively, with energies close to the Fermi level. The orbitals shown have large overlaps with the conductance eigen-channels. These Kohn-Sham wave functions are made predominantly of d-states and they extend over the Nb dimer and the leads. The two shades (blue and green online) correspond to positive and negative signs of the wavefunctions.

the construction of the pseudo potential, which are then expanded in a plane wave basis with $E_{cut} = 68$ Ry.

Several configuration that we have explored initially yielded results that do not correspond to the experimental findings: most importantly, they do not show two-level behavior upon stretching of the contact. These include: (i) the case of two electrodes sharing a common vertex atom as shown in Fig. 30(IIa) (separated by the bulk nearest-neighbor distance, $d_{nn} = 2.66$ Å from the nearest atom in the underlying layer) yielding a conductance of $\sim 5G_0$ [16], and (ii) a configuration where the two electrode tips are bridged by a single

suspended atom separated by d_{nn} from each of the tip atoms (Fig. 30(Ia)), with a conductance of $4.8G_0$. As we describe below, the only nanowire configuration whose transport and structural characteristics agree well with the measurements for the entire range of tip-to-tip gap distances, L_{gap}, discussed in this paper , consists of a dimer of Nb atoms suspended in the gap between the opposing Nb electrodes (Fig. 31).

We begin with a gap-width $L_{gap} = 7.6$ Å, where in equilibrium the two Nb nanowire atoms are separated by $d = 2.05$ Å, and their distances from the tip atoms $a = a' = 2.77$ Å. The calculated conductance for this configuration is $3.0G_0$, with a channel composition $\{0.92, 0.82, 0.48, 0.33, 0.24, 0.1\}$; we list only channels with $\tau_j \geq 0.1$. This correlates well with the highest measured conductance value shown in Fig. 29. As long as $L_{gap} < 8.0$ Å only a symmetric (i.e. $a = a'$, see Fig. 31(b) left) dimer configuration is found to be stable, with the conductance decreasing slowly and monotonically upon stretching of the contact. However, when $L_{gap} = 8.13$ Å two states of the suspended Nb dimer are found: the lower energy one corresponds to a symmetric dimer, and the higher energy (0.4 eV) metastable isomer is a displaced asymmetric dimer configuration (i.e. $a' > a$, see Fig. 31(b) right). The symmetric dimer structure with $d = 2.05$ Å, and $a = a' = 3.04$ Å is an HG state, $G = 2.6G_0$ and a channel composition $\{0.90, 0.81, 0.39, 0.16, 0.13\}$, and the asymmetric configuration (LG state) is a local energy minimum in the gap with $d = 2.05$ Å, $a = 2.52$ Å and $a' = 3.57$ Å, and it exhibits a lower conductance ($2.1G_0$) and a corresponding channel composition $\{0.91, 0.57, 0.30, 0.16, 0.12\}$. It is noteworthy that the close top two conductance channels ($0.90G_0$ and $0.81G_0$) in the symmetric HG dimer configuration, are split in the asymmetric LG isomeric, with the conductance being dominated by a single channel ($0.91G_0$); a similar trend is seen in the channel composition of the HG and LG states in the RTN region of the measurements (see inset between panels (b) and (c) in Fig. 29). Two-level behavior is also found for an additional (short) stretching range (with a smaller energy difference between the two states).

Throughout the elongation process described above the structural variations of the NW and of the transport characteristics are reversible. However, past a certain elongation the two-state characteristic behavior ceases, and only a single low conductance state is found,

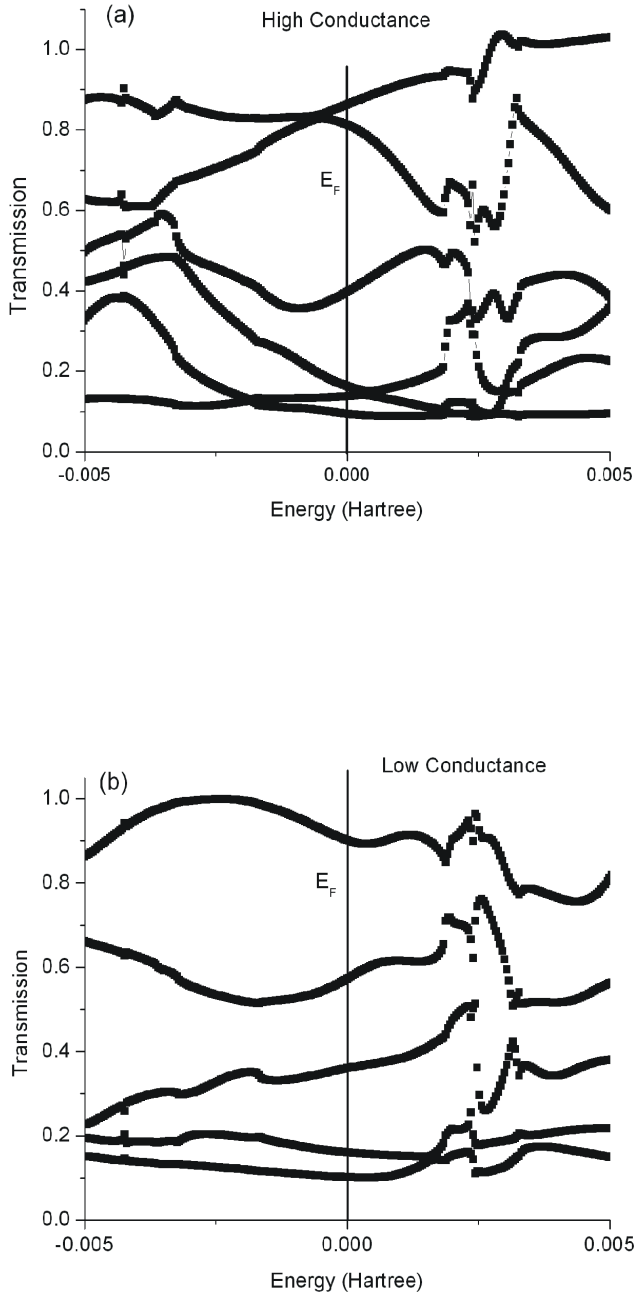

Figure 32: Transmission probability of conduction channels computed by using NEGF algorithm for HG (a) and LG (b) states. Since in our experiments the bias voltage is very low, the relevant transmission probabilities correspond to zero energy ($E = E_F$).

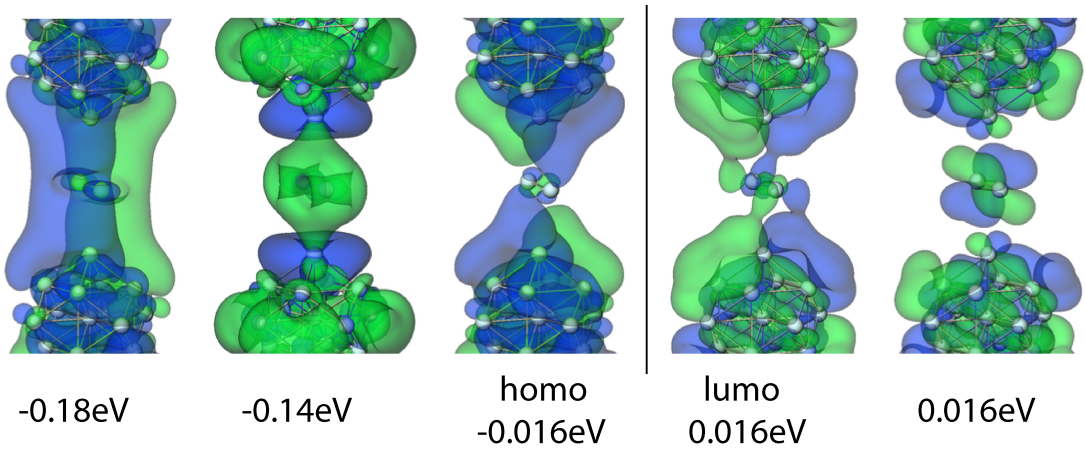

Figure 33: A configuration of the Nb nanowire corresponding to $L_{gap} = 6.63$ Å with superimposed isosurfaces of the highest (lowest) occupied (unoccupied) molecular orbitals, homo (lumo) respectively, as well as several other orbitals with energies close to the Fermi level: see energy values for each orbital with reference to $E_F = 0$. The Fermi level lies between the homo and the lumo orbitals. In the configuration shown here the axis of the suspended Nb dimer makes an angle of 94 degrees with the z-axis (the line connecting the two tip atoms of the electrodes). The other geometric parameters are: the distance between the two Nb atoms in the gap $d = 2.15$ Å and the distance between a Nb atom of the dimer and the nearest Nb ti atom is 3.42 Å . The conductance of this configuration is $3.5G_0$. Note the d-character of the orbitals and their extended nature.

corresponding to an asymmetric dimer. Continued stretching leads to breaking of the NW with the dimer remaining attached to one of the electrodes. This behavior is drastically different from that of gold dimers where the two dimer atoms split and attach themselves to the opposite apexes.

In Fig. 31(b) we display for the HG (symmetric dimer state, $G = 2.6G_0$) and LG (asymmetric dimer state, $G = 2.1G_0$) configurations of the Nb dimer, isosurfaces of wave functions (with energies near the Fermi energy) that are found to have large overlaps with the conductance eigenchannels [10]. The figure provides visualization of the molecular orbitals contributing to electron transport through the NW. The d-character of the orbitals is evident, as well as their extended nature that connects the suspended NW atoms in the gap to the supporting electrodes and leads.

Before closing, we comment on the results of calculations starting with the initial configuration with $L_{gap} = 7.6$ Å , where instead of stretching the contact we compressed it to

a value of $L_{gap} = 6.63$ Å . For this compressed configuration we find that in equilibrium the suspended dimer is tilted with its axis forming an angle of 94 degrees with respect to the axis joining the two tip atoms of the opposing electrodes (see Fig. 33 where we show the atomic configuration of the contact region along with iso-surfaces of the wavefunctions near the Fermi level exhibiting d-character and extended nature). For this configuration, the calculated conductance is $3.5G_0$. It would be of interest to explore experimentally compression of the contact along the (reversible) interval **CD** (see Fig. 28(a)), going beyond point **C**. Such experiments are planned in the nearest future. Another observation requiring both experimental and theoretical clarification is the coincidence along the elongation axis in the jumps from the state with the conductance of $\sim 4.5G_0$ into the HG state (**BC** in Fig. 28(a)) and from the tunnel junction back into the contact mode (**FG** in Fig. 28(a)). The electronic state of the contact along the segment **GH** is similar to the HG state (there are two high-transmission conductance channel); moreover, measurements are much noisier, which might be explained by a tilted dimer configuration being close by energy to the energy of the aligned dimer. The noise can than be caused by the instability in the dimer orientation. Ultimately, experiments involving simultaneous conductance-force measurements (in a MEMS-type device for mechanical stability)and, possibly, shot noise are desirable.

3.4 Summary

In this chapter, transport properties of microfabricated adjustable Nb atomic-size contacts were studied. The conductance of Nb ASC showed upon elongation of the contact by less than 1 Å a reversible evolution from $G \approx 3G_0$ to $G \leq 2G_0$. This included a narrow bistability region where temporal fluctuations between high and low conductance states occur. Measurements in the superconducting state allowed determination of the channel composition as a function of the degree of elongation, revealing a change in the characteristics of the dominant conducting channels between the two states. These results were reproduced and explained by DFT calculations and structural optimizations coupled with conductance evaluations. In particular, we concluded that the Nb ASC consists of a Nb dimer suspended between atomically sharp contacts. The two-level telegraph noise characteristics originate

from shuttling of the dimer between a symmetric (high conductance) and asymmetric (low conductance) configurations. In this manner, we have demonstrated that accurate Nb ASC manipulations and high resolution conductance measurements, in conjunction with high level theoretical simulations, can serve as a reliable electronic transport spectroscopy and an atomic structure microscopy of point contacts.

CHAPTER IV

SUBGAP STRUCTURE IN RESISTIVELY SHUNTED SUPERCONDUCTING ATOMIC-SIZE CONTACTS

In this chapter, I report measurements of the transport properties of superconducting niobium atomic-size contacts in different resistive environments. Embedding resistive shunts close to a junction affected the spectrum of multiple Andreev reflections. In particular, the subgap structure of the current-voltage characteristics shifts to lower voltages. Despite the changes in the subgap structure, methods developed for characterization of superconducting point contacts, including determination of the conductance channel composition, can be directly applied in this layout. Even though I am not aware of a theory which addresses our experimental situation directly, similar changes in the MAR spectrum were predicted to be caused by various pair-breaking effects which affect the coherence of the electronic transport through atomic-size contacts [102].

These experiments are a part of a broader project aimed at creating a special-purpose circuit that enables both voltage-biased (electronic transport) and phase-biased (supercurrent) measurements on the same atomic-size contact configuration. Having the capability to control the quantum phase difference, $\delta\phi$, across Josephson weak links is the key to operating quantum electronic circuits and devices such as SQUIDs and superconducting qubits. Phase-biasing is commonly achieved by incorporating one or more Josephson junctions into a superconducting loop and applying an external magnetic flux. The functionality of a quantum-electronic device critically depends on both the geometric and electronic properties of the circuit as well as the coupling to the electromagnetic environment. This is the case for the recently proposed Andreev level qubit [103, 104], which consists of a quantum point contact, such as a mechanically controlled break junction, embedded in a superconducting loop. In these devices it is important to insure high transmissivity of the junction, which requires knowledge of the conductance channel composition.

In their own right, resistively shunted ultra-small superconducting junctions have recently gained renewed attention in view of the rising interest to the physics of dissipation in macroscopic quantum devices. Carefully designed resistive environments, including shunts as well as networks for reducing the coupling of the junctions to the electromagnetic environment, were shown to cause a superconductor-insulator quantum phase transition in a single tunnel junction [71].

I begin this chapter (Sec. 4.1) with a brief introduction to the Josephson effect in quantum point contacts with a few conductance channels, such as atomic-size MCBJs. In Sec. 4.2, I describe the operating principles and the layout of a novel composite Nb/Ta superconducting circuit for transport and phase-biased experiments. The effect of different shunt resistances are reported in Sec. 4.3. Finally, thermal stability of MCBJs and the temperature independence of the conductance channel composition are mentioned, but detailed investigations are presented elsewhere (Sec. 1.4.4 and Ch. 5).

4.1 Josephson Effect in Superconducting Atomic-Size Contacts

In 1962, Brian Josephson predicted that a surprisingly large supercurrent can flow between two superconductors separated by a thin insulating layer, such as a tunnel barrier, even at zero bias voltage [43]. This current is driven by the superconducting phase difference $\delta\phi$ between the two weakly coupled superconductors. Later, this effect was proven to exist in a variety of systems involving two superconducting electrodes coupled by different "weak links", such as a short wires, point contacts, molecules, carbon nanotubes, etc. [90]. The supercurrent is periodic with respect to $\delta\phi$ and is characterized by the maximum (critical) supercurrent I_c. Generally, both the periodicity and I_c are different for specific systems. In the case of tunnel (superconductor-insulator-superconductor, SIS) junctions between BCS superconductors, Josephson derived that the supercurrent is 2π-periodic, i.e., $I = I_c \sin(\delta\phi)$, with $I_c = \pi\Delta/2eR_N$, where Δ is the superconducting gap, e is the elementary charge, and R_N is the normal resistance of the junction. A unified description of the generic coupling by a weak link (superconductor-weak link constriction-superconductor, S-c-S) based on the

concepts of Andreev reflection [2] and Andreev bound states (see Sec. 1.4.2) was developed in 1990s. In this approach, the transport description is given in terms of the conductance channel composition [5, 28, 82].

In theory, the same set of channels is also responsible for carrying normal electron current across the junction. In thermal equilibrium, the supercurrent through a single channel at a given phase difference is [33]:

$$I(\varphi) = \frac{e\tau_j\Delta}{2\hbar}\frac{\sin(\varphi)}{\sqrt{1-\tau_j\sin^2(\varphi/2)}}\tanh\left[\frac{\Delta}{T}\sqrt{1-\tau_j\sin^2(\varphi/2)}\right]. \tag{23}$$

At low temperatures ($T \ll \Delta$) and in thermal equilibrium, the current phase relation for a weak link with the conductance channel composition $\{\tau_j\} \equiv \{\tau_1, ..., \tau_N\}$ is given by:

$$I(\varphi) = \frac{e\Delta}{2\hbar}\sum_{j=1}^{N}\frac{\tau_j\sin(\varphi)}{\sqrt{1-\tau_j\sin^2(\varphi/2)}}. \tag{24}$$

Even for a single channel, the critical current is not simply proportional to τ_j and, hence, the normal conductance R_N^{-1}:

$$I_c(\tau_j) = \frac{e\Delta}{\hbar}(1-\sqrt{1-\tau_j}). \tag{25}$$

However, Eq. (24) can be reduced to several canonical cases. For example, the Josephson relation can be recovered, assuming that all transmission probabilities are small (i.e., all $\tau_j \ll 1$ as in a tunnel junction) and using the Landauer relation $1/R_N = G_0\sum_{j=1}^{N}\tau_j$. In the opposite ballistic limit all transparencies are equal to unity and the Beenakker-van Houten result [5] for adiabatic impurity-free constrictions can be recovered:

$$I(\varphi) = N\frac{e\Delta}{\hbar}\sin(\varphi/2). \tag{26}$$

Therefore, Eq. (24) appears to interpolate between the Josephson tunnel limit ($I \propto \sin(\varphi)$) and the perfect transmission limit, where $I \propto \sin(\varphi/2)$ behavior is expected. Still, rigorous verification of Eq. (24) remains an outstanding experimental problem.

Due to substantial experimental difficulties, only a few attempts to confirm Eq. (24) indirectly were undertaken. In 1996, Koops *et al.* [47] measured the CPR of an adjustable

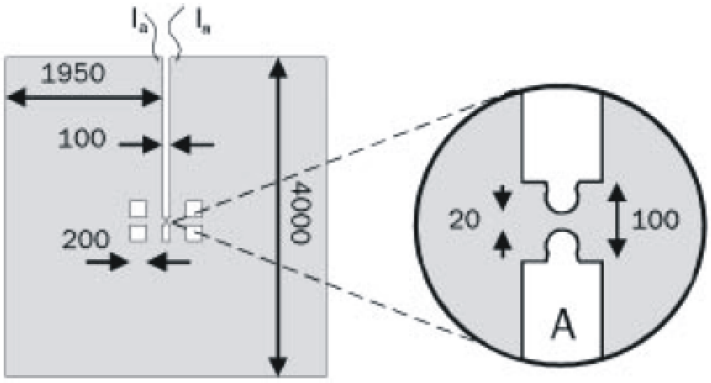

Figure 34: Sample layout for CPR measurement in Nb ASC by Koops *et al.* [47]. The sample was manufactured from 50 μm thick Nb foil by precision laser cutting.

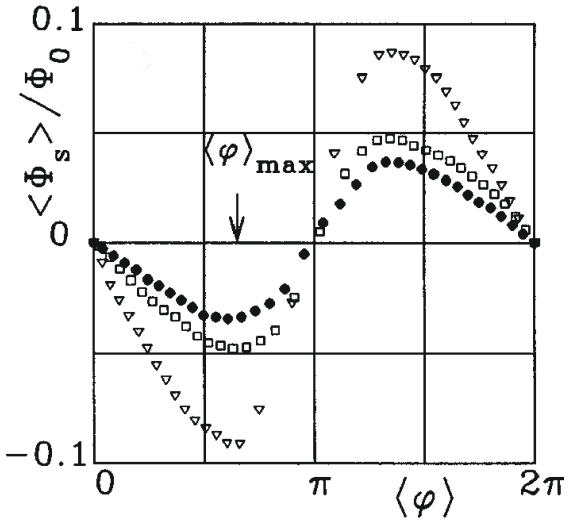

Figure 35: The experimental CPRs of Nb three different atomic-size contacts [47]. The position of the maxima of the CPRs suggest that the CPR not proportional to the fundamental limits of $\sin(\varphi)$ or $\sin(\varphi/2)$ (see text).

Nb ASC incorporated into a laser-cut rf SQUID loop. The sample layout is shown in Fig. 34. While they observed deviations of the CPR from the Josephson sinusoidal behavior (Fig. 35), IV measurements could not be done since the junction was short-circuited by a superconducting loop which has the same superconducting temperature as the junction. Therefore, the conductance channel composition could not be determined.

In 2000, Goffman *et al.* investigated the suppercurrent in aluminum atomic-size contacts with known conductance channel compositions (CCCs) [31]. In that work, instead of phase-biasing, the maximum suppercurrent at zero bias voltage was calculated from the mean current at which switching from the supercurrent to the quasiparticle branch occurs (see Fig. 36). The temperature dependence of the maximum supercurrent, shown for several contacts in Fig. (37), match the theoretical prediction quite well. This experiment demonstrates the relationship between the critical current and the conductance channel composition, which is still only a part of the full current-phase relationship. In the following Section, I describe a microfabricated device [18] which allows exploring the full extent of the current-phase relationship .

4.2 Microfabricated Device Layout

Our circuit's design and functionality are explained in Fig. 38. The composite loop consists of two segments made of different superconductors in perfect contact. The segment made of the material with higher transition temperature, T_{c1}, incorporates a mechanically adjustable ASC. The other segment serves as a resistive shunt between T_{c1} and it own transition temperature, T_{c2}, and becomes a part of the rf SQUID loop at lower temperatures. The break junction's resistance can be reversibly adjusted between "bulk" ($R_{MCBJ} \sim 100\ \Omega$) and "broken" ($R_{MCBJ} > 2\ \mathrm{G}\Omega$). Besides the contact mode (Fig. 38(b)), experimentally significant configurations are: (1) the tunnel mode, used for measuring the superconducting gap (Fig. 38(c)), and (2) the "broken" contact, used for measuring the resistance and the superconducting transition temperature of the shunting segment (Fig. 38(d)). In prototype devices, we used two pairs of gold leads for four-point IV measurements; in experiments targeting CPR measurements as well, a single pair of leads should be attached as close to

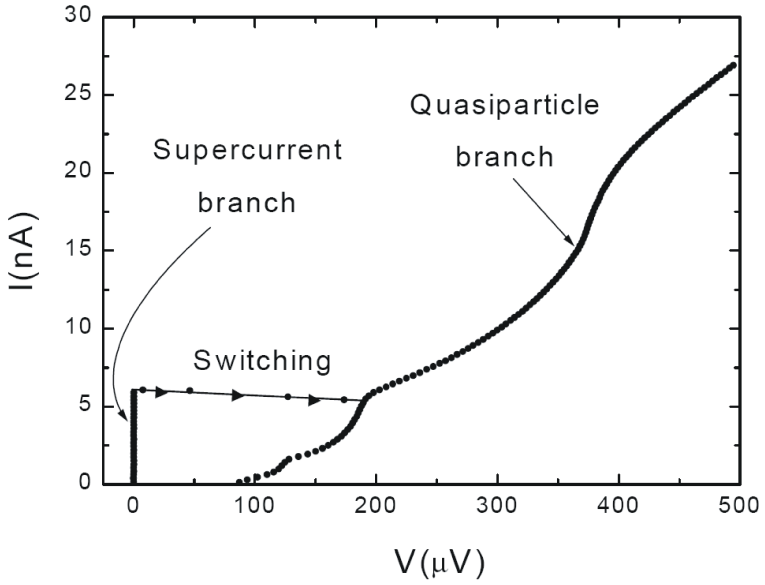

Figure 36: (Adapted from [31, 15]) Typical experimental IV curve of superconducting current-biased Al contact. The characteristic consists of two branches: the supercurrent branch at nearly zero voltage and the quasiparticle branch at finite voltages. Upon increasing the current bias, the contact stays on the supercurrent branch with the voltage staying close to zero, until jumping to a larger finite value. In a carefully designed sample, the current at which such a switching occurs is close to the critical current.

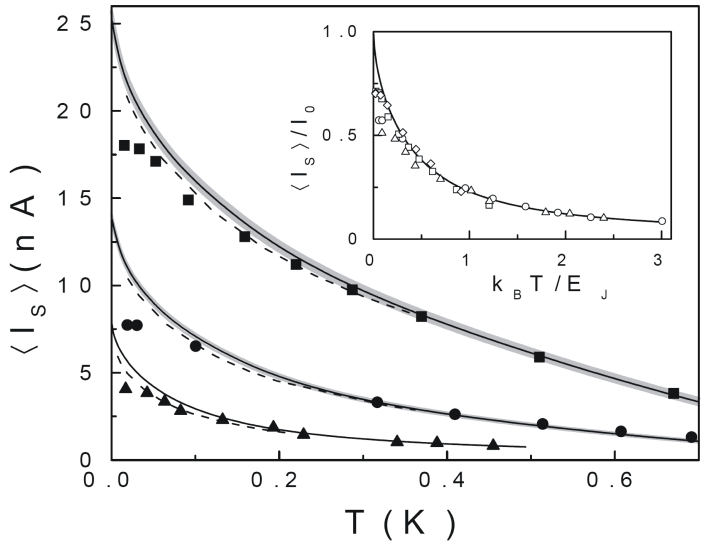

Figure 37: (Adapted from [31, 15]) Mean switching current (normalized to the zero temperature value in the inset) as a function of temperature for three atomic-size contacts with conductance channel compositions determined from transport experiments. Full and dashed lines are theoretical predictions from theoretical models based on the CCC.

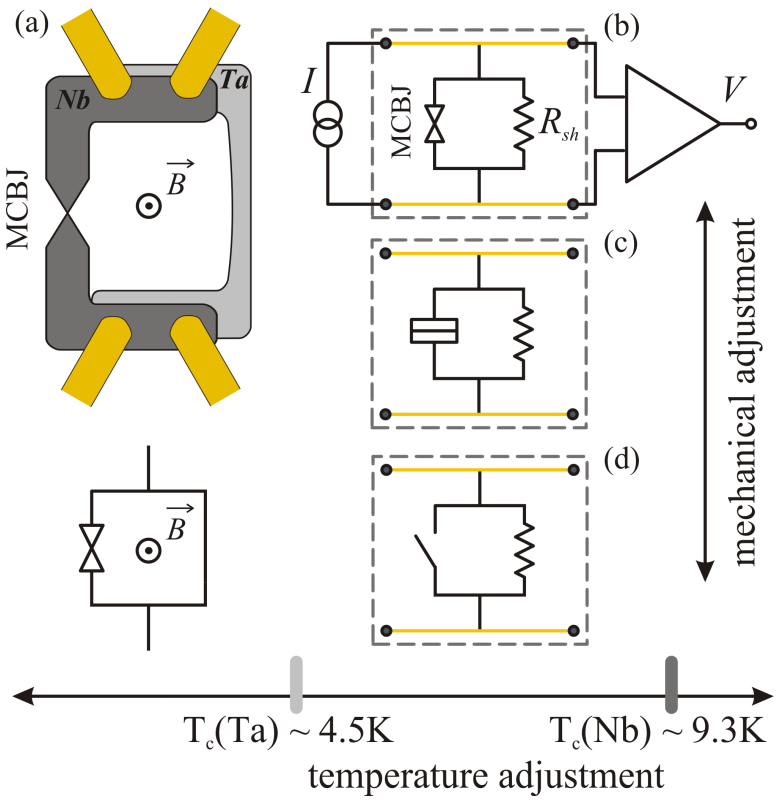

Figure 38: Schematics and operating principle of the circuit. (a) The device is made of two superconducting materials with different transition temperatures (e.g., niobium and tantalum). The circuit's operating regime can be altered both by stretching or compressing the break junction and by varying the temperature. (b) Resistively shunted junction (RSJ) configuration with the MCBJ in the contact mode and the shunting segment in the normal state. (c) Stretched MCBJ in the tunnel mode allows measuring the superconducting gap of the junction material. (d) Further stretching yields the "broken" junction ($R_{MCBJ} >$ 2 GΩ) [18].

the ASC as possible for accurate determination of φ [22].

Our microfabrication sequence is partially based on the thin-film MCBJ technology introduced by van Ruitenbeek *et al.* [95] and is described in detail in Ch. 2. We utilized niobium to form the junction and tantalum to make the shunting segment. This choice was primarily determined by those metals' relatively high transition temperatures, which allowed cost-effective testing. Moreover, Nb is a technologically important material for quantum-electronic applications. To insure perfect contact between the niobium and tantalum segments, we used a multi-source sputterer to deposit two films on top of each other

without breaking the vacuum (Sec. 2.1.3). Subsequently, either of the materials was removed by creating rectangular photoresist masks and selective etching in areas around the junction and the shunting segment (Fig. 39(a), also see Sec. 2.1.5 and 2.1.7). Two major design issues had to be balanced: (1) low loop inductance to avoid multi-valued CPR [22]; (2) sufficiently high normal state shunt resistance. The second requirement was dictated by the need to have the shunt conductance comparable to that of smallest ASC (between one and two conductance quanta, G_0 (G_0^{-1} = 12.9 kΩ). The highest shunting segment resistance we achieved in cryogenic conditions was $\sim$ 2.8 kΩ (Fig. 40). The shunt consisted of 44 suspended Ta wires, each $\sim 200 \times 100$ nm cross-section and 10 μm long, connected in series. The wires detach from the substrate when we wet-etch the Nb sandwiched between the polyimide substrate and the Ta overlay. To prevent the shunt from breaking during mechanical manipulations, we incorporated rectangular anchor pads between wire segments. The meandering pattern (Fig. 39(b)) was used to minimize the loop area and inductance.

4.3 Superconducting Gap Reduction

The sample was measured with well-shielded, battery-operated, analog electronics (see Sec. 2.2.2). The main experimental finding is the shift of the subgap structure (SGS) in resistively shunted Nb MCBJ to lower voltages. This conclusion was made based on a thorough analysis of experimental data from 7 geometrically identical junctions, 3 of which had embedded shunts similar to that shown in Fig. 39. We emphasize data from one sample in particular, where the shunt was intentionally destroyed in the course of experiment by applying excessive current.

To obtain IV characteristics of a resistively shunted junction (RSJ), we subtract the contribution of the resistive shunt: $G_{RSJ} = G_{total} - G_{shunt}$. The resulting SGS was found to be similar to those of unshunted ASC: MAR induce smoothed out current steps in IV curves at voltages around $eV = 2\Delta, 2\Delta/2, 2\Delta/3, ...$, which transform into peaks in differential conductance (dI/dV) curves. It was quickly realized that the gap deduced from such observations was lower than the normal value for all 3 RSJ samples.

In the first RSJ sample, the shunting segment resistance was 800 Ω at 4.2 K. The

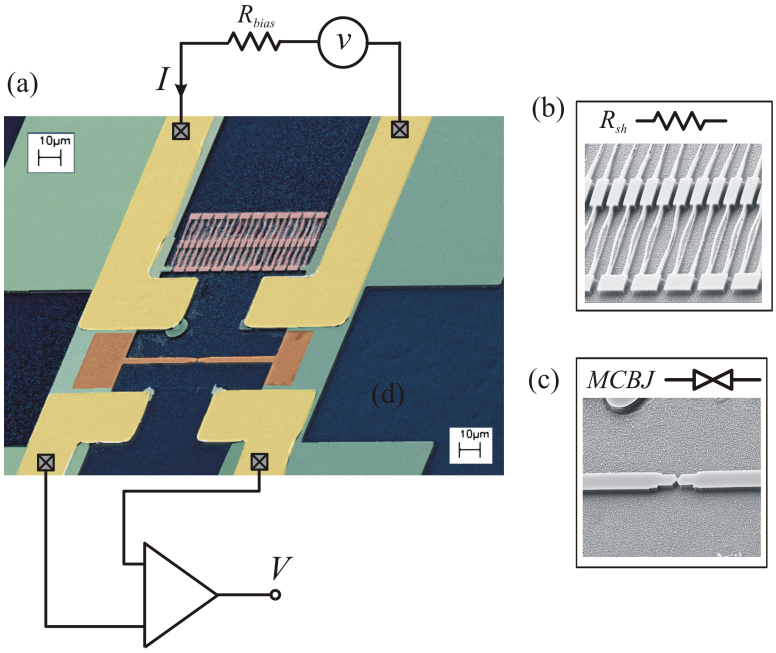

Figure 39: (a) Colorized scanning electron micrograph of the circuit with a diagram of the measurement setup. Metallic structures were deposited on top of an insulating thin polyimide film (dark blue) covering a flexible bronze substrate. The circuit mostly consists of superimposed tantalum and niobium films (green), each $\sim$ 100 nm thick. The top tantalum layer was removed by reactive ion etching in the rectangular area around the break junction, leaving a purely niobium contact (brown). We used energy dispersive x-ray spectroscopy (EDS) microanalysis to verify the absence of tantalum. Subsequently, niobium was wet-etched from the shunt (red). The circuit was operated through two pairs of gold leads (yellow). (b) Magnified view of the tantalum shunt. Both the shunt and the break junction area were patterned by electron beam lithography. (c) The break junction area; the length and the width of the narrowest part are both $\sim$ 100 nm.

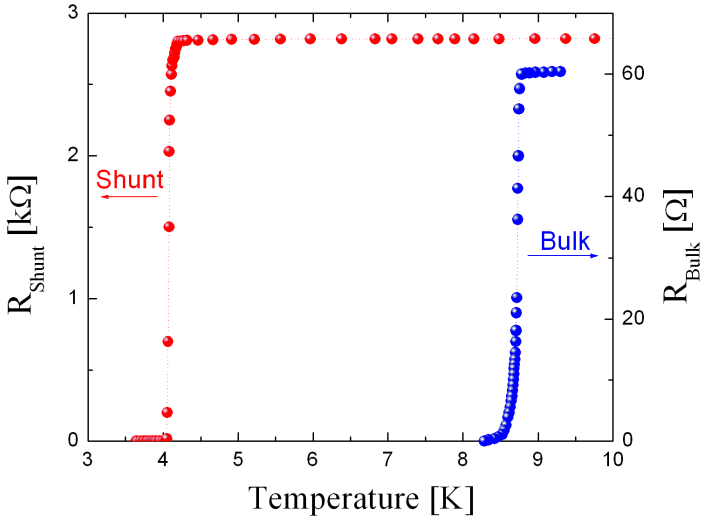

Figure 40: Superconducting transitions in the composite device. Normally, we observe the "bulk" transition of niobium film before stretching the junction for the first time. Later in the experiment, the shunt resistance and transition temperature are measured in the "broken" junction configuration (Fig. 38(d)). We routinely achieve thin-film $T_c = 8.7$ K for Nb and $T_c = 4.1$ K for Ta, which are slightly below corresponding bulk values.

IV characteristics of the junction in parallel with the shunt are shown in Fig. 41(a). The intrinsic IV characteristics of the Nb junctions derived from the IV of the shunted MCBJ are shown in Fig. 41(b). The differential conductance curves were obtained by the numerical differentiations of the curves in panel (b) of Fig. 41. From these curves, we estimated the superconducting gap to be of this RSJ to be about 0.65 meV (the position of the most pronounced non-zero voltage MAR peak is near 2Δ), which is much smaller than the gap of a typical unshunted Nb junction ($\sim$ 1.25 meV at 4.2 K). On top of being shifted to lower voltages, MAR features are significantly distorted rendering the channel composition analysis impossible.

In the second RSJ sample, the shunting segment resistance was 1.8 kΩ. The corresponding IV and dI/dV curves are shown in Fig. 42. The gap value for this sample was estimated to be about 0.9 meV, which is still smaller than the normal gap value. Even though MAR features are more pronounced, a meaningful CCC analysis is still impossible.

In the third RSJ sample, the shunting segments resistance is 2.8 kΩ. The reduction

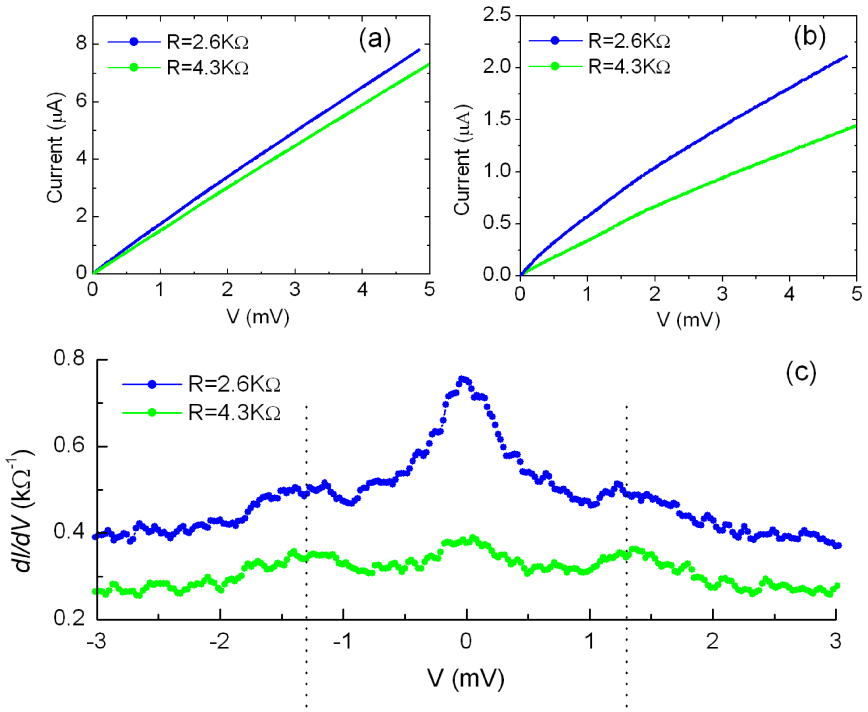

Figure 41: IV characterization of the first RSJ sample with the shunt resistance of 800 Ω at 4.2 K. Results are shown for two configurations with the junction resistances of: (1)2.6 kΩ, (2)4.3 kΩ. (a) IV curves of the junctions in parallel with the shunt. (b) IV curves of Nb junctions after the linear shunt contribution was subtracted. (c) Differential conductance curves numerically derived from the IV characteristics shown in panel (b).

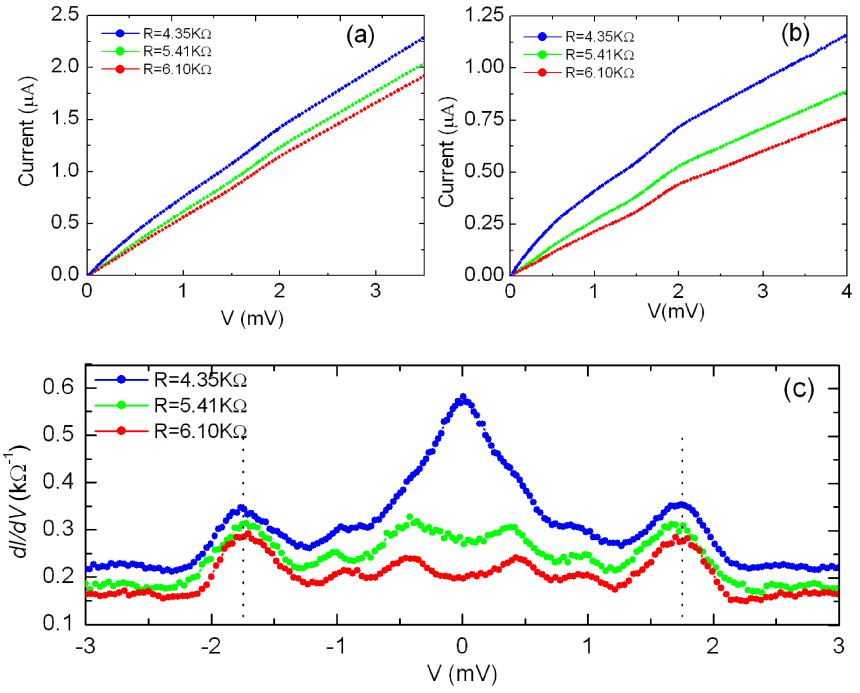

Figure 42: Characterization of the second RSJ sample with a shunt resistance of $\sim 1800\ \Omega$ at 4.2 K. Results are shown for three configurations with the junction resistances of: (1) 4.35 kΩ, (2)5.41 kΩ, (3)6.10 kΩ. (a) IV curves of the junctions in parallel with the shunt. (b) IV curves of Nb junctions after the linear shunt contribution was subtracted. (c) Differential conductance curves numerically derived from the IV characteristics shown in panel (b).

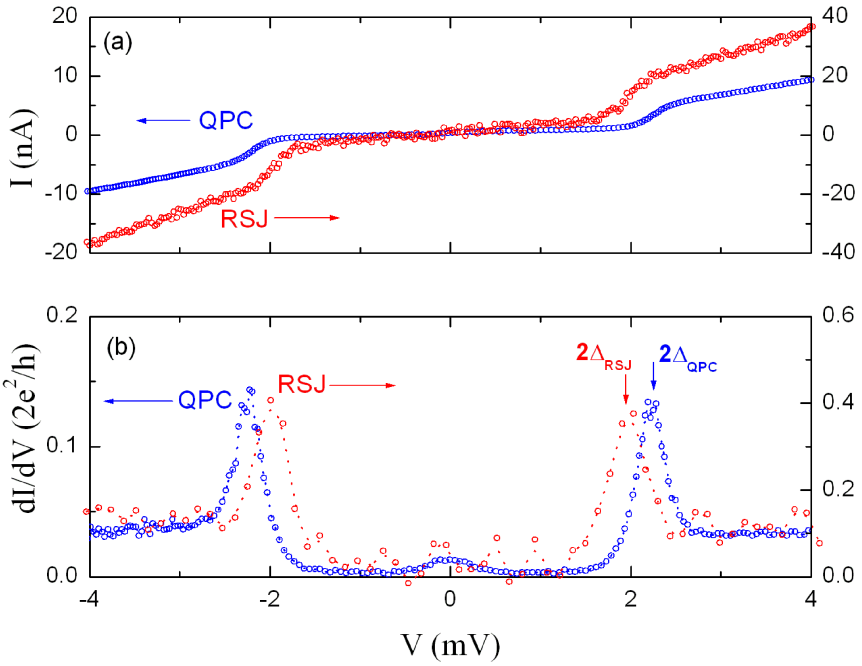

Figure 43: Raw IV (a) and differential conductance (b) tunnel curves obtained from two different samples with identical $T_c = 8.7\ K$. The normal-state ASC resistance was ~ 350 kΩ, that of the RSJ was ~ 100 kΩ (notice the difference in corresponding vertical scales). The ASC circuit did not have an embedded shunt. dI/dV curves were produced by numerical differentiation with smoothing applied to the RSJ data. Broadening of MAR features and substantially higher *voltage* fluctuations were typical for all three RSJ samples. Excess noise might have thermal origin and come from overheating of the shunts.

of the gap value was also observed in this sample. A straightforward illustration is provided by junctions in the tunnel mode (Fig. 43), where the only current enhancement is at $eV = 2\Delta$ exactly. The gap value can be determined more precisely from data reduction, which also yields the CCC. For both RSJ and ASC (MCBJ without shunt), we follow the procedure outlined in Sec. 1.4.3 for unshunted junctions and decompose the IV curves into 5 independent single-channel contributions [78, 58]: $I(V) = \sum_{j=1}^{5} i(V, \tau_j, \Delta)$, which fit the experimental data best. We utilized model $i(V, \tau_j, \Delta)$ curves generated by the simulation code developed at Chalmers University [13, 42, 40, 57]. The fit quality is very sensitive to the value of Δ, which must be found separately. We first evaluate the gap from tunneling curves and/or SGS peaks in dI/dV curves and use it for the initial data reduction. Subsequently, the gap is varied in both directions in steps of 0.01 meV and fitting done to find the optimal value. The results of data reduction are shown in Fig. 44. As it is common for Nb, whose quasiparticle excitation spectrum is slightly different from ideal BCS superconductors, deviations from theoretical models are noticeable in the vicinity of MAR features. These intervals are not included into data reduction [78, 58]. With this stipulation, the quality of fits was virtually identical for unshunted and shunted junctions.

For the third RSJ sample, after we finished the measurement for the RSJ sample, the shunt was burned by applying a high bias current while the Nb junction was in the tunnel mode. After the shunt was destroyed, the gap value increased to the value expected for our unshunted samples. We were able to measure the IV curves for several atomic configurations at different temperature before and after the shunt was intentionally destroyed. From those IV curves, the gap values for different configurations at different temperature was obtained. The results are summarized in Fig. 45. In this figure, circles correspond to the gap values in the contacts made after after the shunt was destroyed; on the other hand, stars represent resistively shunted configurations. Differences in both the values of the gap and its temperature behavior for the two cases are clearly seen. All the unshunted configurations give higher gap values, which also follow the temperature behavior derived from the BCS theory (dashed line). All the shunted configurations give lower gap values, whose temperature behavior deviates from the BCS model.

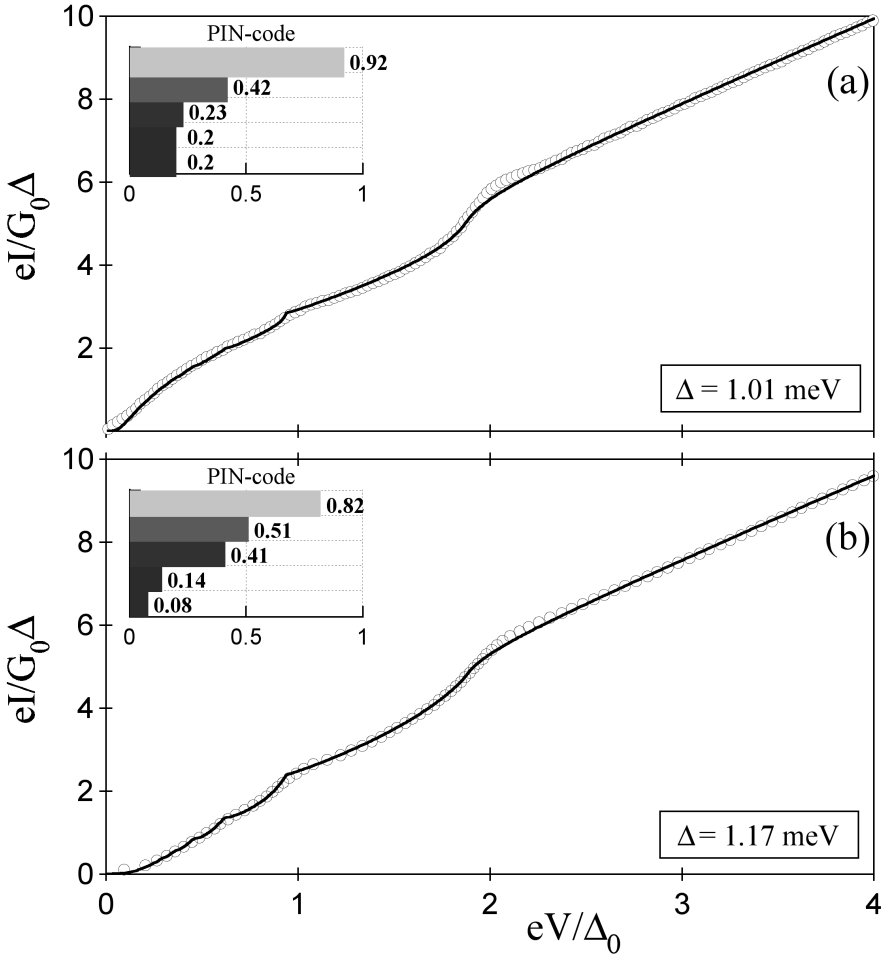

Figure 44: Normalized IV characteristics taken in the same sample before (a) and after (b) destroying the shunt by excessive current at cryogenic temperatures. Both junctions shown have comparable conductances of ($\sim 2G_0$). The presence of the shunt caused $\sim 15\%$ shift in the SGS structure. Solid lines represents best fits, which are of comparable quality.

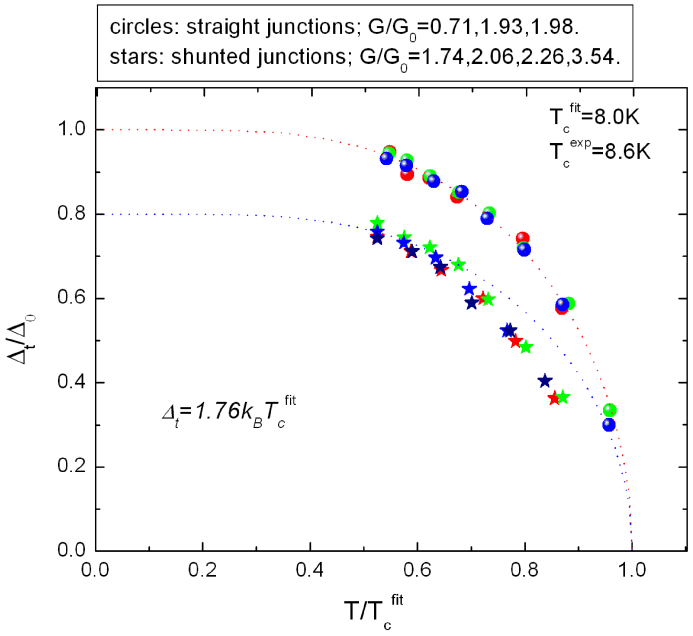

Figure 45: Temperature dependence of the gap in Nb ASCs. The circles show the gap of Nb ASCs after the shunt was destroyed. The stars show the gap of Nb ASCs before the shunt was destroyed. The dotted line shows the theoretical prediction of gap's temperature dependence from the BCS theory.

Finally, thermal stability of both shunted and unshunted junctions was investigated. In accord with preceding studies of aluminum QPC [79], we found that the CCC is temperature-independent (see Sec. 1.4.4) even if the contact is warmed up above the superconducting transition temperature and cooled down to the base temperature (e.g. 4.2 K). Hence the junction will not change its configuration upon cooling the circuit from the RSJ to the rf SQUID configuration. For Andreev level qubit applications, which require substantially lower temperatures, the shunt could be made of titanium ($T_c = 0.35$ K). Its high resistivity will substantially decrease the size and inductance of the qubit loop.

In summary, we have observed shifts of the multiple Andreev reflection spectrum to lower voltages in superconducting niobium atomic-size junctions due to the presence of resistive shunts. Nonetheless, the conductance channel composition of such quantum point contacts can be obtained, if the shunting resistance is high enough, and used in complementary phase-biased experiments.

4.4 Future Work

The microfabricated device introduced in this chapter and the experimental observations made so far provide the foundation for two distinct follow-up experimental directions. Firstly, a similar device, but made of different materials, used at much lower temperatures, and equipped with the CPR measurement circuit can be created and tested as a MAR qubit [103, 104]. In such a setup, direct confirmation of the CPR for atomic-size contacts given by Eq. (24) can be obtained. The second direction points to studies of the influence of the electromagnetic environment, including adjacent microfabricated resistive and reactive *impedances*, on the coherence and dissipation in electronic transport through the junction.

For measurements of the CPR in our samples, we cannot apply a wire loop flux transformer similar to that used in the measurements by Koops *et al.* [47]. Their wire loop flux transformer was pressed against the sample through a 5 μm thick Kapton foil. Such a method is very likely to damage our thin-film samples. Instead, we are developing a pick-up circuit similar to that used for the operation of the superconducting flux qubits [60], which

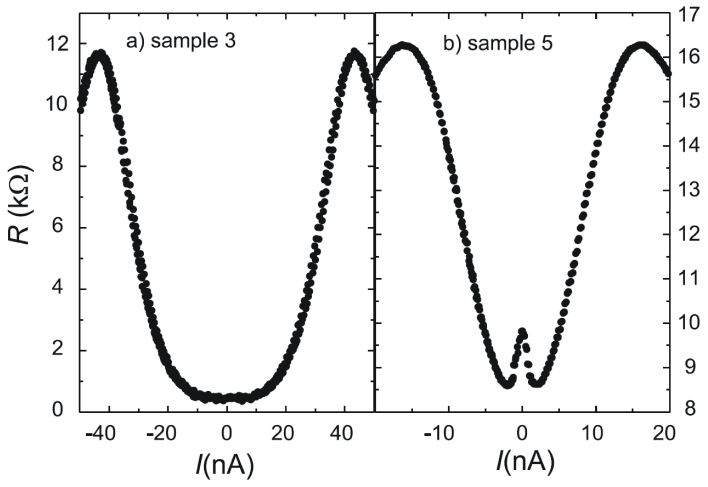

Figure 46: Resistance curves for "superconducting" and "insulating" resistively shunted tunnel Josephson junction. The first sample (S-type) shows a minimum in R at zero bias. The second sample (I-type) shows a resistance peak at zero bias. (a) $R_{shunt} = 11$ kΩ and $R_{junction} = 3.7$ kΩ; (b) $R_{shunt} = 22$ kΩ and $R_{junction} = 12.4$ kΩ

will be microfabricated on the flexible insulating substrate in the vicinity of our composite device. This will also be an important step towards creating a MAR-based superconducting qubit.

Recently, the superconductor-insulator transition (SIT) was observed in resistively shunted single Josephson tunnel junctions [71] and two-dimensional arrays of resistively shunted Josephson junctions [85]. The SIT is caused by quantum mechanical fluctuations of the superconducting phase which destroy superconductivity. In resistively shunted tunnel junctions, the difference between the "superconducting" and "insulating" samples is noticed from the behavior of the resistance near zero current bias. "Superconducting" (S-type) samples exhibit a minimum in R versus I curves near $I = 0$ (see Fig. 46 (a)). "Insulating" (I-type) samples have a resistance peak at zero bias (Fig. 46 (b)). There are two major factors which determine the type of a Josephson junction. The first factor is the shunt resistance (R_s) and the second factor is the ratio of the Josephson energy ($E_j = \hbar\pi\Delta/(4e^2 R_{junction})$) and the Coulomb energy ($E_c = e^2/2C$). The phase diagram from Ref. [71] is shown in Fig. 47. To obtain an I-type sample, the shunt resistance must be larger than 6.5 kΩ and the Josephson energy of the junction must be small.

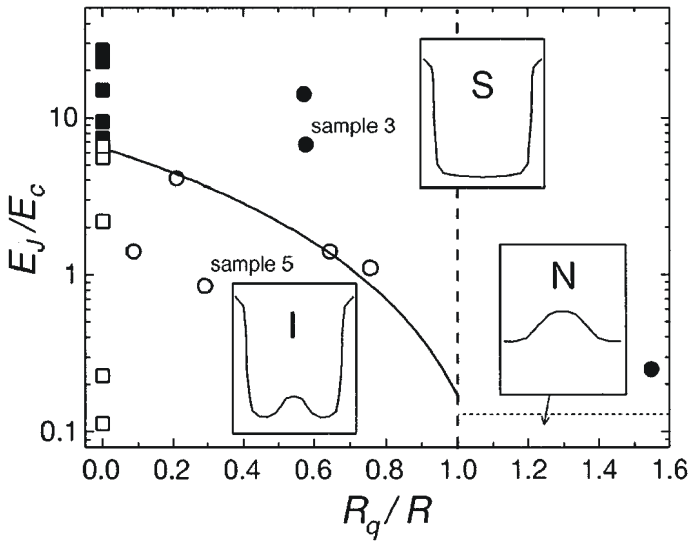

Figure 47: Phase diagram of resistively shunted tunnel Josephson junctions. The phase boundary, which is plotted as a solid line lies between insulator-like (open symbols, I) and superconductor-like (solid symbols, S) samples. To obtain an I-type sample, the shunt resistance must to be larger than 6.5 kΩ and the Josephson energy of the junction must to be small.

We are evaluating and developing microfabricated resistively shunted MCBJ, where similar phenomena can be observed. The differences with the tunnel junctions are: firstly, MCBJ are weak link type Josephson junctions and, secondly, since the normal-state resistance of a MCBJ can be adjusted in a wide range, the SIT boundary can be crossed in a single MCBJ. Primarily, by combining high-precision mechanical manipulation with temperature adjustment and, possibly, the magnetic field, we will be able to have significantly different rates of the Josephson and Coulomb energies (as the junction is stretched, E_j/E_c will decrease). This makes observation of the transition from S-type to I-type in the same sample possible. Finally, care must be taken in order to put an RS-MCBJ into a relatively isolated electro-magnetic environment. This requires the on-the-chip current and voltage leads resistance to exceed 100 kΩ.

CHAPTER V

ANOMALOUS TRANSPORT AND DISSIPATION IN NIOBIUM POINT CONTACTS

In this chapter, I present experimentally found properties of Nb atomic-size contacts which concern energy dissipation (inelastic scattering) and other results outside the realm of the transport theory based on the concept of multiple Andreev reflections. In Sec. 5.1, I describe the evolution of experimentally observed zero-bias anomalies (ZBAs) in a magnetic field, under varying temperature, and under mechanical manipulations. The experimental evidence indicates that these ZBAs are not caused by the Coulomb blockade or the Kondo effect, but are related to superconductivity; however, further experiments are required to substantiate this assessment. This will be followed (Sec. 5.2) by a brief report on the recently started project aiming studies of elastic and inelastic interactions of the conduction electrons with phonons and mechanical degrees of freedom in atomic-size contacts. One of the most exiting prospects is the possibility of observing interaction of the Josephson radiation with vibrational modes of niobium dimers, which, as described in Ch. 3, form the smallest contacts.

5.1 Zero-Bias Anomalies in Superconducting Nb Contacts

Zero-bias anomalies (ZBAs) are ubiquitous in transport through nanoscale systems. Kondo effect and Coulomb blockade are two most recognized types of ZBAs in these systems.

Coulomb blockade was first observed by Giaever in 1968 [29]; it can be modeled by a single electron transistor (SET) shown Fig. 48. In this model circuit, a small system ("quantum dot") is connected to two electrodes through tunneling junctions. The third electrode ("gate") is capacitively coupled to the dot. The gate is used to control the electrical potential of the dot. The electrostatic potential of the dot, which has a charge q, can be written as: $V = q/C$. In this equation, C is the total capacitance of the dot. Since

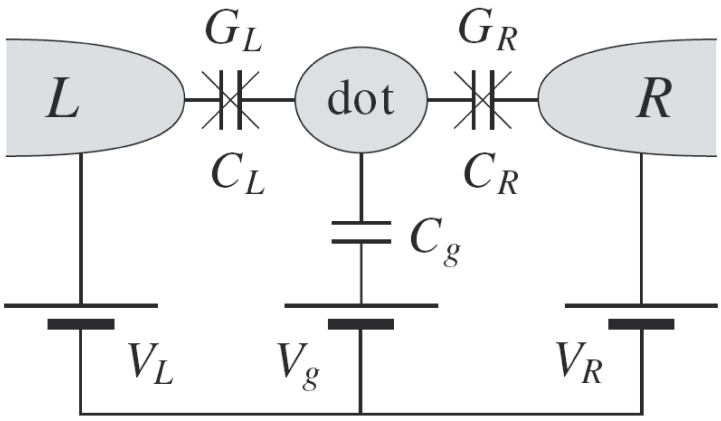

Figure 48: (Adapted from Ref. [74]) An equivalent circuit of a single electron transistor with a quantum dot in the middle. The quantum is connected to left and right electrode by tunneling junctions and is capacitively coupled to gate electrode. In general, the dot can be replace by other small nanoscale system like nanotube, molecule etc.

the system is small, so is the total capacitance. Thus, if an extra electron from one of the electrodes tunnels onto the dot, the electrostatic potential will increase by e/C. Due to a small C, this voltage can be large enough to prevent another electron to tunnel into the dot. Such a Coulomb blockade results in a dip in the conductance curves (or a peak in the the resistance curves) at low bias voltages.

Kondo effect was experimentally discovered in early 1930s in metals containing magnetic impurities [21]. The conventional Kondo effect results from interaction between spins of conduction electrons and the spin of a magnetic impurity [46]. Kondo effect is commonplace in nanoscale systems; it has been observed in various SET setups, where the quantum dot is formed by carbon nanotubes [64], single molecules [68], etc. Unlike Coulomb blockade, Kondo effect results in enhanced conductance at low bias voltages.

Careful characterization of Coulomb blockade or Kondo effect in a nanoscale system requires low temperatures. Also, important experimental "handles" are a magnetic field and, most importantly, an electrostatic gate (see Fig. 48). (For a review of the important physics of both Coulomb blockade and Kondo effect, refer to Ref. [74]).

In our setup, no electrostatic gate is available. On the other hand, we can control the

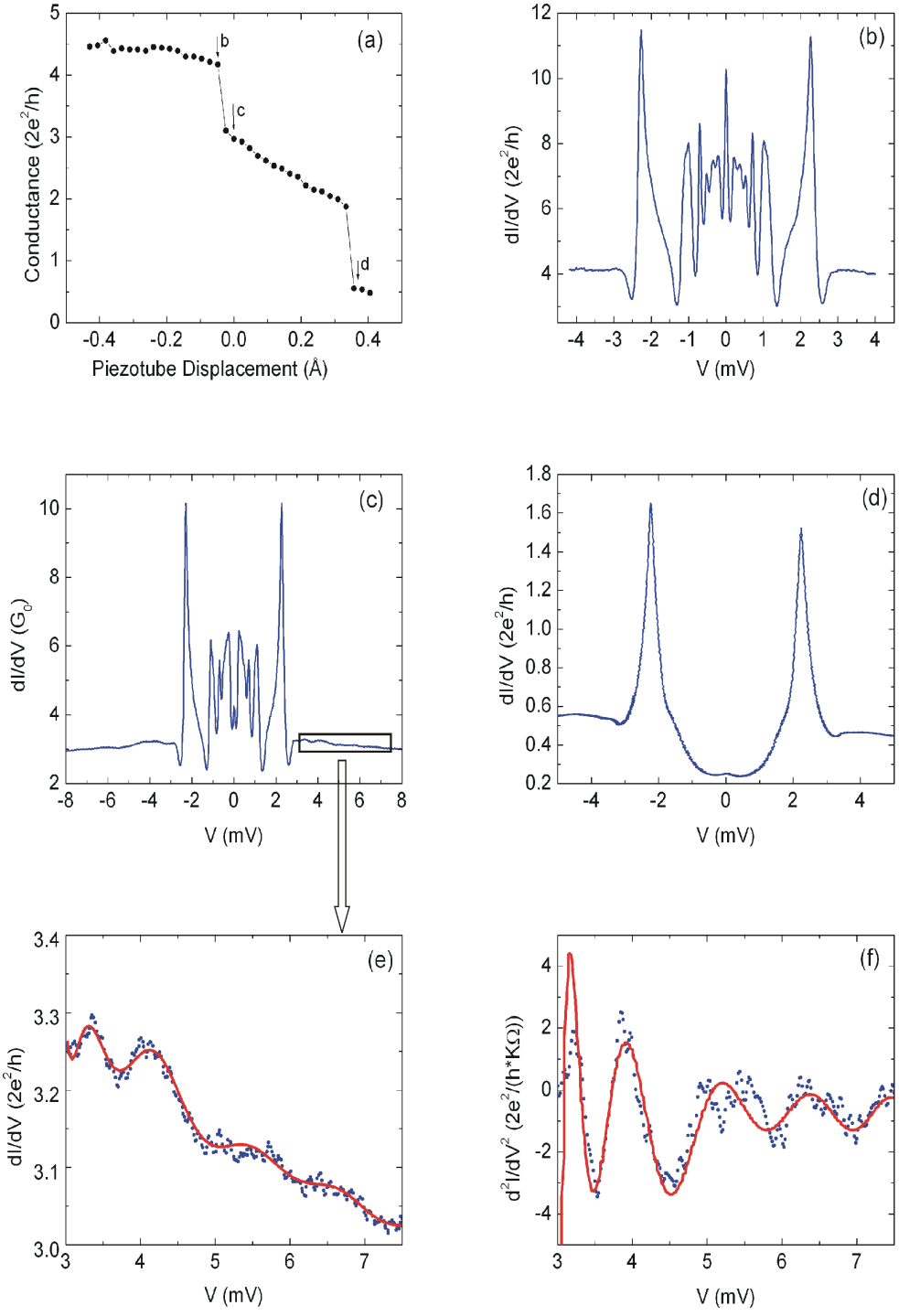

Figure 49: (a) Conductance evolution curve as the Nb ASC is stretched. (b) Conductance versus voltage at $G \approx 4.2G_0$ (point b in panel (a)). (c) Conductance versus voltage at $G \approx 3.0G_0$ (point c in panel (a); this point can identified as an HG state). (d) Conductance versus voltage at $G \approx 0.5G_0$ (point d in panel (a)). (e) The zoom-in of curve in panel (c) between 3 mV and 8 mV. (f) Numerical derivative of the conductance (d^2I/dV^2) plotted in panel (e).

electronic state of the contact to some degree by elongating or compressing the contact. Our experiment are always done at low temperatures and a home-built magnet was built to study transport through atomic contacts both in the superconducting and normal states. In Fig. 49, I review several features that cannot be explained by the transport theory based on the concept of multiple Andreev reflections. Fig. 49 (a) shows a trace of conductance versus elongation. The conductance was calculated from the dissipative branch of IV curves, which were acquired at each point shown in the trace. Measured differential conductance curves shown Fig. 49 (b), (c), and (d) were taken in points b, c, and d shown in panel (a), respectively. It is obvious that panel (d) contains a curve corresponding to a tunnel junction (conductance is depressed in the range of voltages of up 2Δ). Curves (b) and (c) show a complicated structure near 0 V. In particular, sharp peaks at $V = 0$ cannot be explained by MAR transport.

Before discussing these ZBAs, features on the dissipative branch of superconducting ASC ($V > 2\Delta$) must to be mentioned. In Fig. 49 (c), variations in conductance at $V > 2\Delta$ are clearly visible; in addition, the conductance appears to decrease continuously as the bias voltage increases. The rectangular region in panel (c) is expanded in panel (e). Differentiating this curve (shows) that the peak-type structures are superimposed with the conductance decreasing at a constant rate. I will return to these features in Sec. 5.2.

5.1.1 Influence of Mechanical Manipulation

In the smallest Nb contacts, two states (HG and LG) were discovered (Ch. 3). We first look at the behavior of the zero bias features of these states under mechanical manipulation.

Besides the subgap structure, conductance curves in the HG state normally show a peak at 0 V protruding from t a depression in conductance in the range of approximately ± 0.3 mV. Elongation and/or compression does not shift the positions of the features in the SGS, only their mplitudes. As has already been discussed, mechanical manipulations are completely reversible on the conductance plateaus (Ch. 3). The amplitude of zero bias peak in the HG state was observed to decrease monotonously as the Nb contact is stretched (Fig. 50). Ultimately, the 0 V peak disappears, leaving two small rounded peaks

at $V \approx \pm 0.1$ mV. In the LG state, there is no observable peak at zero bias (Fig. 51). During the stretching process, the conductance at zero bias monotonously increases while remaining depressed in comparison with the surrounding structure which can be well modeled by the MAR theory.

5.1.2 Temperature Dependence

Evolution of ZBAs in the HG and LG states were also studied as a function of temperature (Fig. 52 and Fig. 53). Common behavior of the magnitude of the zero-bias conductance was observed: in the beginning, the conductance increases until $T \approx 6.5$ K followed by the decreasing section until T_c where the conductance becomes approximately equal to the conductance on the dissipative branch. These trends are summarized in Fig. 54.

Overall, we believe that the behavior of ZBAs in both states under varying temperature and/or mechanical manipulation can be explained by thermally induced Cooper pair current. Cooper pairs can be moved across the constriction by thermal fluctuations. At first, increasing the temperature will increase this "tunneling" rate. However, fewer pairs are available for "tunneling", thus the current decreases. More generally, at 0 K there is no pair tunneling since there are no thermal fluctuations, and above T_c there are no Cooper pairs to carry the supercurrent. Hence there should be a peak in the amplitude of the thermally activated supercurrent between those extreme temperatures. Similarly, the supercurrent peak will vanish in a tunnel junction if the separation between the electrodes increases. This is the trend we observed in the HG state, which is a weak link rather than a tunnel junction. The trend is opposite in the LG state; however, we believe that it might be caused by atomic reconstructions rather than the normal "tunneling" trends, since the whole SGC structure shows unconventional behavior. In particular, by calculating the conductance channel composition in stretched LG contacts, we observe the most transparent channel to increase its τ with stretching - a result unexpected from ab-initio simulations.

5.1.3 Influence of Magnetic Field

For preliminary experiments described in this section we have made a small superconducting solenoid compatible with our experimental insert. Unfortunately, some wire damage

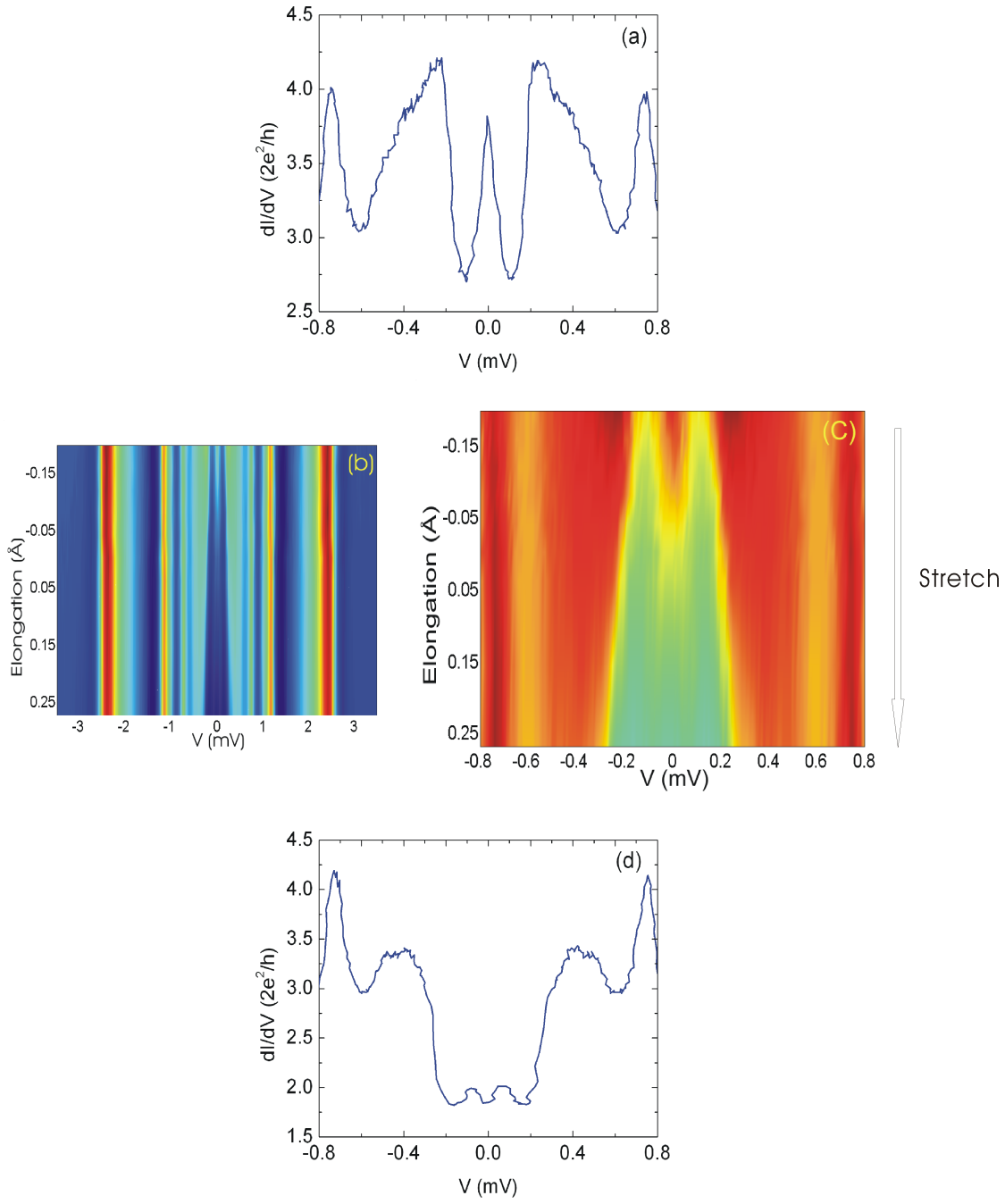

Figure 50: Evolution of ZBA and SGS in the HG state under mechanical manipulation. (a) and (d) contain are the boundary dI/dV curves. Colormap representations of the conductance shown in panel (b) by interpolating between 15 curves. Panel (c) shows the zoom-in by the bias voltage of the central region of panel (b).

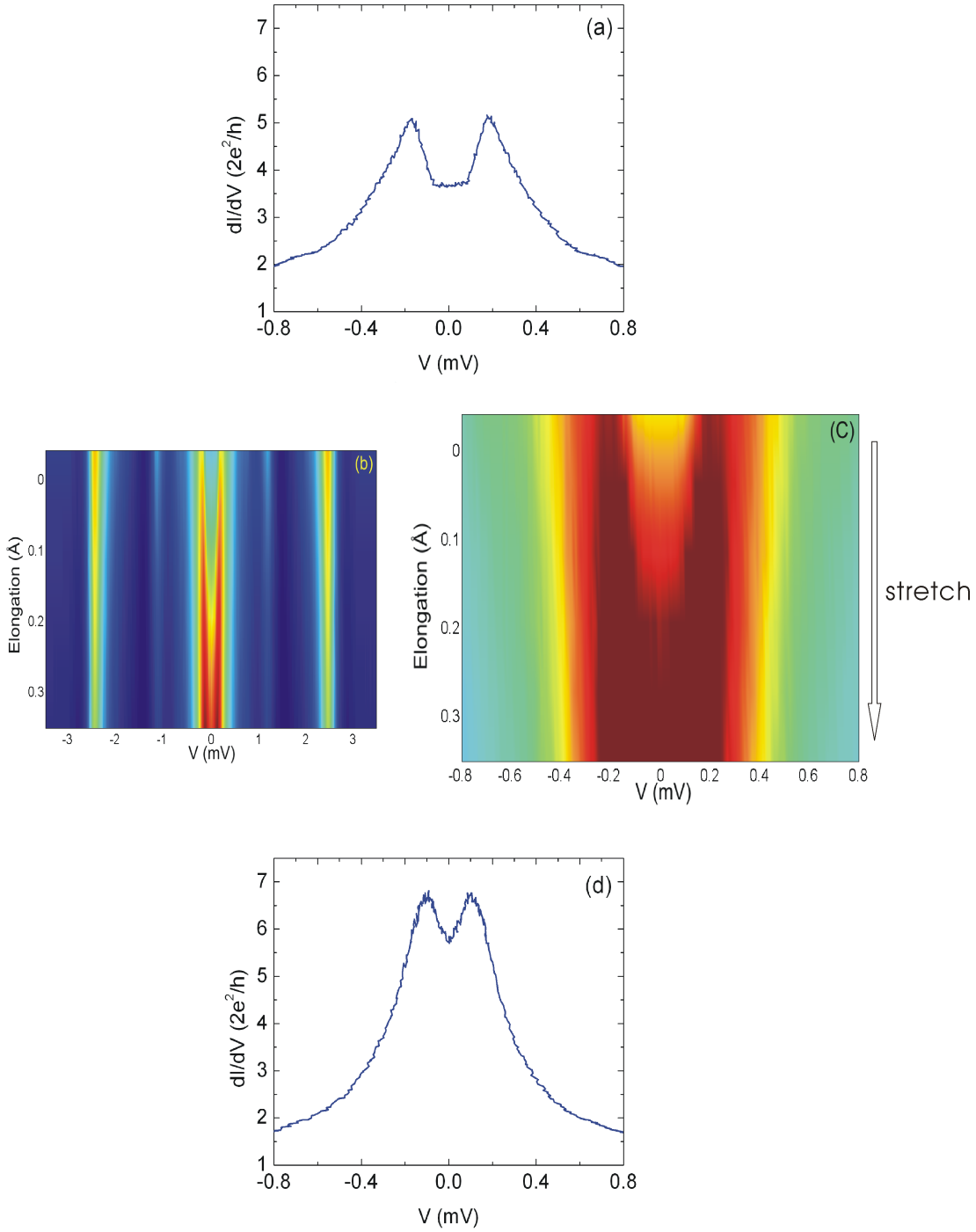

Figure 51: Evolution of ZBA and SGS in the LG state under mechanical manipulation. (a) and (d) contain are the boundary dI/dV curves. Colormap representations of the conductance shown in panel (b) by interpolating between 16 curves. Panel (c) shows the zoom-in by the bias voltage of the central region of panel (b).

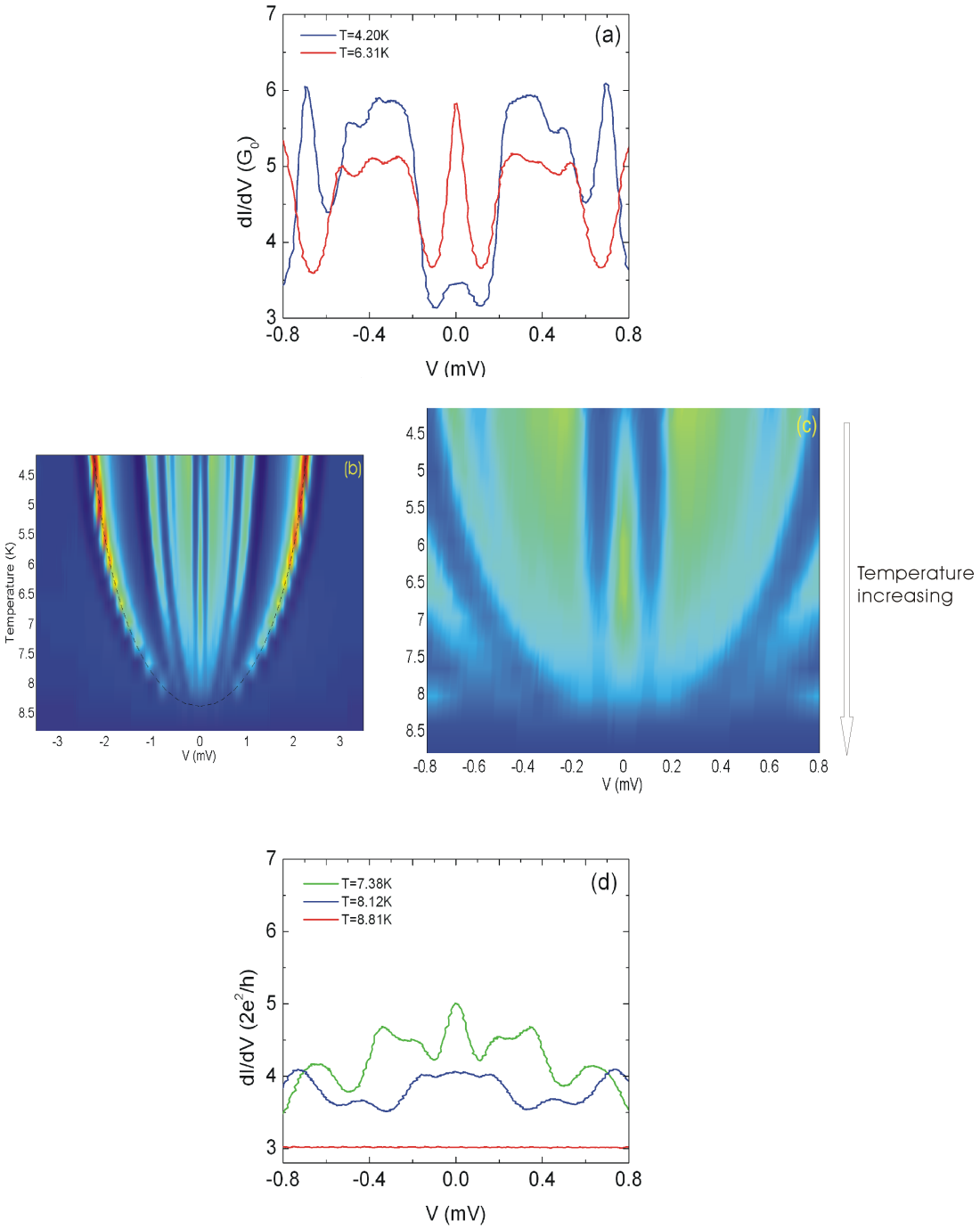

Figure 52: Temperature dependence of the subgap structure and zero-bias anomalies in the HG state. (d) The differential conductance curves at 4.20 K and 6.31 K. (b) The colormap representation of differential conductance versus temperature. The dashed line shows evolution of 2Δ in BCS theory. The peak at zero bias voltage increases at the beginning as the temperature increases. But at temperatures higher than 6.5 K , the peak at zero bias voltage decreases. Panel (c) shows the zoom-in by the bias voltage of the central region of panel (b). (d) The differential conductance curves at 7.38 K, 8.12 K and 8.81 K.

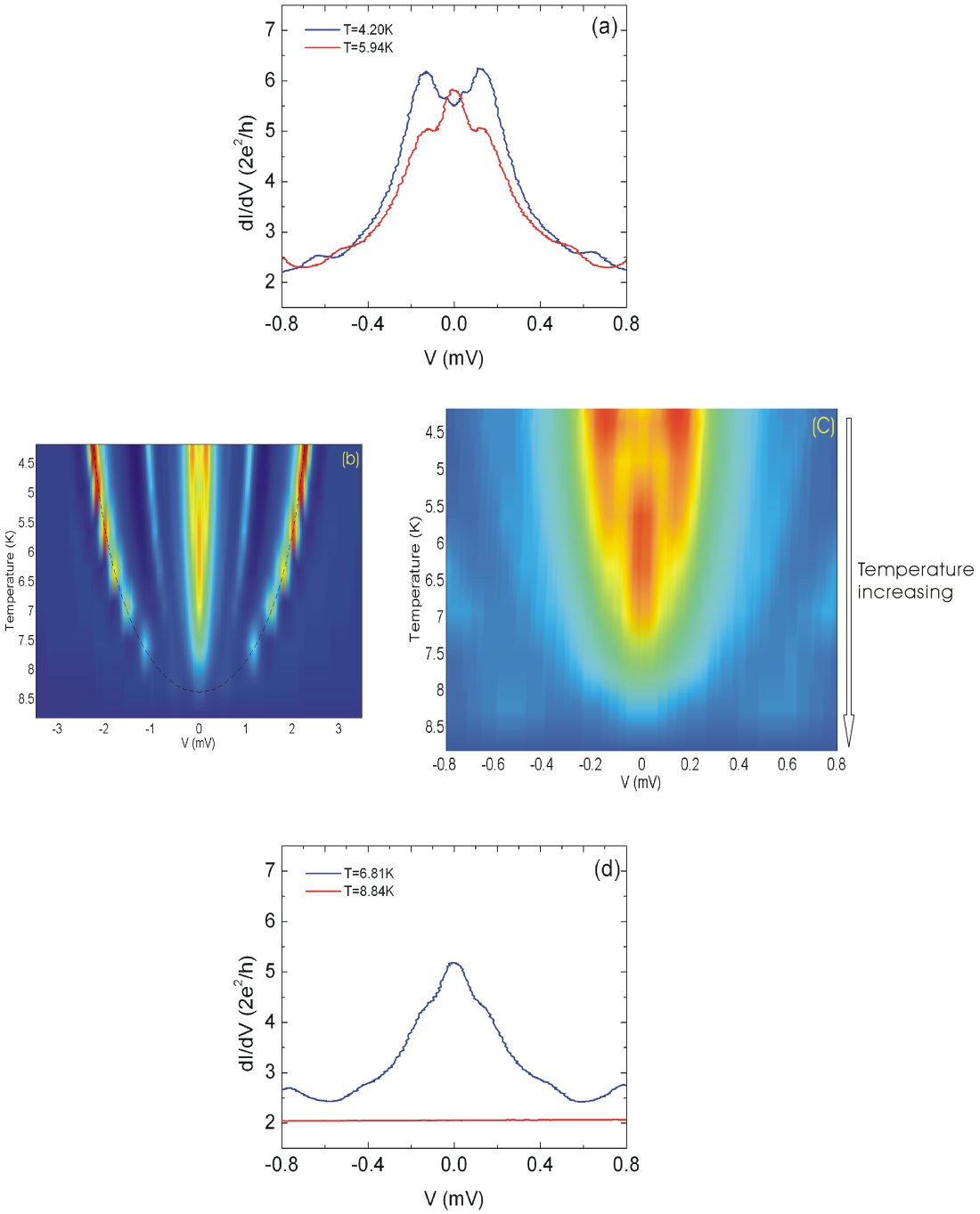

Figure 53: Temperature dependence of the subgap structure and zero-bias anomalies in the LG state. (d) The differential conductance curves at 4.20 K and 5.94 K. (b) The colormap representation of differential conductance versus temperature. The dashed line shows evolution of 2Δ in BCS theory. The peak at zero bias voltage increases at the beginning as the temperature increases. But at temperatures higher than 6.5 K , the peak at zero bias voltage decreases. These trends are identical to those in the HG state. Panel (c) shows the zoom-in by the bias voltage of the central region of panel (b). (d) The differential conductance curves at 6.81 K and 8.84 K.

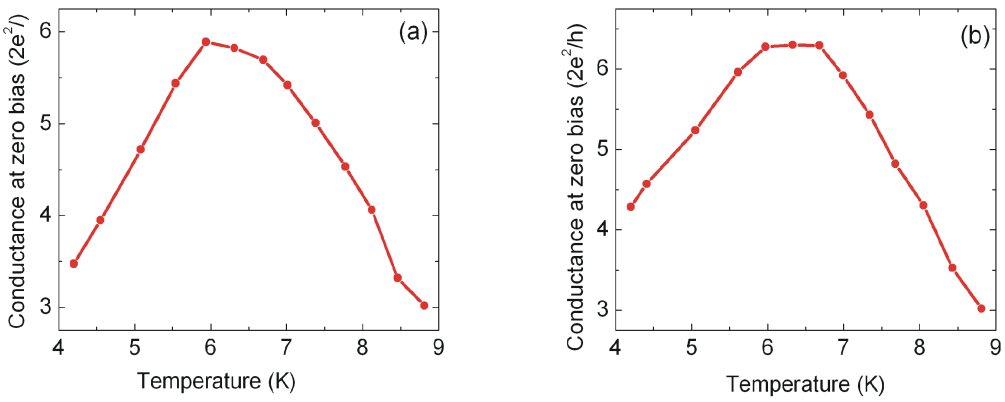

Figure 54: Temperature dependence of conductance at 0 V. (a) Temperature dependence of the conductance at 0 V in the HG state; (b) Temperature dependence of the conductance at 0 V in the LG state.

during the manufacturing and operation prevented the magnet to yield fields sufficient for destroying superconductivity in our Nb thin-film samples. The magnet also lacks a reliable calibration. Therefore I refer to the current in the magnet as a measure of the magnetic field.

The colormap representation of the measured evolution of the SGS in the LG state in a magnetic field in shown in Fig. 55. As the magnetic field becomes stronger (higher current), MAR features shifts closer to 0 V and their amplitudes of become smaller. This is similar to the effect of higher temperatures and is explained by destruction of superconductivity by the field. The conductance at zero bias (shown in Fig. 55 (c)) first increases with increasing magnetic field. However, after some value is reached, the conductance at zero bias decreases as the magnetic field keeps increasing. This trend is exactly the same as what happens t increasing temperatures, however, we did not find even a qualitative explanation yet. More high resolution measurements in both states at much lower temperatures and in higher fields are necessary to see whether the ZBA behavior deviates from a simple qualitative explanation based on the most general behavior of superconducting condensate. We are particularly interested in combined elongation-field experiment targeting the possibility of Kondo-type behavior.

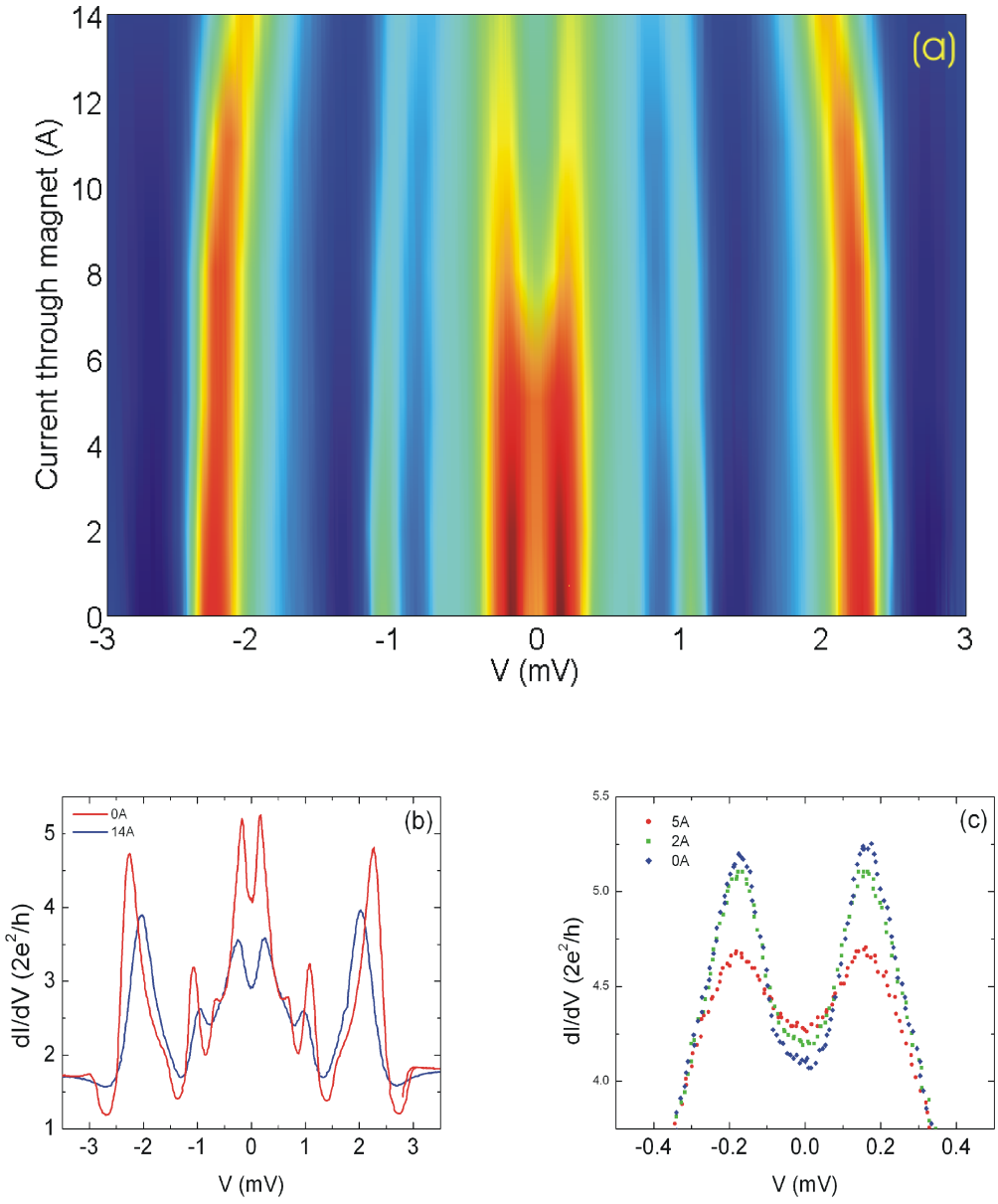

Figure 55: Magnetic field dependence of ZBA in the HG state. (a) Colormap representation of SGS, including ZBA versus magnetic field. The peaks around zero bias voltage decrease as the magnetic field increases. At the beginning, the conductance at zero bias voltage increases with the magnetic field. However, after a certain value is reached the conductance at zero bias voltage decreases. (b) SGS at two values of the magnet current: I_{magnet}= 0 A,14 A. (c) ZBA at I_{magnet} =0 A,2 A,5 A.

5.2 Point Contact Spectroscopy of Superconducting and Normal Niobium Point Contacts

In this section, I report on recent preliminary results of experiments targeting the effect of electron interactions with elementary excitations, defects, and anomalies in the S-c-S and N-c-N niobium systems.

One of the main goals of solid-state physics is investigation of various properties of the matter including mechanical, optical, electronic, etc., with the aim of developing new materials and devices with defined characteristics. There is no universal method to investigate this variety of properties of different materials, which are either conducting or insulating, crystalline or amorphous, thin-layered or bulk, and so on. However, various kinds of *spectroscopies*, like optical, neutron, electron, tunnel, etc., are widely used in solid-state physics. A method of Point-Contact Spectroscopy (PCS) was specifically designed for studying the interaction of conduction electrons with a whole class of elementary excitations in solids (for review, see Refs. [41] and [59]). In this method, a small constriction (typically, a point contact of several nanometers in size) plays a role of a spectrometer. In particular, because of inelastic scattering of accelerated conduction electrons passing through the constriction, the IV characteristic of such as system is nonlinear versus the applied voltage and its second derivative turns out to be proportional to the electron-quasiparticle interaction spectrum. This property of point contacts has been applied to investigations of spectra of different excitations in solids, first of all phonons, as well as magnons, magnetic and nonmagnetic impurities with internal degrees of freedom, and many other processes influenced by the electronic transport. PCS is analogous to the optical absorption spectroscopy, where frequency-dependent absorption of light gives characteristic energy of excitations in insulating materials; hence, PCS measures the imaginary part of conductance electrons self-energy. Conversely, Tunneling Spectroscopy probes the electron density of quasiparticle states and, consequently, measures the real part of of the conduction electron self-energy.

In Fig. 56, I present results of our recent pilot PCS experiment aimed at understanding the nature of non-linearities in the conductance at high bias voltages. This work is still in progress, both experimentally and theoretically; however, we have identified a class of

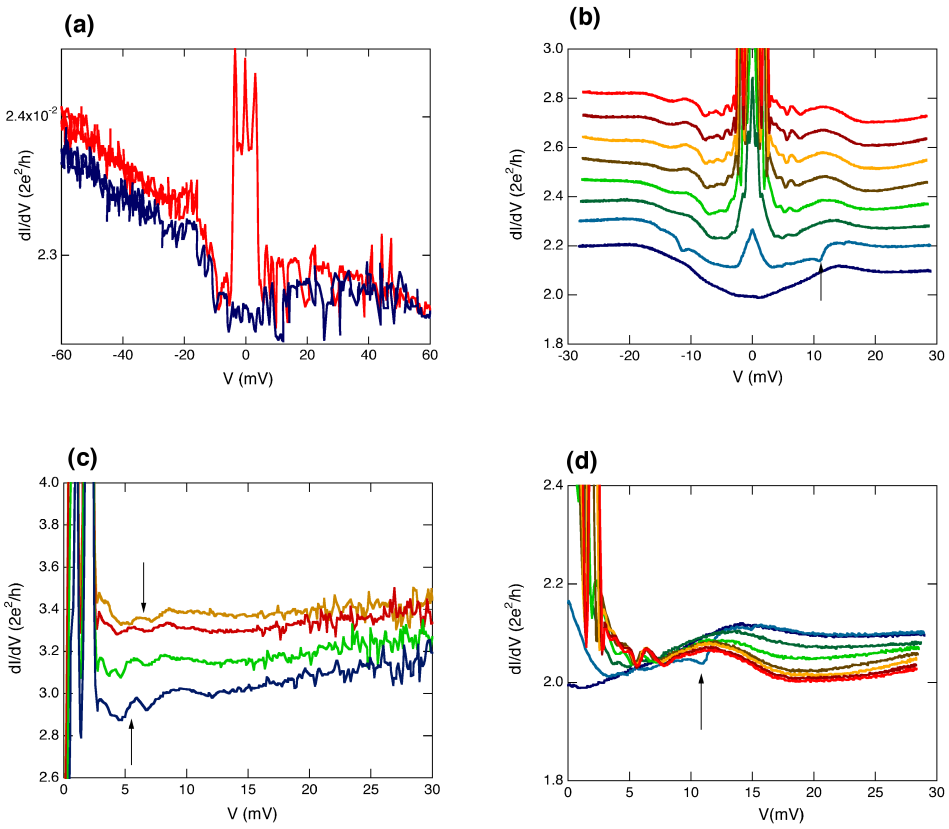

Figure 56: (a) Point contact spectra of a tunnel junction in the normal (blue curve) and the superconducting (red curve) states showing asymmetry and current enhancements, specifically on the left branch. The enhancement voltage corresponds to the frequency of longitudal phonons (ω_L) in bulk niobium. (b) Temperature dependence of features in a PCS spectrum of a contact in the LG state. The temperature of the top curve is 4.2 K; the temperature of the bottom curve is 8.85 K, just above T_c. The curves are offset for clarity. The same characteristics without the offset are shown in panel (d). The feature marked by the arrow appears only near T_c; the dependence of the voltage where this feature appears is the same as of the superconducting gap, Δ. Notice development of features at voltages near 5 mV with temperature. (c) Development of the 5 mV feature as the sample is elongated (from top to bottom, the elongation is about 0.1 Å). Variations in both the amplitude and the position of this feature with elongation indicate that they are related to the properties of the contact area rather than those of the bulk material. It is feasible these features are associated with the interaction of vibrations of the dimer and Josephson radiation.

features (e.g., marked by arrows in Fig. 56) which strongly depend on the temperature, with the dependence reminiscent that of the superconducting gap. We believe that some of them might be associated with the interactions between the mechanical degrees of freedom of the atomic point contact (dimer vibrations) and Josephson radiation. Future research will show whether this exciting proposition can be firmly confirmed.

APPENDIX A

AB-INITIO STRUCTURE AND TRANSPORT SIMULATION METHODS: DESCRIPTION OF THE DFT-NGEF PROCEDURE

Ab-initio simulation of molecule devices or ASC involve setting up a many-body Schrodinger equation, where the Hamiltonian can be written as:

$$\hat{(}H) = -\sum_{i=1}^{n} \frac{\hbar}{2m} \nabla_i^2 - \sum_{i=1}^{n} \sum_{\mu=1}^{N} \frac{Z_\mu e^2}{|\vec{r_i} - \vec{R_\mu}|} + \frac{1}{2} \sum_{i,j=1}^{n} \frac{e^2}{|\vec{r_i} - \vec{r_j}|}. \tag{27}$$

In Eq. (27), the first term is the kinetic energy of electrons; the second term represents the electron-ion interaction and the third term represents the electron-electron interaction. Since no solution, even numerical, is feasible for a system with more than just a few atoms, approximations are needed to simplify the many body problem. The most basic is the Bohr-Oppenheimer approximation, which fixed the positions of the nuclei, since the electrons move much faster. Furthermore, in the Density Functional Theory (DFT), electrons are considered as non-interacting particles moving in the effective potential generated by other

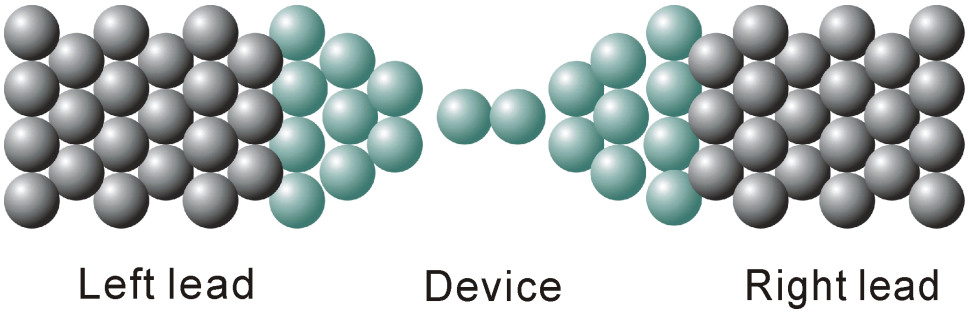

Figure 57: A schematic layout of the system used in numerical simulations. Such an "open" system consists of two semi-infinite crystalline electrodes (left lead and right lead) and the device area (scattering region). The device area usually includes the scatterer (molecule, nanowire, etc.) and several layers of each of the electrodes.

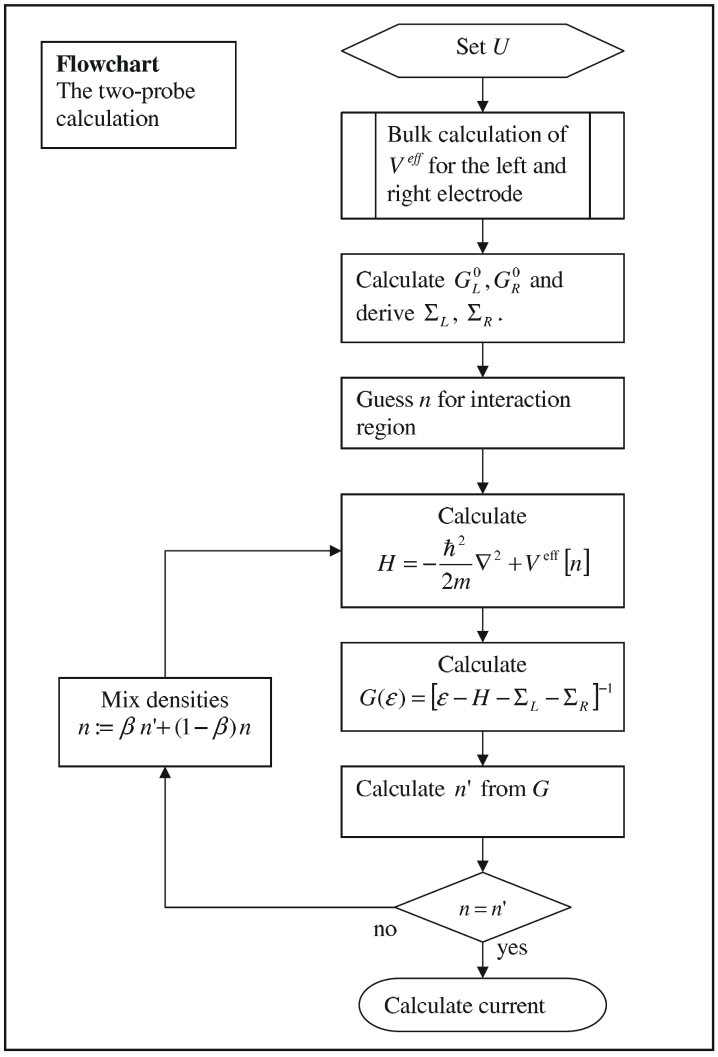

Figure 58: Flowchart of ab-initio non-equilibrium Green's function algorithm used to compute the Green function in the device region of Fig. 57

electrons. This this approximation, the electron density has proven to be an adequate replacement or all the wavefunctions of all the electrons in the system. The electron density must be computed self-consistently, which involves following steps:

1. Guess the electron density (n) ;

2. Compute the effective potential from the election density;

3. With the effective potential, the Schrodinger equation; can be solved. From the wavefunction, the electrons position (n') can be calculated;

$$n(\vec{r}) = \sum_{\varepsilon_\alpha < \mu} |\psi_\alpha(\vec{r})|^2 \tag{28}$$

4. compare the new electron density with old electron density n. If they are different, let $n = \beta\ n' + (1-\beta)n$, repeat step 2.

Nb ASCs can be be modeled as a standard DFT-NEGF system shown in Fig. 57. It is divided into three regions: the left lead, the right lead, and the device region (scatterer). In this model system, only interaction between adjacent regions (left lead-device and right lead-device) are taken into account (τ_1 and τ_2). Hence, theHamiltonian can be expressed in the matrix form as:

$$\hat{H} = \begin{pmatrix} \hat{H}_1 & \tau_1 & 0 \\ \tau_1^\dagger & \hat{H}_d & \tau_2^\dagger \\ 0 & \tau_2 & \hat{H}_2 \end{pmatrix} \tag{29}$$

To further simplify the computation, instead of fully solving the Schrödinger equation, the Green's function is calculated. Green's function of the device regime can be expressed as:

$$G_d = (E - H_d - \Sigma_1 - \Sigma_2)^{-1} \tag{30}$$

$$\Sigma_1 = \tau_1^\dagger\ G_1\ \tau_1 \quad \text{and} \quad \Sigma_2 = \tau_2^\dagger\ G_2\ \tau_2 \tag{31}$$

Σ_1 and Σ_2 in Eq. (29) are the "self-energies" of the leads. Efficient numerical algorithms exist for calculating Green's (G_1 and G_2) functions of periodic semi-infinite systems, such

as the leads. Once the Green's functions are found in the device region, the total charge density matrix can be calculated:

$$\hat{\rho} = \frac{2\ (forspin)}{2\pi} \int_{E=-\infty}^{\infty} dE \sum_i f(E, \mu_i) G_d \Gamma_i G_d^{\dagger} \tag{32}$$

$$where\ \ \Gamma_i = i(\Sigma_i - \Sigma_i^{\dagger}) \tag{33}$$

With charge density matrix in hand, the electron density can be written as:

$$n(\vec{r}) = Tr\hat{\rho} \tag{34}$$

The full self-consistent NEGF algorithm flow chart is shown in Fig. (58). After the self-consistent Green's function is found for the device, the electronic current through the device between the two leads is given by:

$$I = \frac{e}{\pi\hbar} \int_{E=-\infty}^{\infty} dE(f(E, \mu_1) - f(E, \mu_2)) Tr(G_d^{\dagger}\ \Gamma_2 G_d \Gamma_1) \tag{35}$$

This expression is very similar the the transport relation written during the discussion of the Landauer scattering approach. Now, the scattering matrix is given by $Tr(G_d^{\dagger}\ \Gamma_2 G_d \Gamma_1)$. The eigenvalues of this matrix give the conduction channel composition. An example of the theoretical simulations of conduction channel composition in HG and LG states is shown in Fig. 32. Since the bias voltage is small in our experiments, the transmission probability for our samples is corresponding to energy = 0 in both Fig. (32).

REFERENCES

[1] Agraït, N., Levy Yeyati, A., and van Ruitenbeek, J. M., "Quantum properties of atomic-sized conductors," *Phys. Rep.*, vol. 377, pp. 81–279, 2003.

[2] Andreev, A. F., "The thermal conductivity of the intermediate state in superconductors," *Sov. Phys. JETP*, vol. 19, pp. 1228–1231, 1964.

[3] Averin, D. and Bardas, A., "ac Josephson effect in a single quantum channel," *Phys. Rev. Lett.*, vol. 75, pp. 1831–1834, 1995.

[4] Barnett, R. N. and Landman, U., "Born-Oppenheimer molecular-dynamics simulations of finite systems: Structure and dynamics of $(H_2O)_2$," *Phys. Rev. B*, vol. 48, pp. 2081–2097, 1993.

[5] Beenakker, C. W. J. and van Houten, H., "Josephson current through a superconducting quantum point contact shorter than the coherence length," *Phys. Rev. Lett.*, vol. 66, pp. 3056–3059, 1991.

[6] Bhushan, B., Israelachvili, J. N., and Landman, U., "Nanotribology: friction, wear and lubrication at the atomic scale," *Nature*, vol. 374, pp. 607–616, 1995.

[7] Blanter, Y. M. and Büttiker, M., "Shot noise in mesoscopic conductors," *Phys. Rep.*, vol. 336, pp. 2–166, 2000.

[8] Blonder, G. E., Tinkham, M., and Klapwijk, T. M., "Transition from metallic to tunneling regimes in superconducting microconstrictions: Excess current, charge imbalance, and supercurrent conversion," *Phys. Rev. B*, vol. 25, pp. 4515–4532, 1982.

[9] Bogachek, E. N., Scherbakov, A. G., and Landman, U., "Magnetic switching and thermal enhancement of quantum transport through nanowires," *Phys. Rev. B*, vol. 53, pp. R13246–R13249, 1996.

[10] Brandbyge, M., Sørensen, M. R., and Jacobsen, K. W., "Conductance eigenchannels in nanocontacts," *Phys. Rev. B*, vol. 56, pp. 14956–14959, 1997.

[11] Brandbyge, M., Taylor, J., Stokbro, K., Mozos, J.-L., and Ordejon, P., "Density functional method for nonequilibrium electron transport," *Phys. Rev. B*, vol. 65, p. 165401, 2002.

[12] Bratus', E. N., Shumeiko, V. S., Bezuglyi, E. V., and Wendin, G., "dc-current transport and ac Josephson effect in quantum junctions at low voltage," *Phys. Rev. B*, vol. 55, pp. 12666–12677, 1997.

[13] Bratus', E. N., Shumeiko, V. S., and Wendin, G., "Theory of subharmonic gap structure in superconducting mesoscopic tunnel contacts," *Phys. Rev. Lett.*, vol. 74, pp. 2110–2113, 1995.

[14] Büttiker, M., "Scattering theory of current and intensity noise correlations in conductors and wave guides," *Phys. Rev. B*, vol. 46, pp. 12485–12507, 1992.

[15] Cron, R., *Atomic contacts: a test-bed for mesoscopic physics*. PhD thesis, Université P. et M. Curie, Paris, France, 2001.

[16] Cuevas, J. C., Levy Yeyati, A., and Martín-Rodero, A., "Microscopic origin of conducting channels in metallic atomic-size contacts," *Phys. Rev. Lett.*, vol. 80, pp. 1066–1069, 1998.

[17] Cuevas, J. C., Martín-Rodero, A., and Levy Yeyati, A., "Hamiltonian approach to the transport properties of superconducting quantum point contacts," *Phys. Rev. B*, vol. 54, pp. 7366–7379, 1996.

[18] Dai, Z. and Marchenkov, A., "Subgap structure in resistively shunted superconducting atomic point contacts," *Appl. Phys. Lett.*, vol. 88, p. 203120, 2006.

[19] Datta, S., *Electronic Transport in Mesoscopic Systems*. Cambridge: Cambridge University Press, 1995.

[20] de Gennes, P. G., *Superconductivity of Metals and Alloys*. New York: W. A. Benjamin, 1966.

[21] de Haas, W. J., de Boer, J., and van den Berg, G. J., "The electrical resistance of gold, copper and lead at low temperatures," *Physica*, vol. 1, pp. 1115–1124, 1934.

[22] de Wolff, E., Roobeek, H. C., Koops, M. C., and de Bruyn Ouboter, R. *Physica B*, vol. 179, pp. 295–308, 1992.

[23] Eigler, D. M., Lutz, C. P., and Rudge, W. E., "An atomic switch realized with the scanning tunneling microscope," *Nature*, vol. 352, pp. 600–603, 1991.

[24] Eigler, D. M. and Schweizer, E. K., "Positioning single atoms with a scanning tunnelling microscope.," *Nature*, vol. 344, pp. 524–526, 1990.

[25] Face, D. W. and Prober, D. E., "Nucleation of body-centered-cubic tantalum films with a thin niobium underlayer," *J. Vac. Sci. Technology A*, vol. 5, no. 6, pp. 3408–3411, 1987.

[26] Ferry, D. K. and Goodnick, S. M., *Transport in Nanostructures*. Cambridge University Press, 1997.

[27] Fisun, V. V. and Yanson, Y. I., "Conductance quantization in metal nanowires produced by chemical anodization," *Low Temp. Phys.*, vol. 27, pp. 1264–1267, 2001.

[28] Furusaki, A., Takayanagi, H., and Tsukuda, M., "Theory of quantum conduction of supercurrent through a constriction," *Phys. Rev. Lett.*, vol. 67, pp. 132–135, 1991.

[29] Giaever, I. and Zeller, H. R., "Superconductivity of small tin particles measured by tunneling," *Phys. Rev. Lett.*, vol. 20, no. 26, pp. 1504–1507, 1968.

[30] Gimzewski, J. K., Möller, R., Pohl, D. W., and Schlittler, R. R., "Transition from the tunneling regime to point contact investigatedby scanning tunneling microscopy and spectroscopy," *Surface Science*, vol. 189/190, pp. 15–23, 1987.

[31] Goffman, M., Cron, R., Levy Yeyati, A., Joyez, P., Devoret, M. H., Esteve, D., and Urbina, C., "Supercurrent in atomic point contacts and Andreev states," *Phys. Rev. Lett.*, vol. 85, pp. 170–173, 2000.

[32] Grönbeck, H., Rosén, A., and Andreoni, W., "Structural, electronic, and vibrational properties of neutral and charged nb_n ($n = 8, 9, 10$) clusters," *Phys. Rev. A*, vol. 58, no. 6, pp. 4630–4636, 1998.

[33] Haberkorn, W., Knauer, H., and Richter, J., "A theoretical study of the current-phase relation in Josephson contacts," *Phys. Stat. Sol.*, vol. 47, pp. K161–K164, 1978.

[34] Häkkinen, H., Barnett, R. N., Scherbakov, A. G., and Landman, U., "Nanowire gold chains: formation mechanisms and conductance," *J. Phys. Chem. B*, vol. 104, pp. 9063–9066, 2000.

[35] Halbritter, A., Borda, L., and Zawadowski, A., "Slow two-level systems in point contacts," *Adv. in Physics*, vol. 53, no. 8, pp. 939–1010, 2004.

[36] Halbritter, J., "Transport in superconducting niobium films for radio frequency applications," *J. Appl. Phys.*, vol. 97, no. 8, p. 083904, 2005.

[37] Hohenberg, P. and Kohn, W., "Inhomogeneous electron gas," *Phys. Rev.*, vol. 136, pp. B864–B871, 1964.

[38] Huggins, H. A. and Gurvitch, M., "Magnetron sputtering system equipped with a versatile substrate table," *J. Vac. Sci. Technology A*, vol. 1(1), pp. 77–88, 1983.

[39] Imry, Y., *Introduction to mesoscopic physics*. Oxford: Oxford University Press, 1997.

[40] Ingerman, A., Johansson, G., Shumeiko, V. S., and Wendin, G., "Coherent multiple Andreev reflections and current resonances in SNS quantum point contacts," *Phys. Rev. B*, vol. 64, p. 144504, 2001.

[41] Jansen, A. G. M., van Gelder, A. P., and Wyder, P., "Point contact spectroscopy in metals," *J. Phys. C: Solid St. Phys.*, vol. 13, pp. 6073–6118, 1980.

[42] Johansson, G., Wendin, G., Bratus', E., and Shumeiko, V., "Multiple Andreev reflections as a transport problem in energy space," *Superlattices and Microstructures*, vol. 25, no. 5-6, pp. 905–914, 1999.

[43] Josephson, B. D., "Possible new effects in superconductive tunnelling," *Phys. Lett.*, vol. 1, pp. 251–253, 1962.

[44] Kohn, W. and Sham, L. J., "Self-consistent equations including exchange and correlation effects," *Phys. Rev.*, vol. 140, pp. A1113–A1138, 1965.

[45] Kolesnychenko, O. Y., Shklayarevskii, O. I., and van Kempen, H., "Calibration of the distance between electrodes of mechanically controlled break junctions using field-emission resonance," *Rev. Sci. Instrum.*, vol. 70, pp. 1442–1446, 1999.

[46] Kondo, J., "Resistance minimum in dilute magnetic alloys," *Prog. Theor. Phys.*, vol. 32, p. 37, 1964.

[47] Koops, M. C., van Duyneveldt, G. V., and de Bruyn Ouboter, R., "Direct observation of the current-phase relation of an adjustable superconducting point contact," *Phys. Rev. Lett.*, vol. 77, pp. 2542–2545, 1996.

[48] Krans, J. M., van Ruitenbeek, J. M., Fisun, V. V., Yanson, I. K., and de Jongh, L. J., "The signature of conductance quantization in metallic point contacts," *Nature*, vol. 375, pp. 767–769, 1995.

[49] Kulik, I. O., "Macroscopic quantization and the proximity effect in S-N-S junctions," *Sov. Phys. JETP*, vol. 30, pp. 944–950, 1970. [Zh. Eksp. Teor. Fiz. **57** (1969) 1745–1759].

[50] Kulik, I. O. and Omelyanchuk, A. N., "Contribution to the microscopic theory of the Josephson effect in superconducting bridges," *JETP Lett.*, vol. 21, pp. 96–97, 1975.

[51] Landauer, R., "Spatial variation of currents and fields due to localized scatterers in metallic conduction," *IBM J. Res. Dev.*, vol. 1, pp. 223–231, 1957.

[52] Landauer, R., "Electrical resistance of disordered one-dimensional lattices," *Phil. Mag.*, vol. 21, pp. 863–867, 1970.

[53] Landman, U., Luedtke, W. D., Burnham, N. A., and Colton, R. J., "Atomistic mechanisms and dynamics of adhesion, nanoindentation, and fracture," *Science*, vol. 248, pp. 454–461, 1990.

[54] Landman, U., Luedtke, W. D., and Gao, J., "Atomic-scale issues in tribology: interfacial junctions and nano-elastohydrodynamics," *Langmuir*, vol. 12, pp. 4514–4528, 1996.

[55] Landman, U., Luedtke, W. D., Salisbury, B. E., and Whetten, R. L., "Reversible manipulations of room temperature mechanical and quantum transport properties in nanowire junctions," *Phys. Rev. Lett.*, vol. 77, pp. 1362–1365, 1996.

[56] Lang, N. D., "Resistance of a one-atom contact in the scanning tunneling microscope," *Phys. Rev. B*, vol. 36, pp. 8173–8176, 1987.

[57] Lantz, J., Shumeiko, V. S., Bratus, E., and Wendin, G., "Phase-dependent multiple andreev reflections in sns interferometers," *Phys. Rev. B*, vol. 65, p. 134523, 2001.

[58] Ludoph, B., van der Post, N., Bratus', E. N., Bezuglyi, E. V., Shumeiko, V. S., Wendin, G., and van Ruitenbeek, J. M., "Multiple Andreev reflection in single atom niobium junctions," *Phys. Rev. B*, vol. 61, pp. 8561–8569, 2000.

[59] Lysykh, A. A., Yanson, I. K., Shklyarevski, O. I., and Naydyuk, Y. G., "Point-contact spectroscopy of electron-phonon interaction in alloys," *Solid State Commun.*, vol. 35, pp. 987–989, 1980.

[60] Martinis, J. M., Nam, S., Aumentado, J., and Urbina, C., "Rabi oscillations in a large josephson-junction qubit," *Phys. Rev. Lett.*, vol. 89, no. 11, p. 117901, 2002.

[61] Montie, E., Cosman, E., Thooft, G., van der Mark, M., and Beenakker, C., "Observation of the optical analog of quantized conductance of a point contact," *Nature*, vol. 350, pp. 594–595, 1991.

[62] Moreland, J. and Ekin, J. W., "Electron tunneling experiments using Nb-Sn 'break' junctions," *J. Appl. Phys.*, vol. 58, pp. 3888–3895, 1985.

[63] Muller, C. J., van Ruitenbeek, J. M., and de Jongh, L. J., "Conductance and supercurrent discontinuities in atomic-scale metallic constrictions of variable width," *Phys. Rev. Lett.*, vol. 69, pp. 140–143, 1992.

[64] Nygard, J., Cobden, D. H., and Lindelof, P. E., "Kondo physics in carbon nanotubes," *Nature*, vol. 408–410, p. 342, 2000.

[65] Octavio, M., Blonder, G. E., Tinkham, M., and Klapwijk, T. M., "Subharmonic energy-gap structure in superconducting constrictions," *Phys. Rev. B*, vol. 27, pp. 6739–6746, 1983.

[66] Ohnishi, H., Kondo, Y., and Takayanagi, K., "Quantized conductance through individual rows of suspended gold atoms," *Nature*, vol. 395, pp. 780–785, 1998.

[67] Olesen, L., Lægsgaard, E., Stensgaard, I., Besenbacher, F., Schiøtz, J., Stoltze, P., Jacobsen, K. W., and Nørskov, J. K., "Quantised conductance in an atom-sized point contact," *Phys. Rev. Lett.*, vol. 72, pp. 2251–2254, 1994.

[68] Park, J., Pasupathy, A. N., Goldsmith, J. I., Chang, C., Yaish, Y., Petta, J. R., Rinkoski, M., Sethna, J. P., Abruña, H. D., McEuen, P. L., and Ralph, D., "Coulomb blockade and the Kondo effect in single atom transistors," *Nature*, vol. 417, pp. 722–725, 2002.

[69] Pascual, J. I., Méndez, J., Gómez-Herrero, J., Baró, A. M., García, N., and Binh, V. T., "Quantum contact in gold nanostructures by scanning tunneling microscopy," *Phys. Rev. Lett.*, vol. 71, pp. 1852–1855, 1993.

[70] Pascual, J. I., Méndez, J., Gómez-Herrero, J., Baró, A. M., García, N., Landman, U., Luedtke, W. D., Bogachek, E. N., and Cheng, H.-P., "Properties of metallic nanowires: From conductance quantization to localization," *Science*, vol. 267, pp. 1793–1795, 1995.

[71] Penttilä, J. S., Parts, U., Hakkonen, P. J., Paalanen, M. A., and Sonin, E. B., ""Superconductor-insulator transition in a single Josephson junction," *Phys. Rev. Lett.*, vol. 82, no. 5, pp. 1004–1007, 1999.

[72] Perdew, J. P., Burke, K., and Ernzerhof, M., "Generalized gradient approximation made simple," *Phys. Rev. Lett.*, vol. 77, no. 18, pp. 3865–3868, 1996.

[73] Prokhorov, V. G., "Dependence of the superconducting transition temperature on the thickness of superconducting films with different coherence lengths," *Low Temp. Phys.*, vol. 24, no. 6, pp. 410–413, 1998.

[74] Pustilnik, M., "Kondo effect in nanostructures," *Physica Status Solidi (a)*, vol. 203, pp. 1137–1147, 2006.

[75] Rodrigues, V. and Ugarte, D., "Real-time imaging of atomistic process in one-atom-thick metal junctions," *Phys. Rev. B*, vol. 63, p. 073405, 2001.

[76] Rubio, G., Agraït, N., and Vieira, S., "Atomic-sized metallic contacts: Mechanical properties and electronic transport," *Phys. Rev. Lett.*, vol. 76, pp. 2302–2305, 1996.

[77] Schedelbeck, G., Wegscheider, W., Bichler, M., and Abstreiter, G., "Coupled quantum dots fabricated by cleaved edge overgrowth: From artificial atoms to molecules," *Science*, vol. 278, no. 5344, pp. 1792–1795, 1997.

[78] Scheer, E., Agraït, N., Cuevas, J. C., Levy Yeyati, A., Ludoph, B., Martín-Rodero, A., Rubio Bollinger, G., van Ruitenbeek, J. M., and Urbina, C., "The signature of chemical valence in the electrical conduction through a single-atom contact," *Nature*, vol. 394, pp. 154–157, 1998.

[79] Scheer, E., Cuevas, J. C., Levy Yeyati, A., Martín-Rodero, A., Joyez, P., Devoret, M. H., Esteve, D., and Urbina, C., "Conduction channels of superconducting quantum point contacts," *Physica B*, vol. 280, pp. 425–431, 2000.

[80] Scheer, E., Joyez, P., Esteve, D., Urbina, C., and Devoret, M. H., "Conduction channel transmissions of atomic-size aluminum contacts," *Phys. Rev. Lett.*, vol. 78, pp. 3535–3538, 1997.

[81] Schwab, K., Henriksen, E. A., Worlock, J. M., and Roukes, M. L., "Measurement of the quantum of thermal conductance," *Nature*, vol. 404, no. 6781, pp. 974–977, 2000.

[82] Shumeiko, V. S., Bratus', E. N., and Wendin, G., "dc-current transport and ac Josephson effect in quantum junctions at low voltage," *Low Temp. Phys.*, vol. 23, pp. 181–192, 1997.

[83] Smith, D. P. E., "Quantum point contact switches," *Science*, vol. 269, pp. 371–373, 1995.

[84] Stalder, A. and Dürig, U., "Study of plastic flow in ultrasmall Au contacts," *J. Vac. Sci. Technology B*, vol. 14, pp. 1259–1263, 1996.

[85] Takahide, Y., Yagi, R., Kanda, A., Ootuka, Y., and S.Kobayashi, "Superconductor-insulator transition in a two-dimensional array of resistively shunted small josephson junctions," *Phys. Rev. Lett.*, vol. 85, no. 9, pp. 1974–1977, 2000.

[86] Tarucha, S., Austing, D. G., Honda, T., van der Hage, R. J., and Kouwenhoven, L. P., "Shell filling and spin effects in a few electron quantum dot," *Phys. Rev. Lett.*, vol. 77, no. 17, pp. 3613–3616, 1996.

[87] Taylor, J., Guo, H., and Wang, J., "Ab initio modeling of quantum transport properties of molecular electronic devices," *Phys. Rev. B*, vol. 63, no. 24, p. 245407, 2001.

[88] Terabe, K., Hasegawa, T., Nakayama, T., and Aono, M., "Quantized conductance atomic switch," *Nature*, vol. 433, pp. 47–50, 2004.

[89] Thornton, T. J., Pepper, M., Ahmed, H., Andrews, D., and Davies, G. J., "One-dimensional conduction in the 2D electron gas of a GaAs-AlGaAs heterojunction," *Phys. Rev. Lett.*, vol. 56, no. 11, pp. 1198–1201, 1986.

[90] Tinkham, M., *Introduction to superconductivity*. New-York: McGraw-Hill, 1996.

[91] Topinka, M. A., LeRoy, B. J., Shaw, S. E. J., Heller, E. J., Westervelt, R. M., Maranowski, K. D., and Gossard, A. C., "Imaging coherent electron flow from a quantum point contact," *Science*, vol. 289, no. 5488, pp. 2323–2326, 2000.

[92] Troullier, N. and Martins, J. L., "Efficient pseudopotentials for plane-wave calculations," *Phys. Rev. B*, vol. 43, pp. 1993–2006, Jan 1991.

[93] van den Brom, H., Yanson, A. I., and van Ruitenbeek, J. M., "Characterization of individual conductance steps in metallic quantum point contacts," *Physica B*, vol. 252, pp. 69–75, 1998.

[94] van der Post, N., Peters, E. T., Yanson, I. K., and van Ruitenbeek, J. M., "Subgap structure as function of the barrier in atom-size superconducting tunnel junctions," *Phys. Rev. Lett.*, vol. 73, pp. 2611–2613, 1994.

[95] van Ruitenbeek, J. M., Alvarez, A., Piñeyro, I., Grahmann, C., Joyez, P., Devoret, M. H., Esteve, D., and Urbina, C., "Adjustable nanofabricated atomic size contacts," *Rev. Sci. Instrum.*, vol. 67, pp. 108–111, 1996.

[96] van Wees, B. J., van Houten H., H., Beenakker, C. W. J., Williamson, J. G., Kouwenhoven, L. P., van der Marel, D., and Foxon, C. T., "Quantised conductance of point contacts in a two-dimensional electron gas," *Phys. Rev. Lett.*, vol. 60, pp. 848–850, 1988.

[97] Weissman, M. B., "$1/f$ noise and other slow, nonexponential kinetics in condensed matter," *Rev. Mod. Phys.*, vol. 60, no. 2, pp. 537–571, 1988.

[98] Wharam, D. A., Thornton, T. J., Newbury, R., Pepper, M., Ahmed, H., Frost, J. E. F., Hasko, D. G., Peacock, D. C., Ritchie, D. A., and Jones, G. A. C., "One-dimensional transport and the quantisation of the ballistic resistance," *J. Phys. C*, vol. 21, pp. L209–L214, 1988.

[99] Yannouleas, C., Bogachek, E. N., and Landman, U., "Energetics, forces, and quantized conductance in jellium-modeled metallic nanowires," *Phys. Rev. B*, vol. 57, pp. 4872–4882, 1998.

[100] Yanson, A. I., *Atomic chains and electronic shells: Quantum mechanisms for the formation of nanowires*. PhD thesis, Universiteit Leiden, The Netherlands, 2001.

[101] Yanson, A. I., Rubio Bollinger, G., van den Brom, H. E., Agraït, N., and van Ruitenbeek, J. M., "Formation and manipulation of a metallic wire of single gold atoms," *Nature*, vol. 395, pp. 783–785, 1998.

[102] Zaitsev, A. V. and Averin, D. V., "Theory of ac Josephson effect in superconducting constrictions," *Phys. Rev. Lett.*, vol. 80, no. 16, pp. 3602–3605, 1998.

[103] Zazunov, A., Shumeiko, V. S., Bratus', E. N., Lantz, J., and Wendin, G., "Andreev level qubit," *Phys. Rev. Lett.*, vol. 90, no. 8, p. 087003, 2003.

[104] Zazunov, A., Shumeiko, V. S., Wendin, G., and Bratus', E. N., "Dynamics and phonon-induced decoherence of andreev level qubit," *Phys. Rev. B*, vol. 71, no. 21, 2005.

[105] Zhang, C. and Landman, U. *to be published.*

[106] Zheng, H. Z., Wei, H. P., Tsui, D. C., and Weimann, G., "Gate-controlled transport in narrow GaAs/Al_xGa_{1-x}As heterostructures," *Phys. Rev. B*, vol. 34, no. 8, pp. 5635–5638, 1986.

VITA

Zhenting Dai was born in Sanming, Fujian Province of China. He received his Bachelor degree of Science in Physics from Jilin University, Changchun, China, in 1996. He came to School of Physics, Georgia Institute of Technology as a graduate student in 1999. He received Master of Science in Physics from the School of Physics at Georgia Tech in 2001 and Master of Science from School of Electrical and Computer Engineering in 2005. He has been conducting graduate research under supervision of Professor Alexei Marchenkov since January, 2002.